

Grazing Incidence Pumped Zr X-Ray Laser
for Spectroscopy on Li-like Ions

Dissertation zur Erlangung des Grades
“Doktor der Naturwissenschaften”

am Fachbereich Physik, Mathematik und Informatik
der Johannes Gutenberg-Universität
in Mainz

Daniel Ursescu
geboren in Piatra Neamț, Rumänien

Mainz, den 2006

Tag der Prüfung: 23.02.2006

Zusammenfassung

Röntgenlaser Fluoreszenz - Spektroskopie des $2s - 2p$ Übergangs in Lithium-ähnlichen Ionen hat das Potenzial, eine fast universell einsetzbare Methode zur Bestimmung von Kernradien stabiler und radioaktiver Isotope zu werden. Um solche Experimente am Experimentierspeicherring ESR, und auch dem späteren NESR innerhalb des FAIR Projekts, zu ermöglichen, wurde am PHELIX Laser der GSI Darmstadt ein Röntgenlaser aufgebaut, der die neuartige GRIP (Grazing Incidence Pumping) Geometrie verwendet. Mit dieser Geometrie ist stabiler Laserbetrieb bei verhältnismässig niedriger Pumpleistung möglich. Dies ist eine wichtige Voraussetzung für das Erreichen einer höheren Repetitionsrate. Im ersten Kapitel wird begründet, warum für die angesprochenen Experimente der Plasma Röntgenlaser die besten Voraussetzungen liefert. Ausserdem wird ein kurzer Überblick über die Entwicklung der Röntgenlaser gegeben. Die Besonderheit an der GRIP Geometrie ist die gezielte Deposition der Energie des Pumplasers in die für den Laserbetrieb optimale Dichteregion des Plasmas. In der Literatur beschränkt sich die Analyse dieses Prozesses in erster Linie auf die Bestimmung der Dichte am Umkehrpunkt der Trajektorie des Pumplaserstrahls. In dieser Arbeit wird demonstriert, dass sich die gesamte Energiedeposition unter GRIP erheblich modifiziert, wobei eine Vielzahl von Parametern unterschiedlich beitragen. Im zweiten Kapitel wird zunächst die übliche theoretische Behandlung der Plasmadynamik, des aktiven Lasermediums und der Röntgenlaser Emission erläutert. Zusätzlich wird eine darüber hinausgehende, neuartige Analyse der Laserabsorption unter Berücksichtigung eines Korrekturfaktors für die Absorption durch Inverse Bremsstrahlung (IB) vorgestellt. Im dritten Kapitel wird der experimentelle Aufbau des Lasers und der Diagnostik vorgestellt. In diesem Zusammenhang wird eine analytische Formel für die derzeit an GRIP Lasern ausschliesslich verwendete Fokussierungsoptik entwickelt, die es erlaubt, die mittlere und positionsabhängige Traveling Wave Geschwindigkeit direkt zu berechnen. Das vierte Kapitel ist den experimentellen Ergebnissen gewidmet. Speziell wird auf die Abhängigkeit der Pumplaserabsorption und der Laserintensität in verschiedenen Röntgenlinien vom Einfallswinkel des Haupt-Pumpimpulses eingegangen. Die Resultate für die zwei untersuchten Einfallswinkel werden mit den theoretischen Modellen verglichen. Es zeigt sich, dass durch den veränderten Einfallswinkel im Vergleich zu einem einfachen analytischen Modell, das die Geometrie nicht in Betracht zieht, sehr starke Änderungen des Zeitverhaltens der Plasmatemperatur auftreten. Das in dieser Arbeit entwickelte Modell zeigt eine weit bessere Übereinstimmung. Ein interessantes Resultat ist auch das Auftreten einer zentralen Abschwächung der örtlich aufgelösten keV Emission, das bei den Experimenten erstmals direkt beobachtet werden konnte und gut mit früheren Beobachtungen im Ausgangsprofil des Röntgenlasers und der Plasmaverteilung korreliert. Die Schlussbemerkung enthält neben einer Zusammenfassung den Ausblick auf die Möglichkeiten zur Erzielung höherer Photonenenergie.

Abstract

X-ray laser fluorescence spectroscopy of the 2s-2p transition in Li-like ions is promising to become a widely applicable tool to provide information on the nuclear charge radii of stable and radioactive isotopes. For performing such experiments at the Experimental Storage Ring ESR, and the future NESR within the FAIR Project, a grazing incidence pumped (GRIP) x-ray laser (XRL) was set up at GSI Darmstadt using PHELIX (Petawatt High Energy Laser for heavy Ions eXperiments). The experiments demonstrated that lasing using the GRIP geometry could be achieved with relatively low pump energy, a prerequisite for higher repetition rate. In the first chapter the need of a plasma XRL is motivated and a short history of the plasma XRL is presented. The distinctive characteristic of the GRIP method is the controlled deposition of the pump laser energy into the desired plasma density region. While up to now the analysis performed were mostly concerned with the plasma density at the turning point of the main pump pulse, in this thesis it is demonstrated that also the energy deposition is significantly modified for the GRIP method, being sensitive in different ways to a large number of parameters. In the second chapter, the theoretical description of the plasma evolution, active medium and XRL emission properties are reviewed. In addition an innovative analysis of the laser absorption in plasma which includes an inverse Bremsstrahlung (IB) correction factor is presented. The third chapter gives an overview of the experimental set-up and diagnostics, providing an analytical formula for the average and instantaneous traveling wave speed generated with a tilted, on-axis spherical mirror, the only focusing system used up to now in GRIP XRL. The fourth chapter describes the experimental optimization and results. The emphasis is on the effect of the incidence angle of the main pump pulse on the absorption in plasma and on output and gain in different lasing lines. This is compared to the theoretical results for two different incidence angles. Significant corrections for the temperature evolution during the main pump pulse due to the incidence angle are demonstrated in comparison to a simple analytical model which does not take into account the pumping geometry. A much better agreement is reached by the model developed in this thesis. An interesting result is also the appearance of a central dip in the spatially resolved keV emission which was observed in the XRL experiments for the first time and correlates well with previous near field imaging and plasma density profile measurements. In the conclusion also an outlook to the generation of shorter wavelength XRL's is given.

Contents

1	Introduction	1
1.1	Determination of nuclear structure	1
1.2	Li-like ions spectroscopy at GSI	2
1.3	Development of x-ray lasers	6
1.3.1	Short history of CE XRL	8
1.4	Synchronization of the accelerators with PHELIX	13
2	Principles of TCE XRL	15
2.1	Plasma creation for XRL	15
2.2	Absorption of high laser fields	22
2.3	Laser propagation in plasmas	24
2.3.1	The complex refraction index of the plasma	24
2.3.2	Ray tracing of the main pulse including absorption	29
2.3.3	High intensity laser absorption in plasma	30
2.4	Active medium	38
2.4.1	Ionization dynamics in nanosecond laser pulses	38
2.4.2	Ni-like ions rate equations	39
2.5	Properties of the x-ray laser emission	41
3	X-Ray Laser set-up with PHELIX	45
3.1	PHELIX laser	45
3.1.1	The front-ends	46
3.1.2	PHELIX 10 Joule preamplifier	49
3.1.3	Main amplifier, petawatt compresor and booster	50
3.1.4	10 Joule Compressor	51
3.2	Experimental set-up	51
3.2.1	Focusing system characterization	52
3.2.2	XRL diagnostics	60

4	Experiments results	63
4.1	Lasing lines	66
4.2	Delay between the pumping pulses	67
4.3	Optimal duration of the main pump pulse	71
4.4	Main pulse absorption: theory vs. experiment	73
4.5	Small gain coefficient of the XRL	77
4.6	Prepulse influence and gain region	81
4.7	Target behavior	83
4.8	X-ray emission dip	83
5	Conclusions	91
A	Synchronization with SIS	95

List of Figures

1.1	Level scheme of lithium-like ions	4
1.2	X-ray laser types	7
1.3	Comparison of different XRL types: pump energy needed to achieve a given wavelength	11
2.1	Preplasma creation and traveling wave excitation	16
2.2	Schematic representation of the TCE XRL	17
2.3	The inverse Bremsstrahlung correction factor for different pre- plasma temperatures and various laser intensities	23
2.4	Double logarithmic plot of the IB correction factor at low pre- plasma temperatures	24
2.5	Laser frequency, plasma frequency and electron collision fre- quency dependence on density	25
2.6	The real part of the refraction index	26
2.7	The dependence of the refraction index on the plasma density and temperature for $Zf=8$	28
2.8	The complex part of the refraction index depending on tem- perature and plasma density, for $Zf=8$	28
2.9	Absorption scale length as function of normalized plasma fre- quency for different normalized collision rates	31
2.10	Detail of the absorption scale length as function of normalized plasma frequency for different normalized collision rates	31
2.11	Parametric ray-tracing of the beam including intensity trans- mission at incidence angles from 10° to 80°	33
2.12	Ray tracing for various incidence angles on target	34
2.13	Ray-tracing for different incident angles on target 1:1	34
2.14	Transmission in the plasma as function of the plasma density for several plasma scale lengths	35
2.15	Ray tracing in the plasma for different plasma scale lengths	36
2.16	Transmitted intensity as function of the depth in the plasma for several Zf values	36

2.17	Transmitted intensity as function of the depth in the plasma for different plasma temperatures	37
2.18	Energy level representation for Ni-like ions indicating the collisional transition and the lasing line	40
3.1	Schematic representation of the PHELIX laser system: the bold fonts show the subsystems in use for GRIP XRL	46
3.2	PHELIX building ground floor layout with the position of the main subsystems indicated	47
3.3	Experimental set-up picture with the focusing systems for prepulse and main pulse and part of the diagnostics	53
3.4	Representation of the main pulse focusing system	54
3.5	Contour plot of the line focus length	56
3.6	Line focus intensity distribution	57
3.7	Average traveling wave velocity along the line focus	58
3.8	Local traveling wave excitation velocity in speed of light units as a function of the local incidence angle on a spherical mirror	59
3.9	Detail photo with the spectrograph	60
3.10	Transmission curves for the various filters used during experiments	62
4.1	Spectrum of shot 47 (45°) for 3.6 mm target length, represented in 3D	64
4.2	Measurement of the spatial resolved keV emission of the plasma for typical shot (45°)	64
4.3	Spectrum of shot 15 (72°) represented in 3D	65
4.4	Measurement of the keV emission of the plasma for the GRIP set-up	65
4.5	Logarithmic representation of measured lasing lines corrected for transmission filter of the spectrograph.	66
4.6	Output of the GRIP Zr XRL as a function of the peak-to-peak delay of the prepulse and main pulse	67
4.7	Measured thermal oscillations of the preamplifier laser heads as a function of time, due to the cooling system feedback loop	68
4.8	Ionization potentials for Zr	69
4.9	The keV emission of the plasma measured with the pinhole camera for various peak-to-peak delays, at 72° angle (GRIP)	70
4.10	Comparison of the plasma x-ray emission intensity as function of main pulse duration for 45° and 72° incidence angles on target	72
4.11	Calculated transmission of a 0.5 ps and a few ps main pulse through plasma	74

4.12	Temperature evolution of the plasma in time during the main pulse	75
4.13	Comparison of the cross-slit camera measurement with theory for the 45° incidence angle	76
4.14	Comparison of the x-ray laser emission as a function of main pulse duration for 45° and 72° incidence angles on target	76
4.15	Zr XRL gain measurement using linear scale (72°)	78
4.16	Zr XRL gain measurement using logarithmic scale (72°)	79
4.17	Gain curves for the experiment with 45°	79
4.18	Gain measurements for the second lasing line and a Linford fit (72°)	80
4.19	Gain measurements for the lasing line at 26.4 nm (45°) using two methods	81
4.20	Spatial profile along the 22.02 nm lasing line registered by the spectrograph at 45° pumping geometry	82
4.21	Groove in the target after several shots	84
4.22	Scanning electron microscope image of the Zr target after two shots in GRIP configuration with 0.5 ps main pulse duration	85
4.23	3D representation of the spatially resolved keV plasma emission with the dip feature	86
4.24	Near field images obtained with TCE Ag Ni-like XRL	88
A.1	PHELIX-SIS synchronization	97

Chapter 1

Introduction

1.1 Determination of nuclear structure

Besides nuclear masses (or binding energies), nuclear charge radii, spin and nuclear moments are key informations on ground state properties of atomic nuclei.

These informations would help us better understand the forces governing the nucleus. The nucleus is in fact dominated by many-body phenomena. Due to this fact the fundamental interactions responsible for the forces in nuclear physics become less and less evident in these increasingly complex systems.

Constant research effort went in both theory and experiments for unraveling the essence and the value of this fundamental force in nature.

Theory provides us with a wide spectrum of nuclear structure models and methods starting with shell model, collective models, models based on group theory, cluster models and variations like for example the dynamic correlation model [[TLF⁺04](#)], Hartree-Fock and random-phase approximations and Monte Carlo models (see the review from [[CMPN⁺05](#)] and references quoted there). For a theoretical introduction on the determination of the magnetic moment and the quadrupole moment of the nuclei see [[Ney03](#)].

Atomic spectroscopy has provided extended information about the ground state nuclear structure and properties for radioactive nuclei [[Ott89](#), [Klu02](#)]. The opportunity to use these methods comes from the fact that the magnetic moment, the quadrupole moment and the charge distribution of the nuclei are producing small but measurable effects in the electronic structure of the ions or atoms. These effects are well understood so it is possible, using simple electronic systems, to access the information concerning the ground state properties of the nuclei.

Extended theoretical models were developed to produce more accurate numerical results for both the nuclear part and the atomic part. An important step forward would be the free availability of such codes which would boost the scientific output considerably. The rapid advance of computer technology allows now to perform complicated calculations on a home computer. Moreover, combination of numerical codes with symbolic ones is now easily possible. Tools like RACAH [GSF05], DIRAC [SKF05] and FERMI [UTKF05] packages are developed in this direction, for combining algebraic properties of the many body systems with numerical ones. In this way, many body theories like for example dynamic correlation model [TLK⁺03, TLF⁺04, TLFK04] would become more transparent and easy to use.

Over the last four decades there were practically three main experimental research lanes which facilitated the outstanding progress in the determination of the ground state properties of the nuclei from ion systems measurements. *Large scale ion accelerator facilities* were built being able to provide more than thousand of nuclei isotopes. Their production capabilities were further combined with storage techniques like *storage rings and traps* in order to fulfill the dream of providing every ionization state for every achievable isotope¹ [KB04, KBHQ03]. Third, the use of *lasers* outstanding properties like directionality and spectral purity made possible accurate measurements of the electronic properties of the atoms and ions, thus gathering valuable informations related to the nucleus using nuclear effects on the electronic structure. The use of laser techniques in nuclear physics has been reviewed recently in [Neu02] and [KN03].

1.2 Li-like ions spectroscopy at GSI

Such measurements are especially favourable at GSI (Gesellschaft fuer Schwerionenforschung mbH, in Darmstadt) where all elements up to uranium can be obtained in a specific charge state (bare, hydrogen-like, helium-like, lithium-like and so on), a large number of radioactive isotopes are available at the fragment separator (FRS) by fragmentation or fission, and where these ion beams can be stored, electron cooled, and bunched in the experimental storage ring (ESR).

Although the information on nuclear ground-state properties extracted from a study of hyperfine structure and isotope shift is model-independent, it is hampered in complex neutral atoms by the accuracy with which the

¹A similar dream is now transformed in reality: large scale facilities to provide coherent electromagnetic fields at any wavelength are now envisioned by projects like DESY-TESLA and SLAC-LCLS.

electron wave functions are known at the site of the nucleus. In that respect it is highly advantageous to measure these effects in highly charged ions with one or only few electrons. Since the electron wave function can precisely be calculated in such simple few-electron systems, uncertainties are negligible due to the atomic hyperfine fields at the site of the nucleus. In this way, absolute charge radii can be determined instead of only changes in charge radii between two isotopes of the same element as accessible by conventional isotope shift measurements. Furthermore, in combination with measurements of the matter radius, neutron radii can be determined. This adds a new quality to studies of hyperfine structures and isotope shifts, since the evolution of nuclear properties cannot only be followed along isotopic chains (where - also in the case of neutral atoms - the electronic factor stays almost constant) but also along isotonic chains.

Lithium-like ions are most suited for the experiments proposed here since they represent a good compromise between the request for reliable calculations of the electronic factor and low atomic excitation energy. The most hunted ion is Li-like Uranium which is providing the strongest Coulomb field to its electrons, producing the strongest measurable QED effects among all ionic systems. In the pursuit for evaluation of these effects, both theory groups and experimentalists were producing remarkable results.

Figure 1.1 shows the level scheme of Li-like uranium with the 2s - 2p transitions.

The $2S_{1/2}$ - $2P_{1/2}$ transition in uranium has been measured in several complex experiments at Lawrence Berkeley National Laboratory in USA [SBB⁺91] and at GSI in Darmstadt [BKM⁺03]. However, very recently the last result was improved by a factor of 7 in [BCTT05] where an energy of 280.645 ± 0.015 eV was measured for the transition. In a two months experiment employing the SuperEBIT (electron beam ion trap) in Livermore, the fluctuations of the spectral line peak were determined to be a factor of two lower than the spectral resolution of the spectrometer ($\frac{\Delta\lambda}{\lambda}$) involved in the measurements. In this way the experimental accuracy of the measurement reached $3.6 \cdot 10^{-4}$.

An alternative proposal for the systematic measurement of this transition for most of the Li-like ions is described in [BBdMK⁺00, NAdM⁺01]. At ESR energies, photon energies of around 110 eV in the laboratory frame would be sufficient to induce this transition in Li-like uranium when the laser generating the photons is directed anti-collineary to the ions. Since the emitted photon after laser excitation again will be strongly Doppler shifted, high detection sensitivity and good suppression of scattered laser light can be reached. Photon energies around 56 eV, as achieved recently at GSI using PHELIX (Petawatt High Energy Laser for heavy Ions eXperiments)

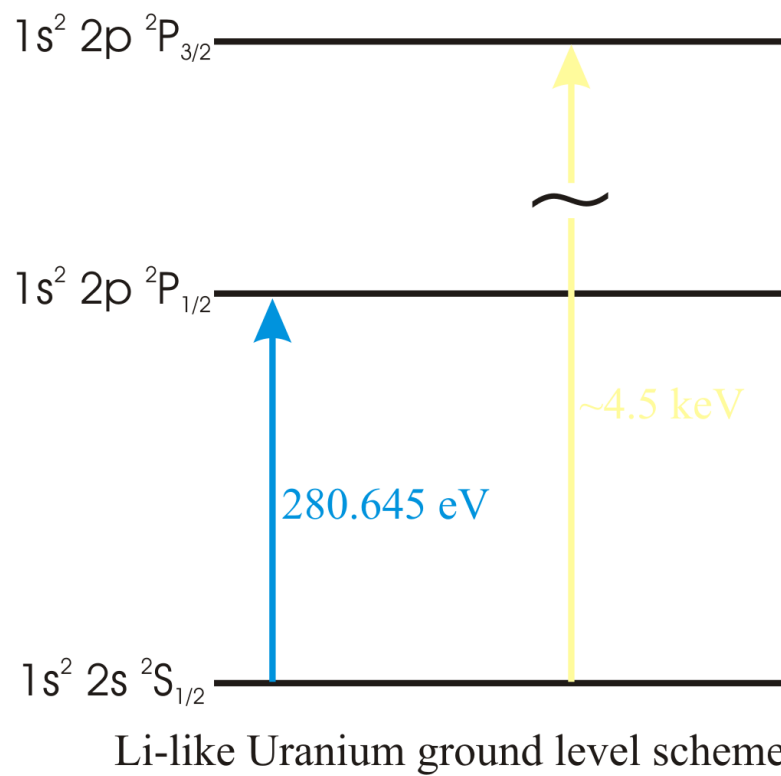


Figure 1.1: Level scheme of lithium-like ions. The transition energies are indicated for Li-like uranium.

preamplifier [NSC⁺04] and as reported in this work would reach well above lithium-like tin.

The requirements on the pulsed laser system for getting a reasonable signal for hyperfine structure and isotope shift studies are moderate with respect to repetition rate and laser power. The range of ion velocities in the ESR between 20% and 80% of the speed of light allows one to choose the optimum scheme of an x-ray laser with the photon energy appropriate for the ion under investigation. Since tuning can be achieved via the Doppler shift in the ESR by variation of the beam velocity, a fixed frequency laser can be used.

The relative line width of the transition is on the order of 10^{-7} . Therefore a narrow band laser is needed for as good as possible spectral overlap. X-ray lasers constitute the most narrow-band source currently available in the soft x-ray regime. The bandwidth of x-ray lasers has been determined to be on the order of 10^{-5} . Given this, the excitation cross section can be calculated to be 10^{-16} cm^2 . In the ESR, a beam of 10^5 radioactive ions in the storage ring typically can be cooled to an emittance of $0.1 \pi \text{ mm mrad}$ and bunched to a length of only 2 m. At these parameters, a good overlap of laser and ion beam can be achieved. Assuming the presently reported x-ray intensity to be 10^{11} photons per pulse, an excitation probability of around 0.1 percent can be achieved.

Light emitted after laser excitation is detected in the forward direction. This leads to an additional Doppler shift into an energy range between two and three times the laser energy. These energetic photons can be efficiently and selectively detected by multi-channel plates or by scintillator coated waveguides inserted into the vacuum close to the ion beam. Absorber foils can reject visible photons and critical x-ray background.

Even with as few as 10^5 ions in a bunch, multiple hits on the detector will be registered in resonance for every pulse. The fast response restricts background to the time interval given by the length of the laser pulse and the flight pass of the resonant photons. Outside of optical resonance this should give negligible count rates. Therefore about 10 pulses per frequency interval should be sufficient to record a signal.

As an example for the required accuracy, the isotope shift between ^{238}U and ^{235}U in the $2s_{1/2} - 2p_{1/2}$ transition is approximately 0.3 eV. For the case of Li-like ^{235}U the hyperfine splitting of the $2s_{1/2}$ state is about 1 eV and the $2p_{1/2}$ splitting is around 0.3 eV. After electron cooling, the line width of the signal of 10 meV will therefore enable a measurement of the hyperfine and relative isotope shift effects with an accuracy of 10^{-5} limited by the uncertainties of the Doppler width. The precision of the determination of the large total contribution from the extended nuclear charge, and thereby

the charge radius, can be expected to be in the order of 10^{-4} . For this accuracy the ion beam velocity in the ESR has to be known within the 10^{-5} range which is feasible.

1.3 Development of x-ray lasers

For the envisaged experiments described in the previous section, one needs a quasi-monochromatic x-ray source which should have a relative bandwidth in the range of 10^{-5} .

In the recent years, ultraviolet and x-ray sources were developed with remarkable results. Bright coherent short wavelength sources are available now. Rapid progress was enabled by developments in high power lasers as well as progress in electron beam physics and technology. Laser harmonics generation [SBS⁺97, HKM⁺02, TNM04, GPW⁺04], free electron lasers [ABB⁺02] and capillary X-ray lasers [GFR⁺02, SMR⁺02] are the best existing choices for coherent radiation in the UV region, providing in addition short pulses in the femtosecond and sub-femtosecond range with high repetition rate. On the other hand synchrotron radiation is covering a wide wavelength range in the hard X-ray domain. All these short wavelength sources, while giving outstanding resolution in the time domain, do not offer spectral resolution with high peak brilliance in the intermediate regime at wavelengths between 3 nm to 25 nm. The X-Ray Lasers (XRL) are filling this gap with relative spectral bandwidth better than 10^{-4} and peak brilliance of $10^{22} - 10^{26}$ photons/(s mm² mrad²) in 0.01% bandwidth, so several orders of magnitude more than any other existing sources [Dai02] in pulses as short as 2 ps [KJR⁺02].

The three categories of fundamental processes used to obtain coherent XUV - x-ray sources namely: high-order harmonics generation (HHG), self-amplified spontaneous emission of electron beams in electromagnetic fields (SASE) and plasma emission (plasma XRL) are schematically represented in fig. 1.2.

High-order harmonics are induced in gas targets by short (femtosecond) laser pulses. The electrons of atomic or ionic systems are shaking strongly in the laser field emitting radiation at wavelengths which are odd integer multiple of the laser frequency. The wavelength of the harmonics emitted is sensitive to the pumping pulse duration decreasing with the pulse duration of the pump laser and increasing with the pump intensity. In this way up to 500 eV in He [SBS⁺97] and 250 eV in Ar-filled capillaries have been obtained [GPW⁺04]. They have very good beam quality but are broadband due to their short pulse duration (similar to the pump beam), making them impractical for high resolution laser fluorescence spectroscopy.

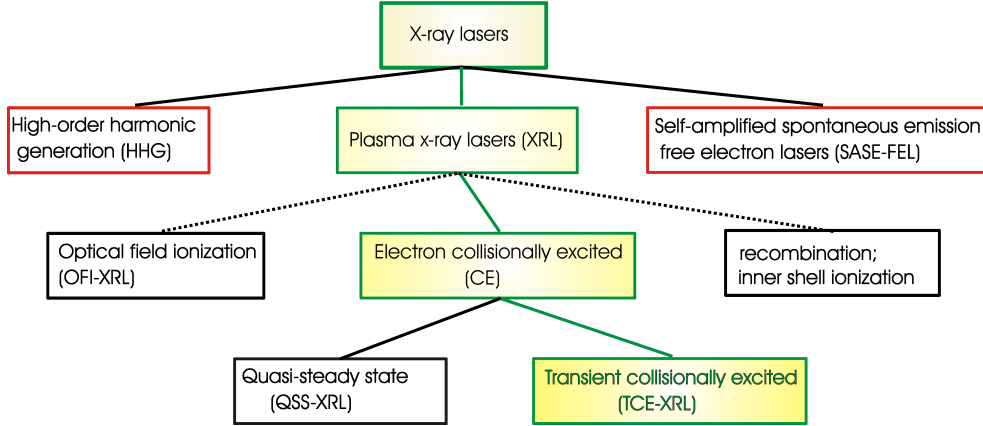


Figure 1.2: X-ray laser types

In the free electron lasers (FEL), an intense, energetic electron beam is made to pass through a periodic magnetic field, which causes the electrons to oscillate, and as they do so they emit light. The electron beam and the generated light interact cooperatively. This has the advantage, compared with the synchrotron-radiation light sources that have been used for decades, that in the FEL the light is produced in a coherent, tightly collimated beam that can be focused to high intensity [Pel01]. Two large-scale FEL projects are currently in the construction phase - the Linac Coherent Light Source project at Stanford and the TESLA project in Hamburg. TESLA, with a proposed multi-billion-dollar particle accelerator and FEL facility, has progressed furthest. The TESLA test facility is a smaller, proof-of-principle project that has begun operation at far-ultraviolet wavelengths and demonstrated in the year 2005 x-ray pulses at 30 nm wavelength. The pulses duration is short, below 100 fs and as a consequence the relative bandwidth of such lasers is still large (0.1).

In the plasma XRL lasing is obtained from specific transition in ionic systems of a given type: Ni-like, Ne-like, Pd-like and so on. We distinguish, for the clarity of the analysis, three steps: plasma generation, population inversion creation and the propagation of the coherent electromagnetic field in the plasma; all these steps are strongly influencing the XRL emission properties. One of the key factors is the plasma electron density where the population inversion is created because it will determine the main absorption mechanism for the laser pulse which creates the population inversion: at low electron plasma densities ($10^{17-18}/cm^3$) the ionization is initiated by optical field ionization (OFI) using high pump laser intensities ($10^{15-16}W/cm^2$), while at high densities ($10^{20-21}/cm^3$) the plasma production and the population

inversion are created with lower laser intensities in the electron collisional excitation schemes (CE). Other pumping schemes are also under consideration: recombination to H-like or Li-like ions for example can produce population inversion in a highly ionized plasma.

In OFI one uses gas targets, for most of the cases in capillary tubes where plasma is created by combinations of fast electric discharges and laser pulses. The wavelengths demonstrated to present are around 40 nm, too long for Li-like ions spectroscopy.

In the CE schemes the absorption of the laser pulse which induces the population inversion is due mainly to the inverse Bremsstrahlung (IB) mechanism close to the electron plasma critical density. Plasma creation in such systems is typically provided by irradiation of thick solid targets of various materials or thin solid coatings, with thicknesses in the order of few microns. The system we use employs thick solid targets so this type of systems will be further described in this thesis.

Other schemes for plasma lasers have been studied, too. In the recombination scheme, population inversion in H-like and Li-like ions is generated through electron capture in highly excited states and subsequent decay to the upper lasing level. Wavelength as short as 3.88 nm have been envisaged in H-like Al [BJM97] but without an experimental demonstration up to now. In the inner shell ionization schemes, the population inversion is generated by convincing the electrons placed in an inner shell to get excited by using x-ray radiation or by electron collisions [BDS+03, BSZ+05, BBS+05]. Little experimental evidence has been produced and a lot of development work is needed for these schemes. For more details see the review article from reference[Dai02].

Another important distinction we have to make for the plasma XRL using CE is the dynamics of the gain zone. If the x-ray laser emission duration is of the same order of magnitude with the population inversion equilibration time one speaks about transient collisionally excited (TCE) plasma XRL. If the emission is longer than the equilibrium time, one has a quasi steady state (QSS) of the population inversion in the XRL.

1.3.1 Short history of CE XRL

The pursuit for the x-ray laser started more than 35 years ago with the recombination schemes. In 1970s, English scientists [IP74, DJPR76] performed spectroscopic experiments to find out the population inversion in hydrogen-like carbon ions. Gain was found for the Balmer alpha transition at 18.2 nm pumped via recombination with bare ions in highly excited states and subsequent decay.

Population inversion has been found also in a recombining aluminium plasma which was later identified as 3d-4f and 3d-5f transitions in lithium-like ions [JJC⁺87].

The first clear demonstration of recombination type soft x-ray lasing pumped by a CO₂ laser was published in 1985 [SSM⁺85]. The gain-length product of 6.5 for the carbon 18.2 nm line was obtained.

Finally high intensity carbon x-ray laser pumped by a 2 ps, 20 J, laser using a 7 μm diameter carbon fiber as an x-ray laser target was demonstrated [ZKN⁺95]. The intensity on the target was $6 \cdot 10^{15}$ W/cm². The gain coefficient was 12.5 cm^{-1} and the gain-length product was 6 which was the largest value in the recombination schemes.

Although the recombination schemes inherently have significant advantages such as high pumping efficiency, no satisfactory lasing has been demonstrated. From the point of view of the soft x-ray sources for applications, the recombination schemes should be developed to achieve at least the saturated amplification. Further investigation should be needed.

Looking for alternative paths to recombination XRL, [ZKL76] first described a mechanism for obtaining an inversion between $2p^5 3p$ and $2p^5 3s$ levels in neon-like ions. Subsequently a series of papers were published about theoretical description [VAVE77]. To produce the inversion, the $n = 3$ excited levels are populated by electron impact excitation from the ground ($2p^6$) state of the neon-like ion which is produced in the plasma heated by the pumping laser. The population inversion between $2p^5 3p$ and $2p^5 3s$ levels develops because of the large difference between the radiative decay rates.

In 1985, at the LLNL in the United States the first clear demonstration of a soft x-ray lasing was published [MHR⁺85] at wavelengths in the range of 20.63 and 20.96 nm from the neon-like selenium plasma.

In neon-like ions, soft x-ray lasing has been observed with silicon ($Z = 14$, [LLPF97]) to silver ($Z = 47$, [FWS⁺92]) at wavelengths between 87 and 8 nm. The required pumping intensity for short wavelength extension of the neon-like x-ray laser is very high, i.e. 10^{16} W/cm² for gadolinium at 4 nm [RLH88].

The first demonstration of a discharge-pumped ultraviolet laser at 46.9 nm was done in 1994 [RST⁺94]. A fast capillary discharge having a 10–90% current rise-time of 20 ns, 40 kA was used to excite plasma columns up to 12 cm in length in 4 mm channels, producing population inversion in the $J = 0-1$ of neon-like argon and resulting in a gain of 0.6 /cm at 46.9 nm wavelength.

The nickel-like scheme, proposed firstly in [MHR85] has proved to be successful for short wavelength amplification below 10 nm [MMH⁺87, MMS⁺90] at the Lawrence Livermore National Laboratory (LLNL) reaching water win-

dow wavelengths using a several kJ green pump laser. With this scheme, the pumping intensity can be reduced significantly, since the quantum efficiency (the laser transition energy/the excitation energy) of the nickel-like system is much higher than that of the neon-like system.

In 1997, the British group published two papers on the saturated amplification nickel-like soft x-ray lasers including samarium at 7.3 nm and silver at 14 nm [ZMN⁺97, ZML⁺97].

Up to this time (1997) the pump pulses used for XRL were of the order of nanosecond, so the above mentioned lasers were working in the QSS regime.

In the nineties the transient excitation method was proposed [AS89, AS90] which has several attractive properties such as (a) the inversion in this scheme can occur at arbitrary electron density and it increases with larger electron density, (b) the gain coefficient in this scheme is several times higher, less sensitive to the details of the kinetic model. This scheme works in the rapidly ionizing plasma where the recombination processes are weaker, (c) there are no restrictions to an active media dimension, (d) pumping laser energy requirements are impressive, i.e. it is enough to provide only 0.1–0.3 J in a few hundred ps pulse and 1 J in 1 ps or 10 J in 10 ps pulse for a neon-like iron ion soft x-ray laser at 20 nm.

The group at Max Born Institute in Germany demonstrated the first TCE XRL system at 32.6 nm in Ne-like Ti using a nanosecond long prepulse and a short main pulse of the order of picosecond [NSK⁺97]. There was a significant reduction in the pumping power needed for inducing lasing so this new pumping method opened the way to XRL for few-Joule laser systems.

Significant progress was registered for both CE QSS and TCE XRL schemes up to present. The shortest wavelength saturated TCE XRL (7.3 nm in Ni-like Sm) was reported in [KPM⁺01] while for QSS systems this is 5.86 nm in Ni-like Dy [STZ⁺99]. TCE also allowed to generate shortest XRL pulses (2 ps) [KJR⁺02]. Spatial coherence was improved in oscillator amplifier schemes like reported in [NTN⁺03] for a TCE XRL or in [ZFS⁺04] where a hybrid HHG oscillator - plasma amplifier was demonstrated.

In 2003 another important step in reduction of the pumping energy needed was achieved in the GRIP (GRazing Incidence Pumping) scheme. The principle of the method relies on the fact that the electron density in the lasing region is of the order of 10^{20} /cm³ while the energy deposition is made at critical density, which is $1.1 \cdot 10^{21}$ /cm³ for 1054 nm pumping laser wavelength when the pumping is made at normal incidence on the target. In this way the absorption of the pump pulse is taking place several tens of micrometers away from the gain region where it is needed. The solution was found in a well known formula [Elt90, Eli02] which is stating that the turning point electron density for a laser pulse propagating in a plasma with linear

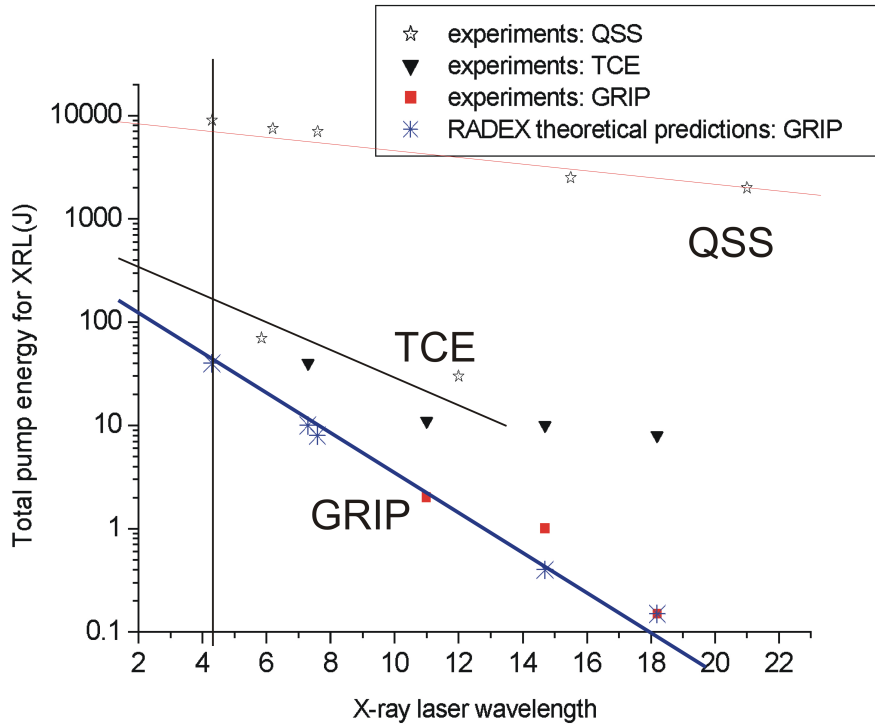


Figure 1.3: Comparison of different XRL species in terms of pump energy needed to achieve a given wavelength. The upper QSS points represent the early experiments at LLNL, USA, while the lower ones represent the best results obtained with QSS at those wavelengths with Quasi-Steady State scheme. The red triangles are experiments with close to normal pumping geometry in TCE scheme, reported by Dunn and his coworkers between 1998-2003 together with the shortest saturated TCE XRL wavelength (reported at VULCAN in Rutherford, UK). The squares are experimental results using GRIP pumping method during the last three years by Dunn, Rocca and their teams while the blue crosses are theoretical predictions for GRIP scheme made by RADEX code.

density profile is smaller for larger incidence angles according to the simple relation

$$n_e = n_{ec} \cdot \sin^2 \alpha$$

where n_{ec} is the critical plasma electron density and α is the incidence angle on target. Using pumping angles between 10° and 30° , the energy of the pump laser can be deposited in the density region where the gain appears (of the order 10^{20} /cm³).

To have a clear overview over the CE XRL progress in the last 20 years we refer to fig. 1.3 where experimental results obtained in QSS, TCE and GRIP pumping methods are compared in terms of pump energy needed for achieving laser at a given wavelength. The upper points in the plot represent experiments in early nineties in USA for QSS scheme; the triangles show the experimental results obtained in TCE scheme while the squares represent results of the GRIP method compared with the theoretical predictions of the RADEX code (the crosses).

Modelling of the XRL is based on magnetohydrodynamics (MHD) codes for plasma description like RADEX, EHYBRID and MEDUSA coupled with rate equations programs for the plasma ionization and population inversion dynamics and with laser propagation codes that are helpful for analyzing the gain of the XRL. However, analytical description of the processes it is important for gathering the simple picture of the processes involved. Such an analytical model, proposed in [LZ01, LLZ02] explained for example Ni-like Pd XRL results obtained in [DOS+98, DLO+00].

For the GRIP pumping method analytical models are not yet fully developed. While preplasma dynamics (generated with the first pumping pulse, also called prepulse) and the free expansion of the plasma are analytically described in the model mentioned above, description of the specific effects due to grazing incidence main pulse pumping are poorly modeled.

In this thesis results from a GRIP transient collisionally pumped Ni-like zirconium x-ray laser at the recently built multi-Joule Terawatt laser at GSI-Darmstadt are presented, pointing out various important laser-plasma interaction issues that contribute to the good understanding of this pumping method. The analytical model of [LZ01] is extended with the numeric approach in order to understand the absorption of the main pulse in the plasma which is the distinguishing feature of the GRIP method.

1.4 Synchronization of the accelerators with PHELIX

Spectroscopy experiments at the accelerator require, at the same time, spectral, thermal and temporal overlap of the laser pulses with the ion bunches to be excited. Spectral overlap of the monochromatic XUV radiation with the $2s_{1/2}$ - $2p_{1/2}$ transition in the Li-like ions is provided by a matching of the ion velocity to provide the needed Doppler shift. However, spatial and temporal overlap of the ion bunch with the laser pulses have to be achieved, too. Experiments performed at the 100 TW laser facility of the Ecole Polytechnique in France proved that the XRL reaches the pointing stability required by the experiments [Neu03]. Spectral bandwidth requirements were demonstrated in previous experiments [PZR+01].

The temporal overlap of the XRL pulse with the ion bunch requires the synchronization of the PHELIX laser with the high frequency phase of the accelerator structure. The design of the synchronization procedure has to take into account the timing and real-time diagnostic of different subsystems in PHELIX and in the accelerators infrastructure. The accuracy of the temporal overlap is below 1 ns.

PHELIX laser operation is controlled through an object oriented program named PCS (PHELIX Control System) based on a GSI developed LabView framework. In addition, PHELIX Interlock System (PILS) is an independent program which controls the safety regulations in the lab. Both are slow control systems without assurance for the real-time reaction. As a consequence a hardware synchronization scheme was developed employing minimum interaction with the PCS and PILS. A typical working procedure with PHELIX starts with the launching of the PILS program which controls the state of the window and of the doors in the building and allows, among other things, to turn on the lasers. Then PCS is activated, monitoring in this way various parameters of the laser. When all the safety procedures are fulfilled, a PHELIX shot is initiated by the PCS. The PCS writes all necessary timing parameters in the programmable delay generators devices and then triggers the shot. After the trigger is initiated, PCS can not stop anymore the shot via software. However, the real-time evolution of the process is implemented in hardware components, the so called "fast synchronization system" (FSS).

FSS manages the distribution of all trigger signals to the PHELIX subsystems with the needed accuracy, down to less than 1 ns and should manage real-time feedback from the critical subsystems. The difficult part is to synchronize it to external devices with their own time flow control systems like in the case of the accelerator [UKT+05].

The heavy ion synchrotron (SIS) at GSI will be taken as an example in the following as it is representative for the synchronization procedure of the PHELIX XRL Li-like ions spectroscopy experiments. In a similar way with PHELIX it has different levels of real-time control of the ion bunch production and delivery. All the major events in this process are broadcast via a so called timing bus cable to all users. The typical temporal accuracy is in the range of $5 \mu s$ but the events generation includes asynchronous steps. The position of the bunch in the ring can be controlled with ns accuracy via the high frequency (HF) system. The HF system has to be triggered at the right time with sub-nanosecond accuracy when needed. Up to now this has not been done and is the aim of BuTIS project to make such sub nanosecond synchronization possible as an important step toward the planned extension of the accelerator facility at GSI. PHELIX-SIS synchronization is the first test for this scheme.

Up to now the design of the PHELIX laser using femtosecond front-end synchronization with the ring accelerators at GSI has been accomplished. Cabling and basic diagnostics devices are in place. The first tests are planned for beginning of 2006. Description of the synchronization with the SIS as depicted using SysML (Systems engineering Modeling Language [SP05]) is presented in appendix A.

Chapter 2

Principles of Transient Collisionally Excited X-Ray Laser

Plasma X-ray lasers are developed at the interface of several physics disciplines: laser physics for the development of the pump sources, atomic physics for the characterization of the active medium at microscopic level, plasma physics for the macroscopic understanding of the gain medium, electrodynamics for the description of the properties of the coherent x-ray radiation which develops along the amplification medium. This chapter starts with an overview of the laser-plasma interaction and then gives a theoretical description of the x-ray lasers pointing out key issues for each of the main parts of our laser: optical pumping, active medium, properties of the x-ray emission.

2.1 Plasma creation for XRL

The generation of the active medium for an XRL is a dynamic process. In the original TCE scheme [NSK⁺97, DOS⁺98], one uses two pulses to irradiate a solid target. The first pulse (named prepulse) will create a highly ionized plasma (named preplasma), the second pulse (named main pulse) will create population inversion in this plasma as depicted in fig. 2.1. As it is shown in the right side of the figure, the main pulse is shorter in time and as a consequence has a reduced spatial extension when compared with the prepulse. It also arrives at the target with a tilted amplitude front, generating in this way a traveling heated region along the preplasma line. This traveling heated region can be associated with the gain region of the XRL. Because of the short lifetime of the population inversion it is important that this region

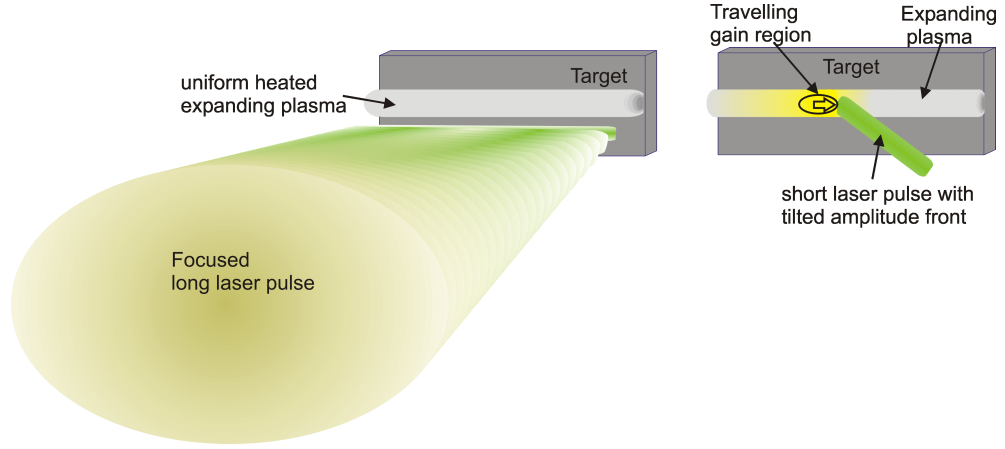


Figure 2.1: Prepulse is reaching the target creating the plasma; the tilted amplitude short main pulse is creating locally in the plasma a gain region which travels along the plasma line

is, moving at a given speed close to the velocity of light, denoted as traveling wave (TW) speed. In the standard TCE scheme only the amplitude front is tilted relative to the target while the wave vector \vec{k} of the main pulse is normal to the target. In the GRIP scheme the wave vector of the main pulse is tilted to large angles relatively to the normal at the target.

Further in fig. 2.2 a side view of the process is presented. The peak to peak delay between the main pulses is shown. The electron plasma density generated on the target surface is presented in gray levels. It is assumed that it takes an exponential shape in the region of interest as it will be explained in this section.

Following a simple model, one can obtain a very useful scaling law for the plasma density and scale length. It is exposed here briefly following reference [LZ01]. The starting point is a 1D time dependent single fluid model for the description of the electron component dynamics in the plasma. The continuity equation for compressible fluids written for ions is:

$$\partial_t \rho(x, t) + \partial_x \rho(x, t) \cdot v(x, t) = 0 \quad (2.1)$$

where $\rho(x, t)$ is the average ion mass density and $v(x, t)$ is the velocity field. Further, the local momentum balance is determined by the gradient of the pressure field $p(x, t)$:

$$\rho(x, t) (\partial_t v(x, t) + v(x, t) \partial_x v(x, t)) = -\partial_x p(x, t) \quad (2.2)$$

The local energy balance has to be written using the potential energy

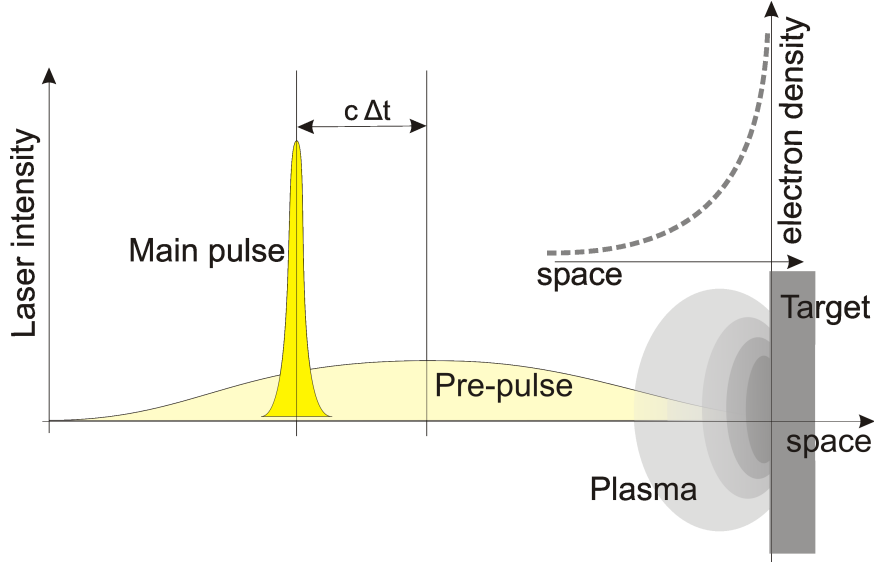


Figure 2.2: Schematic representation of the TCE XRL: laser pulses intensities, the target and the plasma electron density are represented in the spatial extension

$\epsilon(x, t)$ and the heat flow $h(x, t)$:

$$\begin{aligned} & \partial_t \left(\rho(x, t) \left(\epsilon(x, t) + \frac{v(x, t)^2}{2} \right) \right) = \\ & -\partial_x \left(\rho(x, t) v(x, t) \left(\epsilon(x, t) + \frac{v(x, t)^2}{2} \right) + p(x, t) v(x, t) \right) + \rho(x, t) h(x, t) \end{aligned} \quad (2.3)$$

The electrons in the plasma is are considered to form an ideal gas and as a consequence one can write the following equations of state(EOS) for the pressure and for the internal energy density:

$$p(x, t) = p_0 Z(t) \Theta(t) \rho(x, t) \quad (2.4)$$

$$\epsilon(x, t) = \epsilon_0 Z(t) \Theta(t) \quad (2.5)$$

where $\Theta(t)$ is the electron temperature in eV and $Z(t)$ is the average ionization degree of the plasma. The parameters with index 0 (like p_0 and Z_0) are constants taking care of the non dimensionalization and are analyzed later. Note that in this way one assumes constant temperature over the whole plasma, which is a relatively good approximation in the case of moderate energy nanosecond long laser pulses generating the plasma.

The empirical equation for the average charge state can be written as follows:

$$Z(t) = Z_0 \Theta(t)^{1/3} \quad (2.6)$$

and one further searches a self-similar solution for the velocity field:

$$v(x, t) = v_0 (\Theta(t) Z(t))^{1/2} + \frac{x}{t} \quad (2.7)$$

where the first term on the right hand side of the equation 2.7 is the speed of sound in the plasma.

One can get now a simple differential equation by replacing the relations 2.4, 2.5, 2.7 and 2.6 in equation 2.2:

$$\frac{\partial_x \rho(x, t)}{\rho(x, t)} = -\frac{v_0 (3 \Theta(t) + 2 t \partial_t \Theta(t))}{3 p_0 \sqrt{Z_0} t \Theta(t)^{4/3}} \quad (2.8)$$

where it is assumed that all the parameters, the electron density and the temperature have strictly positive values. The equation 2.8 finds an exponential solution along the x coordinate which allows to introduce a scale length of the plasma density as the coefficient of the exponential as follows:

$$\frac{1}{L(t)} \equiv -\frac{\partial_x \rho(x, t)}{\rho(x, t)} = \frac{v_0 (3 \Theta(t) + 2 t \partial_t \Theta(t))}{3 p_0 \sqrt{Z_0} t \Theta(t)^{4/3}} \quad (2.9)$$

where

$$\rho(x, t) = \rho_0(t) \exp\left(-\frac{x}{L(t)}\right) \quad (2.10)$$

The coefficient $\rho_0(t)$ can be obtained by integrating the electron density and with the assumption that this will provide the total ablated mass, labeled further $M(t)$.

$$M(t) = \int \rho(x, t) dx = \frac{\rho_0(t)}{1/L(t)} \quad (2.11)$$

For the total ablated mass another formula of the mass ablation rate derived in [GEK⁺92] can be used which is valid for the ablation process of the thick slab target irradiated by a nanosecond laser pulse in the approximation of high average charge state:

$$M(t) = \frac{m_0 I^{2/3} t^{2/3}}{Z(t)^{3/2} \Lambda^{1/3}} \quad (2.12)$$

By replacing eq. 2.6 in eq. 2.12 and then in eq. 2.11 one can parametrize the electron density as function of the laser intensity noted I :

$$\rho(x, t) = \frac{I^{2/3} m_0 t^{2/3} e^{-x/L(t)}}{\Lambda^{1/3} Z_0^{3/2} L(t) \Theta(t)^{1/2}} \quad (2.13)$$

where the $L(t)$ and $\Theta(t)$ have to be determined using the energy conservation relation 2.3.

In the energy equation one has to introduce an explicit form for the absorption term $h(x, t)$. The main absorption process for laser absorption in dense plasmas is considered to be the inverse Bremsstrahlung mechanism. The formula for inverse Bremsstrahlung is obtained using the formula for the opacity k_{IB} :

$$k_{IB}(x, t) = k_0 \frac{\Lambda \lambda^2 Z(t) n_e(x, t)^2}{\Theta(t)^{3/2} \sqrt{1 - \frac{n_e(x, t)}{n_{ec}(\lambda)}}} \quad (2.14)$$

In the above formula $n_e(x, t) = n_{e0} \rho(x, t) Z(t)$ represents the electron density of the plasma at a given point x at the time t , λ is the laser wavelength, $n_{ec}(\lambda)$ is the critical density of the plasma given by the formula:

$$n_{ec}(\lambda) = \frac{m_e c^2}{2\lambda^2 e^2} \quad (2.15)$$

where m_e is the electron mass and e is the electron charge. In this way the square root in the opacity formula defines the plasma refraction index for the pumping laser wavelength.

Integrating over the spatial coordinates one obtains the total absorbed laser energy, assuming a positive scale length for the plasma and a constant Coulomb logarithm:

$$\tau_{IB} = \int k_{IB} dx = \frac{k_0 n_{e0}^2 \Lambda M(t)^2 Z(t)^3}{L(t) \Theta(t)^{3/2} \left(1 + \sqrt{1 - \frac{n_e(x, t)}{n_{ec}(\lambda)}}\right)} \quad (2.16)$$

and in the approximation of the square root close to zero which is fulfilled in the density regions close to critical density this can be approximated with the well known formula:

$$\tau_{IB} = \frac{k_0 n_{e0}^2 \Lambda M(t)^2 Z(t)^3}{L(t) \Theta(t)^{3/2}} \quad (2.17)$$

Finally one can write the source term in the energy equation, if one assumes that the $\tau_{IB} < 1$, as:

$$h(x, t) = \frac{I \tau_{IB}}{M(t)} \quad (2.18)$$

where it is clear that the source term introduces nonlinearity in the energy equation 2.3 through the $L(t)$ term (contained also in the $M(t)$ term).

With all the above approximations and notations the relation 2.3 becomes now a second order differential equation for the time dependent temperature.

Selecting a power law form of the solution and choosing the real one within the set of possible solutions one obtains:

$$\Theta(t) = 62^{1/3} \frac{m_0^{1/3} v_0^{1/3} n_{e0}^{2/3} k_0^{1/3} \Lambda^{2/9} \lambda^{2/3} I^{5/9}}{(44\epsilon_0 p_0 + 54p_0^2 - 62\epsilon_0 v_0^2 + 14p_0 v_0^2 - 31v_0^4)^{1/3}} t^{2/9} \quad (2.19)$$

As expected, this solution does not depend on the Z_0 proportionality factor in equation 2.6. Further, one can write the form of the plasma scaling law which fully characterizes the plasma density profile:

$$L(t) = \frac{27 \cdot 2^{2/9} m_0^{2/9} Z_0^{1/2} p_0 n_{e0}^{4/9} k_0^{2/9} \Lambda^{4/27} \lambda^{4/9} I^{10/27}}{31^{7/9} v_0^{7/9} (44\epsilon_0 p_0 + 54p_0^2 - 62\epsilon_0 v_0^2 + 14p_0 v_0^2 - 31v_0^4)^{2/9}} t^{31/27} \quad (2.20)$$

The coefficients in the above equations should be now identified. For ideal plasmas $p = \frac{\rho}{M_i} Z \cdot k_B \cdot \Theta$ is one of the equations of state (EOS); M_i is the mass of one ion, k_B is the Boltzmann constant. So $n_e = \frac{\rho}{M_i} Z$ is the electron numerical density. $\epsilon = \frac{1}{2} \xi n_e k_B \Theta$ where ϵ is the internal energy density, ξ is the number of degrees of freedom and is taken usually 3 and sometimes can be 4 if there is a magnetic field which introduces another degree of freedom. The speed of sound is $v_0 = \sqrt{p/\rho}$. As a consequence one can write:

$$p_0 = v_0^2 = 2 \frac{\epsilon_0}{\xi} = \frac{k_B}{M_i} \quad (2.21)$$

$$n_{e0} = \frac{1}{M_i} \quad (2.22)$$

and for the proportionality factor of the average ionization Z_0 from eq. 2.6 one finds in literature [CT73] the average ionization dependence of the plasma electron temperature for laser pulses which fulfill $n_e \cdot t < 10^{11} - 10^{12} \text{ s/cm}^3$:

$$Z = \frac{2}{3} (A\Theta)^{1/3} \quad (2.23)$$

where Θ in this case is the temperature in eV and A is the atomic mass number.

The m_0 factor is, according to [GEK⁺92], given by the relation

$$m_0 = 5.494 M_i^{7/6} \quad (2.24)$$

The solutions for scale length and temperature can now be simplified; The scaling with different physical parameters is in general a power law with exponent smaller than unity or very close to unity. This means that small percentage variations of the physical parameters are producing smaller percentage changes in the temperature and in the scale length.

In conclusion one recovers the scaling laws for the temperature, scale length and initial density of the plasma from [LZ01]

$$\Theta(t) = 1.86 \cdot 10^{-5} eV \cdot I^{5/9} A^{2/9} \Lambda^{2/9} \lambda^{2/3} t^{2/9} \quad (2.25)$$

$$L(t) = 2.75 \cdot 10^{-7} cm \cdot I^{10/27} A^{-2/27} \Lambda^{4/27} \lambda^{4/9} t^{31/27} \quad (2.26)$$

with the units W/cm^2 for laser intensity, micrometer for the laser wavelength and nanosecond for the pulse duration. A is the nuclear mass number.

One more simple relation can be extracted from 2.9 knowing the dependence of the temperature on the pulse duration:

$$L(t) = \frac{27}{31} \sqrt{p_0 Z_0} \Theta(t)^{1/3} t \quad (2.27)$$

and one can also write the coefficient $\rho_0(t)$ from eq. 2.10 as

$$\rho_0(t) = \frac{31}{27} m_0 I^{2/3} \Lambda^{-1/3} Z_0^{-2} p_0^{-1/2} \Theta(t)^{-5/6} t^{-1/3} \quad (2.28)$$

To get the full picture of the plasma creation and evolution one has to add the scaling laws for the plasma when the laser is switched off, at the moment t_{1L} , when the plasma expands adiabatically. According to [LZ01] the analytical scaling laws are obtained for this period using the condition before t_{1L} :

$$\Theta_{free}(t) = \Theta(t_{1L}) t_{1L}^{2/3} t^{-2/3} \quad (2.29)$$

$$L_{free}(t) = L(t_{1L}) t_{1L}^{-5/9} t^{5/9} \quad (2.30)$$

$$n_{0free}(t) = n_0(t_{1L}) t_{1L}^{7/9} t^{-7/9} \quad (2.31)$$

where $\Theta(t_{1L})$, $L(t_{1L})$, and $n_0(t_{1L})$ are the electron temperature, scale length, and reference electron density at t_{1L} and the time parameters are given in nanoseconds with the time axis origin at the beginning of the pre-pulse.

The relation 2.23 showing the dependence between the average charge state and the plasma temperature is a good approximation during the plasma heating with the laser. However, once the laser is switched off for periods of time of the order of nanosecond, the averaged charge state is not going down immediately following the decrease of temperature. So it is safe to assume that the average charge state stays constant after the laser is turned off although the temperature might decrease by a factor of two or more during the adiabatic expansion over one nanosecond.

2.2 Main pulse absorption in plasma for high laser fields

Having rules of the thumb for temperature and scale length of the plasma (eq. 2.25 - 2.31) one has to investigate next the interaction of the main pump pulse with the plasma. For this one has to elucidate how effective is the energy transfer to the plasma. As it will be seen in the following sections, this needs good understanding of the absorption mechanism and of the effects from the particular focusing geometry for the main pulse.

In the case of TCE XRL the main mechanism for laser absorption is the inverse Bremsstrahlung (IB). This is determined from the kinetic point of view by the collision frequency of the electrons in the plasma. At high laser intensities, e. g. $I > 10^{14} \text{W/cm}^2$ the large electric field of the laser will distort the thermal distribution of the electrons, thus changing the electron-ion collision frequency ν . In this cases, the electron mean square thermal velocity $v_{thermal}^2$, which appears in the collisional rate through the plasma temperature factor, is increased with the averaged squared electron oscillation velocity $v_{laser\ field}^2$ in the laser electric field which now is comparable to $v_{thermal}^2$.

$$v_{effective}^2 = v_{thermal}^2 + v_{laser\ field}^2 \quad (2.32)$$

This parameters regime is known as nonlinear IB due to the fact that the correction to the usual IB formula is made through a factor which is laser field dependent:

$$\nu = 2.91 \cdot 10^{-6} \frac{Z \cdot f \left(\frac{v_{laser\ field}^2}{v_{thermal}^2} \right) \cdot n_e \cdot \log \Lambda}{\Theta^{3/2}} \quad (s^{-1}) \quad (2.33)$$

where the electron temperature Θ is in eV and the electron density n_e is in cm^{-3} , Z is the average charge state and $f \left(\frac{v_{laser\ field}^2}{v_{thermal}^2} \right)$ is the correction factor for nonlinear IB.

To illustrate the correction factor, the figure 2.3 shows the IB correction factor f as a function of preplasma temperature for different laser intensities. The range for the laser intensities is typical to the main pulse in the TCE XRL schemes. The plasma temperature is represented on a logarithmic scale. At 10^{13}W/cm^2 there is little influence from the correction factor on the collision rate, while at 10^{15}W/cm^2 there is a significant decrease in the correction factor at temperatures below 100 eV.

To see that this factor can drastically affect the absorption the behavior of the coefficient at low plasma temperatures combined with strong laser fields is presented in 2.4 on a double logarithmic scale. At low preplasma

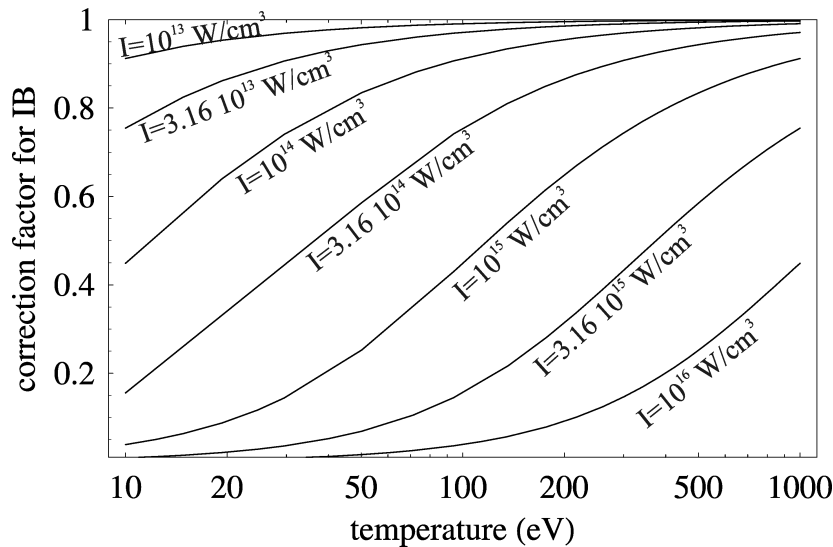


Figure 2.3: The inverse Bremsstrahlung correction factor for different pre-plasma temperatures and various laser intensities

temperatures the correction factor can decrease the collision rate down to a few percents of it's initial value. This effect clearly explains why the creation of the plasma from solid targets is so ineffective for short, intense laser pulses: the low plasma temperature and the high laser fields are inducing low collision rate through the correction factor. This dramatically decreases the absorption of the laser in the plasma. For this reason the introduction in the TCE method of a long pulse to create the plasma [NSK⁺97] proved to be very efficient in reducing the laser energy needed to pump the XRL.

The formula for the IB correction factor is a double integral for the case of the classical non-relativistic treatment of the electrons and is obtained using numerical integration. For the quantum or relativistic treatment things are more complicated but the result is similar to the classical non-relativistic case within 10 % [SW79]. Moreover the correction factor can be overestimated up to a factor of two if we consider the non-maxwellian distribution of the electrons in the plasma as demonstrated by [Lan80] and as a consequence the absorption of the laser in plasma is overestimated by the same factor. According to this paper, the additional factor to correct the absorption is given by formula:

$$f_L = 1 - \frac{0.553}{1 + \left(\frac{0.27v_{thermal}^2}{Zv_{laserfield}^2} \right)^{3/4}} \quad (2.34)$$

In the experimental data evaluation of chapter 4 this additional decrease of

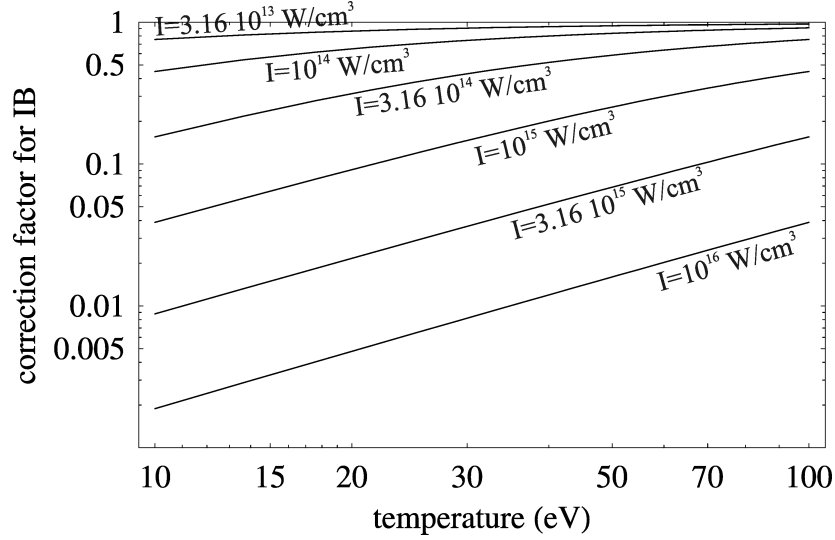


Figure 2.4: Double logarithmic plot of the IB correction factor at low pre-plasma temperatures

the IB factor will be included.

Taking into account the dependence of the collision rate on the average charge state of the plasma and on the correction factor (see eq. 2.33) it is useful to introduce for simplicity of further analysis a global factor in the collision rate denoted Zf :

$$Zf = Z \cdot f \cdot f_L \quad (2.35)$$

This factor has to be included for any evaluation of the laser propagation in plasma as we will see in the next section.

2.3 Laser propagation in plasmas

2.3.1 The complex refraction index of the plasma

The electromagnetic field propagating through a plasma will be reflected, refracted and absorbed. From the optical point of view one has the complex refraction index formula in order to quantify these processes. See the book of S. Eliezer [Eli02].

The equation of the propagation of a laser beam in the plasma can be written as [BW99, KBMD02]:

$$\frac{\partial}{\partial s} \left(n_{Cref}(x, y, z) \frac{\partial \mathbf{r}(x, y, z)}{\partial s} \right) = \nabla n(x, y, z) \quad (2.36)$$

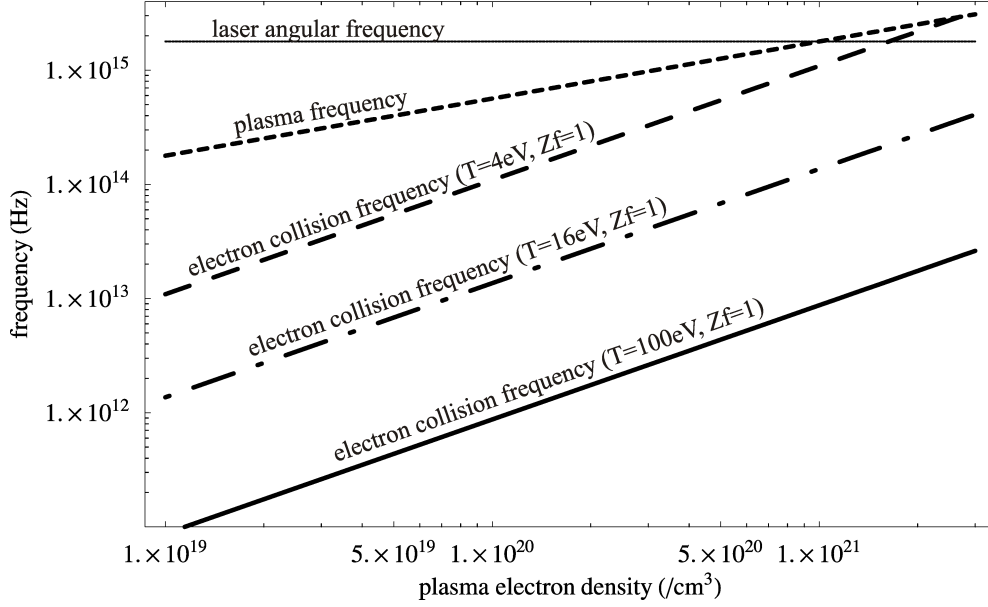


Figure 2.5: Laser frequency, plasma frequency and electron collision frequency dependence on density for pre-plasma temperatures of 4 eV, 16 eV and 100 eV assuming that the average charge state together with the IB correction factor contribute as unity

where $ds = \sqrt{dx^2 + dy^2 + dz^2}$ is the path element and $\mathbf{r} = (x, y, z)$ is the position vector, while $n_{Cref}(x, y, z)$ is the complex refraction index.

In order to solve this equation one has to compute the complex index of refraction. This is given by the following relations ([Eli02] p. 41-42):

$$\epsilon = 1 - \frac{\omega_{pe}^2}{\omega(\omega + \mathbf{i}\nu)} \quad (2.37)$$

$$n_{Cref} = \sqrt{\epsilon} = n_{ref} + \mathbf{i}n_{abs} \quad (2.38)$$

where ϵ is the plasma dielectric function, ω_{pe} is the electron plasma frequency, ω is the angular laser frequency, ν is the electron-ion collision frequency, n_{ref} is the real part of the refraction index and n_{abs} is the complex part of the complex refraction index so it determines the absorption in plasma.

In the figure 2.5 the frequencies which enter in the determination of the complex refraction index are represented as functions of the plasma electron density for the densities around critical density (eq. 2.15) which are of interest for the plasma x-ray lasers. The laser angular frequency for the wavelength 1054 nm is represented as a reference line. The plasma frequency in this plot is proportional with the square root of the density so in a double

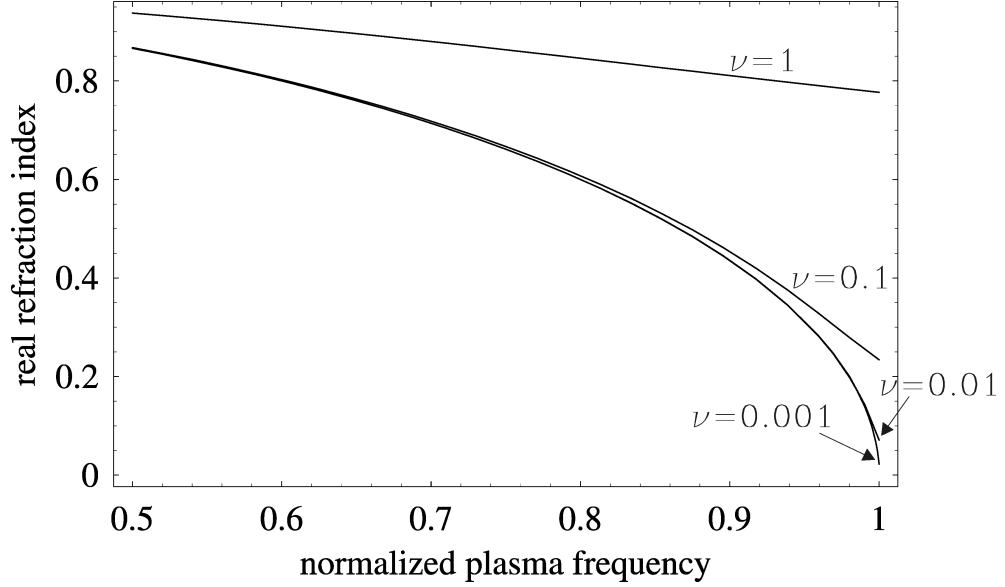


Figure 2.6: The real part of the refraction index as function of the plasma normalized frequency for different normalized electron collision frequencies

logarithmic scale looks linear. The place where this line crosses the laser angular frequency line defines the plasma critical density.

The plasma frequency in this electron density region is at maximum a factor of ten away from the laser angular frequency. For the electron collision frequency three reference lines were represented, corresponding to electron plasma temperatures of 4 eV, 16 eV and 100 eV. The last value is close to the typical temperature of the preplasma for XRL. For simplicity, the factor Zf which appears in the formula of the electron collision frequency has been chosen unity. It is observed that for low temperatures (4 eV) the electron collision frequency increases significantly compared to the high temperature curves by two orders of magnitude, being no more negligible compared to laser angular frequency or plasma frequency around the critical density. For higher plasma temperatures (100 eV) the electron collision frequency is 2-3 orders of magnitude below the laser frequency which allows to neglect it in the calculation of the refraction index.

To see this more clearly the normalized plasma collision frequency $\tilde{\nu} = \nu/\omega$ and $\tilde{\omega}_{pe} = \omega_{pe}/\omega$ are introduced. In this way - dropping the tilde sign - one can rewrite the real and the complex part of the refraction index:

$$n_{ref} = \frac{\nu\omega_{pe}^2}{\sqrt{2}(1+\nu^2)\sqrt{-1+\frac{\omega_{pe}^2}{1+\nu^2}} + \sqrt{1+\frac{\omega_{pe}^4-2\omega_{pe}^2}{1+\nu^2}}} \quad (2.39)$$

$$n_{abs} = \frac{1}{\sqrt{2}}\sqrt{-1+\frac{\omega_{pe}^2}{1+\nu^2}} + \sqrt{1+\frac{\omega_{pe}^4-2\omega_{pe}^2}{1+\nu^2}} \quad (2.40)$$

The real part of the refraction index is represented as a function of the normalized plasma frequency at different normalized electron collision frequencies ν in fig. 2.6. The normalized plasma frequencies correspond to electron densities from $0.25 \cdot n_{ec}$ to critical density n_{ec} . It is observed that for the small values of the ν , the real refraction index takes the shape of the well known formula

$$n_{ref} = \sqrt{1 - \omega_{pe}^2} \quad (2.41)$$

which is obtained from formula 2.39 taking $\nu = 0$.

The real refraction index differs by a factor of 3 or more when we change ν by a factor of 10, close to critical density. Because the real part of the refraction index enters in the differential equation 2.36, I chose to work with the formula 2.39 instead of it's simplified version 2.41.

Description of the refraction index in terms of normalized frequencies is advantageous due to the reduced number of parameters involved, but is not transparent in terms of magnetohydrodynamics parameters. In order to come closer to such a description one has to convert the normalized frequencies into electron density (ρ in the figure) and temperature T . The result is visualized in fig. 2.7 where the real part of the refraction index is represented as a function of plasma MHD parameters for electron densities less than the critical density and temperatures specific to the prepulse plasma. For the electron collision rate a Zf factor equal to 8 is assumed. The refraction index is decreasing fast at low temperatures along isodensity lines. It is close to unity at low temperatures and it goes to small values at higher temperatures; close to the critical density the reduction of the refraction index with the temperature increase is stronger than in the lower density regions. For a given temperature the refraction index tends to decrease from values close to unity at $10^{20}/cm^3$ to small values toward critical density. If one translates the simplified formula of the refraction index in terms of densities one obtains:

$$n_{ref} = \sqrt{1 - \frac{n_e}{n_{ec}}} \quad (2.42)$$

which is temperature independent. This is not the case for the extended formula 2.39 as clearly presented in fig. 2.7

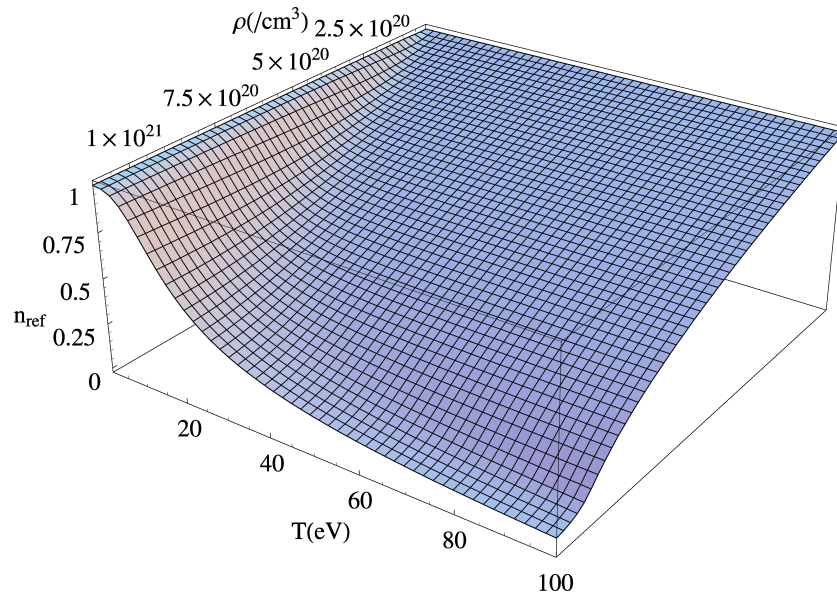


Figure 2.7: The dependence of the refraction index on the plasma density and temperature for $Zf=8$

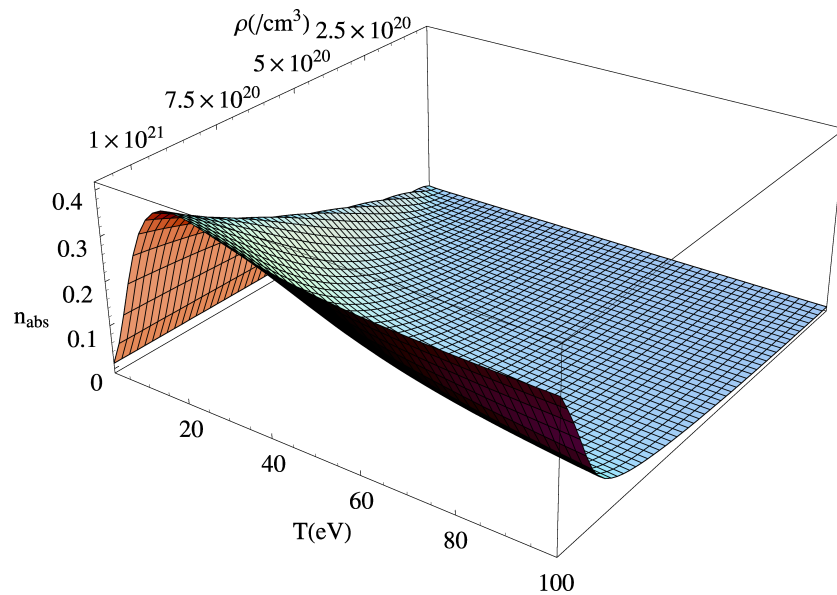


Figure 2.8: The complex part of the refraction index depending on temperature and plasma density, for $Zf=8$

With the above analysis of the real part of the refraction index it becomes clear that one can use the simplified formula 2.42 for the refraction index inserted in the propagation equation 2.36 to ray-trace the laser propagation in plasma with good chances to obtain an analytical solution, but in this case sensitivity to the temperature parameter is lost. Alternatively one can use the more elaborate formula 2.39 with the disadvantage of going numeric for the ray tracing. The second option is here adopted for the sake of a more careful description of the laser propagation in plasma.

2.3.2 Ray tracing of the main pulse including absorption

The results of the previous section 2.1 are used to describe the preplasma MHD. According to that, an exponential profile of the plasma is assumed with the z axis along the plasma line focus and with the x axis perpendicular to the target. In this case the refraction index depends only on the x coordinate and the propagation equation reduces to a set of two coupled differential equations:

$$\partial_{x(s)}n_{ref}(x(s)) \cdot (\partial_s x(s))^2 - 1 + n_{ref}(x(s)) \cdot \partial_s \partial_s x(s) = 0 \quad (2.43)$$

$$\partial_{x(s)}n_{ref}(x(s)) \cdot \partial_s x(s) \partial_s z(s) + n_{ref}(x(s)) \partial_s \partial_s z(s) = 0 \quad (2.44)$$

To solve the above equations one has to define the boundary conditions. α denotes the incidence angle on the target and the initial entrance point in the plasma is chosen to have zero coordinate. One can now write:

$$x(0) = 0 \quad (2.45)$$

$$z(0) = 0 \quad (2.46)$$

$$(\partial_s x(s))_{s=0} = -\cos(\alpha) \quad (2.47)$$

$$(\partial_s z(s))_{s=0} = \sin(\alpha) \quad (2.48)$$

This boundary value problem can be solved for an arbitrary initial plasma scale length and temperature and for a given incidence angle. α is the incidence angle of the main pulse onto the preplasma, and is the essence of the GRIP approach for the XRL.

In this work Mathematica 5.0 software is used to solve the BVP in an efficient manner. For a given set of parameters it takes one second to produce the solution on a computer with IntelPentium 4 processor at 2.4 GHz with

512 Mb DDR memory. One additional advantage is that the numerical solution can be graphically represented in the same environment using simple instructions. The BVP delivers the "trace of the ray" in the plasma so the next step is to compute the intensity of the ray at any point in plasma, using the complex part of the refraction index n_{abs} .

Similar to the real part of the refraction index, the imaginary part of the refraction index is represented in fig. 2.8 as a function of the MHD parameters temperature and electron density, denoted ρ in the figure. In the region up to 40 eV in temperature a feature is observed due to the fact that the electron collisional frequency (computed again with $Zf=8$) cannot be neglected at low temperatures, while at higher temperatures the complex part of the refraction index becomes almost constant for a given electron density. For a given temperature the index is increasing toward critical density, which, as expected, produces a stronger absorption of the laser light.

The local absorption scale length d_{abs} can be defined as following

$$d_{abs} = \frac{\lambda_0}{4\pi n_{abs}} \quad (2.49)$$

where the attenuation of the wave intensity (E^2) is exponential with the $1/e$ decay determined by d_{abs} .

The d_{abs} parameter is a function of the normalized plasma frequency and of the collision frequency. It decreases strongly at low collision frequencies, but is several orders of magnitude larger than the laser wavelength λ_0 , as depicted in fig. 2.9 (for calculations was used $Zf=8$). From the picture one can see that the the absorption scale length can easily take values over several orders of magnitude depending on the normalized electron collision rate and it is smaller towards the critical density of the plasma. For a clear view of the scale length, in fig. 2.10 a zoom is presented into the region of 0 to 200 micrometer for the same $Zf=8$. This is interesting especially for the fact that the typical plasma scale length is in the range of 20 - 50 micrometer. From this figures it is now clear that at high densities, close to critical density, the absorption is very effective in short distances whereas in the more diluted plasmas the laser pulse can propagate over distances of the order of a millimeter without strong reduction in intensity. The key role in this absorption belongs, as expected, to the electron collision frequency to which the absorption is very sensitive.

2.3.3 High intensity laser absorption in plasma

The change in intensity along the path defined by the solution of the BVP is obtained integrating

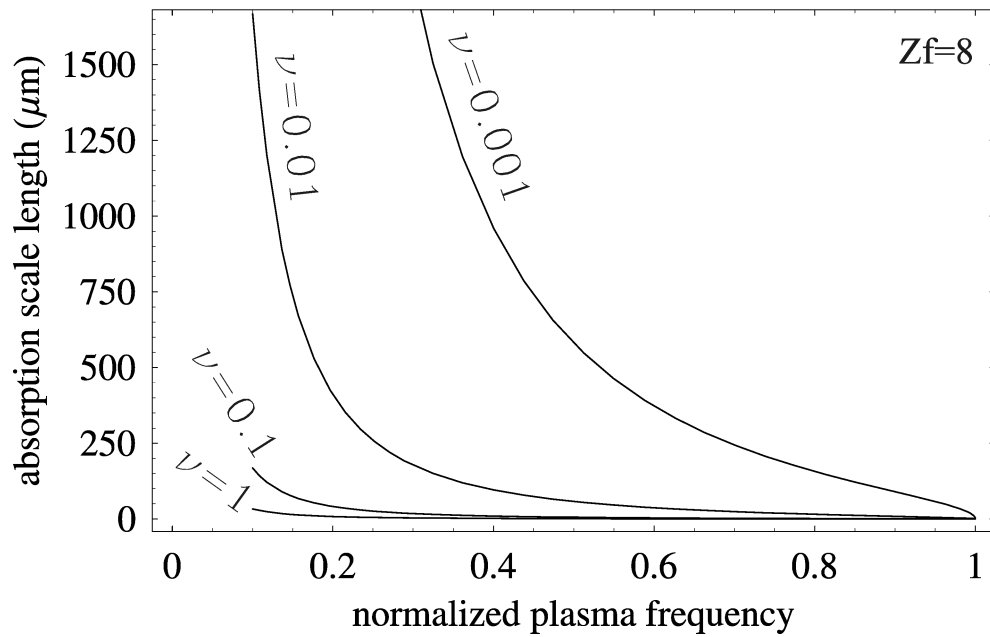


Figure 2.9: Absorption scale length as function of normalized plasma frequency for different normalized collision rates

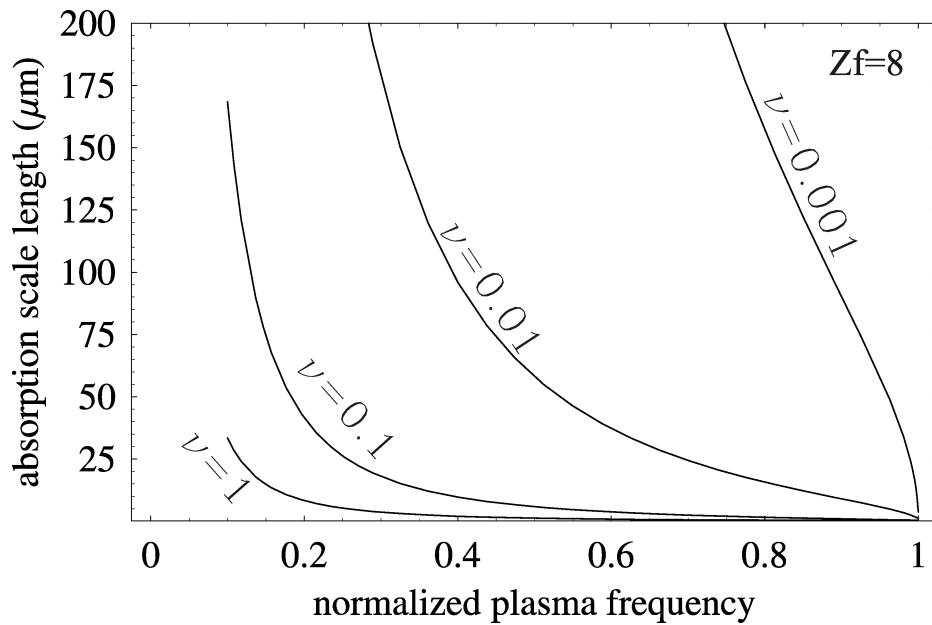


Figure 2.10: Detail of the absorption scale length as function of normalized plasma frequency for different normalized collision rates

$$I(s_0) = I_0 \cdot \exp\left(-\int_0^{s_0} \frac{ds}{d_{abs}(x(s))}\right) \quad (2.50)$$

where I_0 is the initial laser intensity and s_0 is a given place along the optical path.

Now one can describe any ray in the plasma using $x(s), z(s), I(s)$ functions which are providing the position and the transmitted intensity of a ray depending on the input plasma temperature, scale length and density at different incident angles.

The parametric analysis described above starts here by considering a fixed plasma temperature (30 eV) and density scale length (30 μm) which are typical values for the preplasma in the XRL, and varying the incidence angle from 10° to 80° in steps of 10° . For the normalized collision length an average charge state times inverse Bremsstrahlung correction factor of $Zf=1$ is used, obtaining the results from fig. 2.11. The unit on the spatial axes are centimeters but the axes are not scaled in the same way. Along the plasma the total length of the axis z is 800 microns while along the plasma gradient axis x is only 150 microns total length. The point 0 on the x axis corresponds to an electron density of $10^{19}/cm^3$. The rays are entering at this density into the plasma at the point $(x,z)=(0,0)$. On the vertical axis the transmitted intensity of the laser through the plasma is displayed, which reaches a point (x,z) on the ray path. The assumed initial laser intensity is taken equal to unity, meaning that there is no absorption of the laser light at densities below $10^{19}/cm^3$. One can observe that the transmission through the plasma decreases at large incidence angles in spite of the fact that the ray lengths are significantly longer at these angles.

The projection of the parametric plot on the horizontal plane delivers the ray trace in the plasma at different angles as shown in fig. 2.12.

Here one can see the penetration depth of the rays in the plasma varying from 125 microns for 10° incidence angle on plasma down to 50 microns at 80° incidence angle which means two to four scale lengths of the plasma ($L=30$ micron) penetration region. In the other direction the propagation takes place in a region from 60 micron to 770 micron depending on the incident angle. However, while the propagation in the plasma is significantly longer at large incidence angles the absorption along these ray paths is reduced as one can see in fig. 2.13. Here it is represented the transmission of the laser pulse along the x axis with the same conditions as mentioned for fig. 2.11. The ray enters in the plasma at the point $(x,transmission)=(0,1)$ and the total energy which has been deposited in the plasma can be evaluated from the transmission value at the same $x=0$ coordinate. For large angles the energy deposited in the plasma represents only 60% of the total energy. This shows

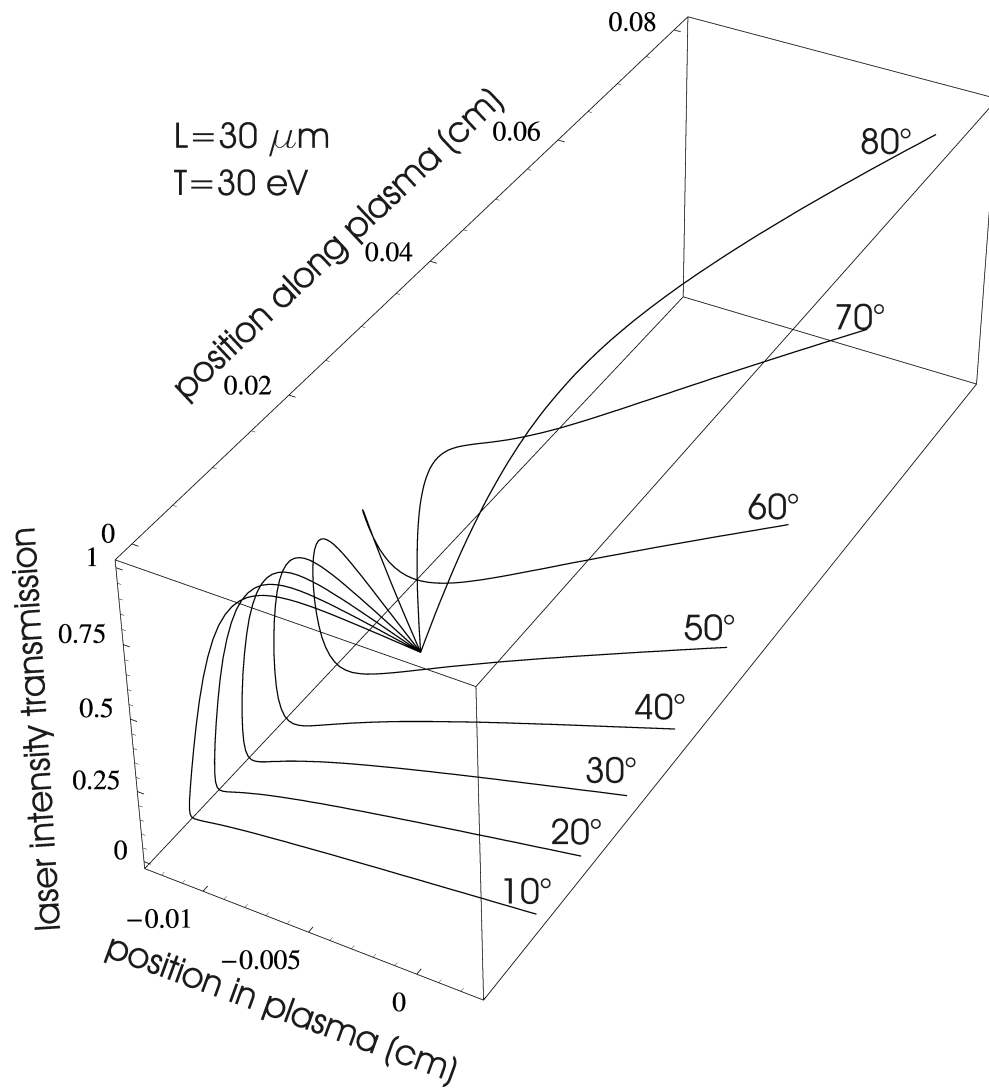


Figure 2.11: Parametric ray-tracing of the beam including intensity transmission at incidence angles from 10° to 80°

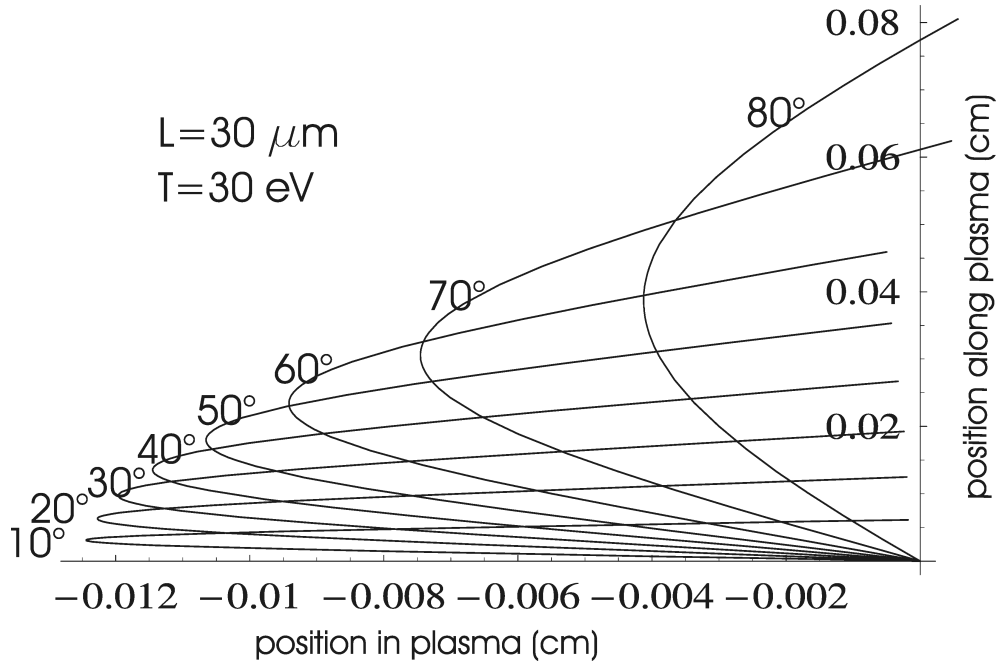


Figure 2.12: Ray tracing for various incidence angles on target, from 10° to 80° using different magnification factor for the two representation axes in order to resolve the penetration depth in the plasma

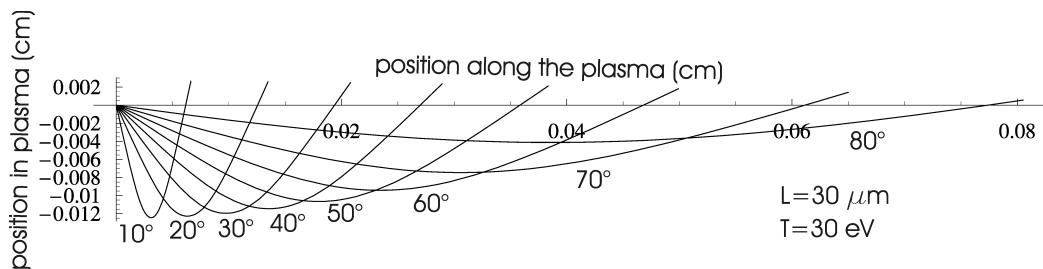


Figure 2.13: Ray-tracing for different incident angles on target using the same magnification factor for the two representation axes in order to provide a visual comparison of the optical paths lengths

that under certain conditions the coupling of the laser energy into the plasma will be inefficient for large incidence angles.

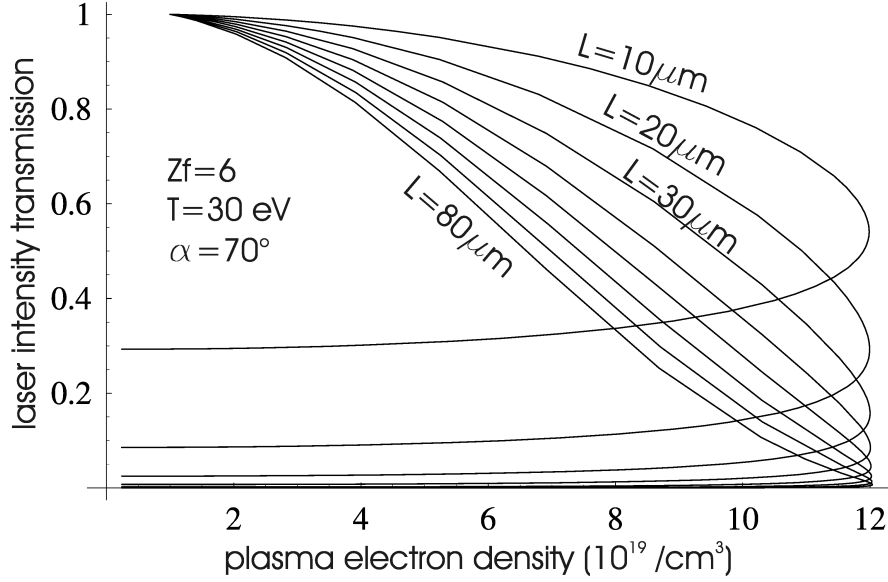


Figure 2.14: Transmission in the plasma as function of the plasma density for several plasma scale lengths

In fig. 2.14 a fixed incidence angle of 70° is chosen, and different plasma scale lengths are assumed, at constant electron temperature of 30 eV and $Zf = 6$. In this case the laser beam reaches the same plasma density region ($1.2 \cdot 10^{20}$) for all scale lengths. As a check of the ray tracing code one remarks that the electron plasma density at the turning point agrees well with the analytic formula [Tal03] which is applicable to any incidence angle for a linear electron density profile:

$$\cos \alpha = \sqrt{\frac{n_e}{n_{ec}}} \quad (2.51)$$

where the n_e and n_{ec} stand for electron density at the turning point and the critical density, respectively and the α is the incidence angle on the target.

The graphic 2.14 demonstrates that the scale length of the plasma can also give a significant effect on the absorption, with up to 30% of the energy of the laser being transmitted through the plasma for steep plasma gradients. This effect is attributed to the fact that the path in the plasma is significantly shorter in this case as clearly shown in fig. 2.15 where the raytracing of the main pulse in the plasma is represented under the same conditions.

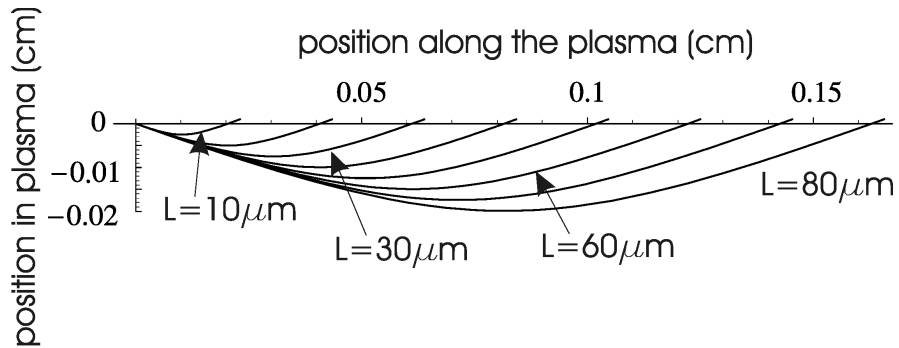


Figure 2.15: Ray tracing in the plasma for different plasma scale lengths

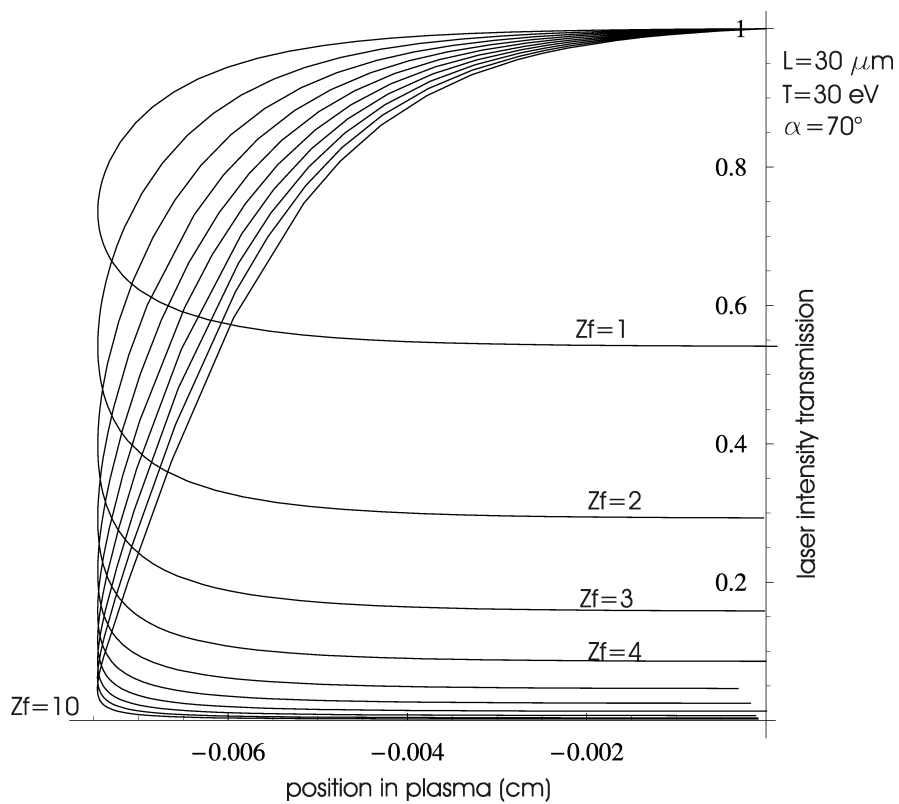


Figure 2.16: Transmitted intensity as function of the depth in the plasma for several Z_f values

For studying the effect of the Zf factor in fig. 2.16 the transmitted intensity through the plasma as a function of position in plasma at constant incident angle of 70° in a plasma with $30\mu m$ scale length and 30 eV electron temperature is represented. While the propagation trajectory of the laser pulse is the same in this condition, one can see a tremendous effect on the transmitted intensity. This increases to more than 50% for small Zf factors which would mean an inefficient use of the main pulse energy.

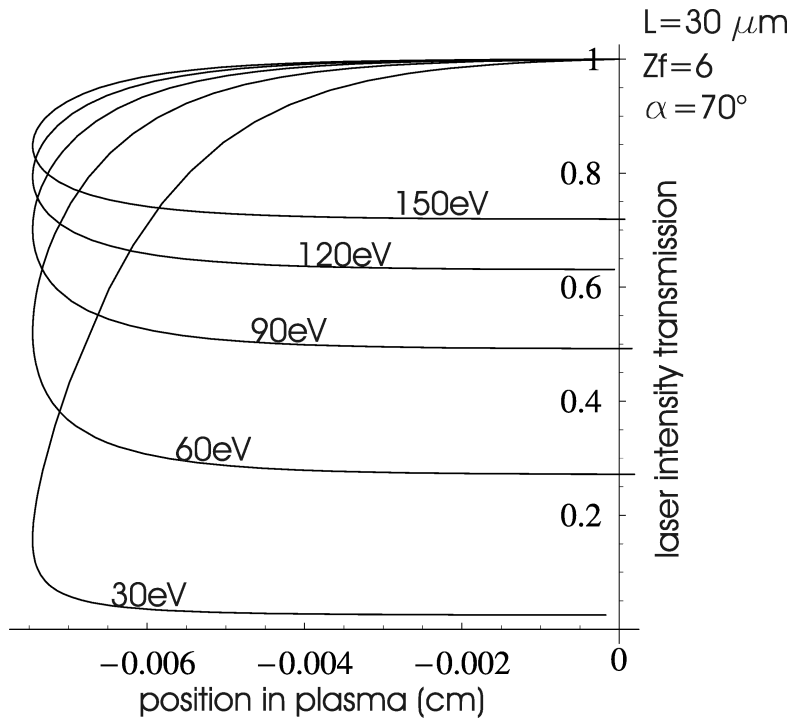


Figure 2.17: Transmitted intensity as function of the depth in the plasma for different plasma temperatures

One last parametric study is presented in fig. 2.17. The plasma scale length for this case is $30\mu m$ and $Zf=6$. The transmitted intensity is represented as a function of the position in plasma for different temperatures from 30 eV to 150 eV in steps of 30 eV. The transmitted energy strongly increases at higher temperatures up to 70 % from the total. This effect can be easily understood according to the electron-ion collision rate formula (eq. 2.33) which shows inverse proportionality with the temperature at the power $3/2$. This has as a direct consequence in a strong reduction of the absorption through the IB mechanism when the plasma temperature is increased.

In this section the effects of the variation of different parameters (laser incidence angle, plasma scale length, Zf factor, temperature) on the absorp-

tion of the main pulse in plasma were shown. Each of the parameters can produce significant effects leading to decreased absorption of the main pulse in the plasma. Unfortunately, the parameters are coupled in non-trivial way. As an example, plasma temperature, scale length and average ionization are interdependent and are indirectly controlled through the laser beam parameters. An analysis according to the experimental parameters will be presented in chapter 4.

2.4 Active medium

In the XRL the active medium is dynamically generated. In a first step, the Ni-like ion species are produced and then the population inversion within this species is induced using a strong laser field and thermal excitation.

Rate equations are used for modeling these two processes. Here a short description of the main issues regarding the modeling from the literature is given.

2.4.1 Ionization dynamics in nanosecond laser pulses

For laser produced plasmas we have two main categories of processes: collisional and radiative. They account for excitation, deexcitation, ionization and recombination. In the collisional part, electron-ion collisions are dominant compared to ion-ion collisions. So the autoionization and its inverse - dielectronic recombination are neglected.

Having this in mind, one can identify the type of equilibrium in the plasma. **Local Thermodynamic Equilibrium (LTE)** prevails when collisional excitation and ionization are balanced by their inverse processes, namely collisional decay and recombination. **Coronal model** can be used when detailed balancing does not hold, since collisional excitation and ionization are balanced by radiative processes: spontaneous line emission and radiative decay. In the **collisional - radiative model (CR)** the deexcitation and recombination occur through both their collisional and radiative forms.

It was shown in [CT73] that a collisional-radiative model may be applied to plasmas produced using nanosecond laser pulses if the electron temperature is above a few tens of eV. Above this temperature one can relate the average charge state Z of a given ion species to the electron plasma temperature.

The rate equations for the CR model can now be written as:

$$\begin{aligned} \frac{\partial n_{z+1}}{\partial t} = & n_e n_z S(z, T_e) \\ & - n_e n_{z+1} [S(z+1, T_e) + \alpha_r(z+1, T_e) + n_e \alpha_{3b}(z+1, T_e)] \\ & + n_e n_{z+2} [\alpha_r(z+2, T_e) + n_e \alpha_{3b}(z+2, T_e)], \end{aligned} \quad (2.52)$$

where $S(z, T_e)$ is the collisional ionization coefficient, $\alpha_r(z, T_e)$ is the radiative recombination coefficient and $\alpha_{3b}(z, T_e)$ the three body recombination coefficient for the charge state z and electron temperature T_e . The coefficients are given by the following relations:

$$S(z, T_e) = \frac{9 \cdot 10^{-6} \xi_z \cdot (T_e / \chi_z)^{1/2}}{\chi_z^{3/2} (4.88 + T_e / \chi_z)} e^{-\chi_z / T_e} \quad (cm^3/s) \quad (2.53)$$

$$\begin{aligned} \alpha_r(z, T_e) = & 5.2 \cdot 10^{-14} \left(\frac{\chi_z}{T_e} \right)^{1/2} z \left(0.43 + \frac{1}{2} \log \left(\frac{\chi_z}{T_e} \right) + 0.47 \left(\frac{T_e}{\chi_z} \right)^{1/2} \right) \\ & (cm^3/s) \end{aligned} \quad (2.54)$$

$$\alpha_{3b}(z, T_e) = 2.97 \cdot 10^{-27} \xi_z / T_e \chi_z^2 (4.88 + T_e / \chi_z) \quad (/s) \quad (2.55)$$

where ξ_z is the number of electrons in the outermost layer corresponding to the state of charge z and χ_z is the ionization potential. An important result has been derived in the case of the stationary state for electron temperatures larger than 30 eV. The average charge state becomes density independent and the relation 2.23 holds [CT73].

2.4.2 Ni-like ions rate equations

The schematic representation of the levels in Ni-like systems is presented in fig. 2.18. During the heating of the plasma via the main pulse, both the 4p and 4d levels are populated by electron collisional excitation. The 4p-3d decay is much faster than the 4d-3d transition because the last one is forbidden, so that a population inversion builds up. The lasing transition is the 4d-4p transition and the lower level of this decays to 3d state via fast radiative decay.

The use of the average charge states for the ionization dynamics from neutral up to Ni-like ions is motivated by the fact that large numerical errors are introduced in detailed level computations. The computational time will also be extremely large in this case. However, for analyzing the creation of

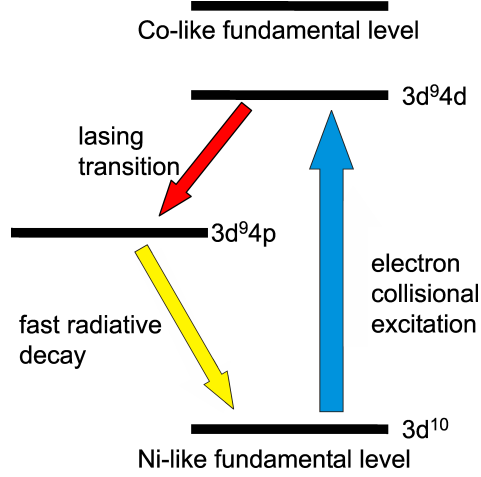


Figure 2.18: Energy level representation for Ni-like ions indicating the collisional transition and the lasing line

population inversion in Ni-like ions, such detailed computations are carried out.

For this, the higher energy levels in the ion are considered in LTE, because they fulfill the following relation:

$$n_e \geq 1.9 \cdot 10^{16} T_e^{1/2} E_{ik} \quad (cm^{-3}) \quad (2.56)$$

where the n_e is the electron density and E_{ik} is the transition energy in eV between level i and level k of an allowed radiative decay. The above condition was obtained assuming that collisional de-excitation is ten times greater than radiative de-excitation. It is clear now that collisional processes tend to dominate the population of quantum states when the energies of the states are close together and when the electron density is high. There is always some energy level close to the ionization limit of the ion where the more closely spaced higher energy levels are in LTE with each other. This level is often referred to as the "collision limit". It moves closer to the ground state as the electron density increases. For x-ray lasing to occur, at least the lower quantum state involved in the lasing process must be below the collision limit [Tal03].

For the other levels one has to go for detailed rate equations considering the relevant populating and de-populating collisional and radiative processes. Collisional excitation from one state i to another state k occurs at a rate

$$R = n_e n_z K(i, k) \quad (2.57)$$

where $K(i, k)$ is the rate coefficient obtained by averaging the cross-section for the collisional excitation process over the Maxwellian distribution of speeds of

the free electrons. For collisional transitions between levels for which electric dipole radiative transitions are allowed one has:

$$K(i, k) = 64\pi^2 \left(\frac{\pi}{3}\right)^{1/2} \left(a_0^3 \frac{E_H}{h}\right) \left(\frac{E_H}{k_B T_e}\right)^{1/2} \left(f_{ik} \frac{E_H}{E_{ik}}\right) G_{ik} e^{-E_{ik}/(k_B T_e)} \quad (2.58)$$

with h the Planck constant, $G_{ik} \approx 1$ the Gaunt factor for the transition, E_H the hydrogen atom ionization energy, a_0 the Bohr radius and f_{ik} the oscillator strength.

For collisional excitation between levels where the electric dipole radiative transition is forbidden we have [DNI⁺97, Tal03]:

$$K(i, k) = 1.58 \cdot 10^{-5} \frac{\gamma_{ik}(T_e) e^{E_{ik}/T_e}}{E_{ik} \sqrt{T_e}} \quad (cm^3/s) \quad (2.59)$$

where the temperature and the transition energy are in eV and

$$\gamma_{ik}(T_e) = n \cdot (A_0 + A_1 \ln(T_e/E_{ik}) + A_2 (\ln(T_e/E_{ik}))^2 + A_3 (\ln(T_e/E_{ik}))^3) \quad (2.60)$$

with the values of n , A_0 , A_1 , A_2 and A_3 are tabulated in reference [DNI⁺97].

For the de-excitation rates one has to use the following relation:

$$K(k, i) = \left[\frac{g_i}{g_k} e^{E_{ik}/(k_B T_e)} \right] K(i, k) \quad (2.61)$$

where the g_i and g_k are the degeneracies of the two energy levels.

The rate of radiative de-excitation between two quantum states k and i is given by $A_{ki} n_k$ with n_k the population density in the k level and A_{ik} the Einstein coefficient. If absorption of the radiation is important, the effect of photo-excitation can be taken into account by introducing the idea of the "net radiative bracket". Rather than attempting a detailed ray tracing of the radiation emission and absorption, the radiative de-excitation is written as $A_{ki} n_k T_{ki}$ where T_{ki} is the net radiative bracket which can take values from zero (complete absorption of the radiation) to one (no absorption of the radiation). The net radiative bracket is related to the "escape factor" which is the fraction of radiation emitted that ultimately escapes the plasma without absorption.

2.5 Properties of the x-ray laser emission

The spectral line shape of the XRL emission is determined by the broadening process dominating in the gain region. With a Maxwellian electron velocity

distribution one obtains for Doppler broadening the following Gaussian line shape:

$$f_D(\nu) = \frac{2(\ln 2)^{1/2}}{\sqrt{\pi}\Delta\nu_D} \exp \left[-4 \ln 2 \left(\frac{\nu}{\Delta\nu_D} \right)^2 \right] \quad (2.62)$$

where ν is frequency in the emitted line and $\Delta\nu_D$ is the full width at half maximum (FWHM) of the line, given by the formula:

$$\Delta\nu_D = 2(\ln 2)^{1/2} \frac{1}{\lambda} \left(\frac{m_{ion}}{2k_B T_{ion}} \right)^{-1/2} \quad (2.63)$$

with m_{ion} the ion mass and T_{ion} the ion temperature.

For a natural or collisional broadening dominated emission, the line shape is Lorentzian:

$$f_L(\nu) = \frac{2}{\pi\Delta\nu_L} \frac{1}{1 + (2\nu/\Delta\nu_L)^2} \quad (2.64)$$

with the FWHM of the spectral line due to natural broadening given by:

$$\Delta\nu_L = \frac{1}{2\pi} \left(\sum_i A_{ui} + \sum_i A_{li} \right) \quad (2.65)$$

where A_{ui} are Einstein coefficients for the transition from the upper lasing level u to all the possible lower levels i , and A_{li} are Einstein coefficients for the transition from the lower lasing level l to all the possible lower levels i .

Further one can investigate the dependence of the XRL emission intensity along the gain region. While the process is initiated by spontaneous emission one can write the equation of radiative transfer as follows:

$$\frac{\partial I(z, \nu)}{\partial z} = G(\nu)I(z, \nu) + E(\nu) \quad (2.66)$$

with the spontaneous emission term $E(\nu)$ given by:

$$E(\nu) = n_u A_{ul} f(\nu) h\nu \frac{\Omega}{4\pi} \quad (2.67)$$

where the n_u is the population in the upper lasing level, $f(\nu)$ is the emission line shape and Ω is the appropriate solid angle of the amplified spontaneous emission, while $G(\nu)$ is the gain coefficient given by:

$$G(\nu) = f(\nu) \frac{\lambda^2}{8\pi} A_{ul} \left(n_u - \frac{g_u}{g_l} n_l \right) \quad (2.68)$$

where λ is the wavelength of the lasing line and n_l is the population on the lower lasing level.

With the Linford approximation [LPSS74] one obtains from the above equations:

$$I_{tot}(z) = I_0 \cdot \gamma \frac{(e^{G(0)z} - 1)^{3/2}}{(G(0)ze^{G(0)z})^{1/2}} \quad (2.69)$$

For Gaussian line profiles $f(\nu)$, $\gamma = 1$. Other sharply peaked line profiles are also well approximated by this equation. Lorentzian profiles, for example, have $\gamma = \pi^{-1/2}$.

When writing the eq. 2.66, one assumes that spontaneous emission is random in direction, phase, polarization and frequency (weighted over a line shape function). This can be overcome by using seeded schemes. In several experiments oscillator amplifier schemes were used. In a TCE scheme, XRL output was improved in beam divergence, by 2 - 3 times, and peak intensity, by up to one order of magnitude, when compared with a single plasma column of the same length or longer [DOF+02, NTN+03]. A recent breakthrough was the use of HHG to seed an OFI XRL [ZFS+04]. The paper reported a tabletop soft X-ray femtosecond laser operating at 10 Hz and exhibiting full saturation, high energy, high coherence and full polarization. This injection technique allowed to measure the gain evolution in time with sub-picosecond accuracy [MSM+05].

The temporal evolution of the emission of the XRL is much harder to be theoretically described, while it involves an accurate knowledge of the plasma MHD, ion wave-function and atomic properties, sophisticated rate-equations and ray tracing codes.

The straightforward solution is to look at experiments. For QSS schemes, XRL pulse durations in the range of 50-100 ps are observed while the gain lifetime is exceeding 200 ps [RMP+02]. In the case of TCE, the shortest pulse measurement reported was 2 ps for Ni-like Ag XRL [KJR+02] while with the HHG seeding there are hopes to obtain shorter pulses [ZFS+04]. An extended analysis of the pulse duration measurement for TCE Ni-like Pd XRL was reported in [DSS+03]. The measured XRL pulse duration was from 4 ps to 8 ps while changing the duration of the main pump pulse from half a ps to 27 ps. Another result for single shaped pump pulse Ni-like Ag TCE XRL was reported in the range of 32 ± 3 ps without using traveling wave excitation [JLP+03].

Concerning the spatial beam profile and coherence one has to add that they are typically low in the original TCE proposal. However, there is a lot of improvement in the recent years due to the introduction of the seeding schemes mentioned above. Full spatial coherence has been reported in [NTN+03] while there is hope that the temporal coherence of the injected HHG will be transferred to the XRL in experiments similar to the one in ref.

[ZFS⁺04].

A picture of the spectral, spatial and temporal characterization of the plasma XRL with emphasis on the CE schemes was presented in this chapter. Beyond the extensive description of preplasma parameters and XRL active medium and emission properties, an extensive parametric analysis of the laser coupling in the plasma was performed for a wide range of parameters by means of a coupled analytical and numerical computation program developed for this work. The analysis shows that the interplay of the prepulse and main pulse parameters can produce different effects on the laser-plasma coupling, no global optimal configuration being possible. They are serving as a guide through the next chapter where the experimental results obtained with TCE Zr XRL at PHELIX are presented.

Chapter 3

X-Ray Laser set-up with PHELIX

In this chapter a short description of the experimental set-up for the plasma XRL experiments is given. It starts with a presentation of the PHELIX (Petawatt High Energy Laser for heavy Ions eXperiments) laser system with accent on the sub-systems used in our experiments: femtosecond front-end, the preamplifier and the 10 J compressor. Then the focusing systems for the pre and main pulse are described, together with the diagnostic instruments used.

3.1 PHELIX laser

PHELIX laser is a high energy high power pulsed laser built using the MOPA Master Oscillator Power Amplifier architecture at Gesellschaft für Schwerionenforschung institute in Darmstadt, Germany. It consists of several sub-systems (see figure 3.1): pulses are formed in two alternative front-end systems which both deliver up to 50 mJ pulse energy; the next stage of amplification, the preamplifier, can amplify one of the two front-ends pulses to about 10 J nominal energy; a third amplification level, the main amplifier, is designed to provide enough energy to achieve petawatt range compressed pulses using pulses from the femtosecond front-end; a fourth amplification level, named booster, is under consideration to provide up to 4 kJ in long pulses (using the nanosecond front-end). Due to the necessity to use Nd:Glass amplifiers for the high energy stages the operating wavelength of the whole system, including the Ti:sapphire short pulse front-end, is 1053 nm. The short pulse front-end incorporates a single grating pulse stretcher. Compression of the optical pulses for the XRL experiments is achieved after

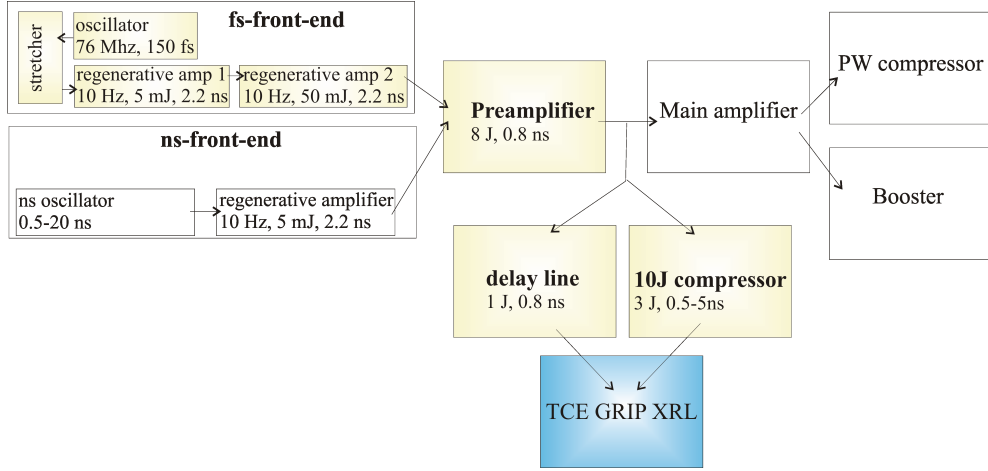


Figure 3.1: Schematic representation of the PHELIX laser system: the bold fonts show the subsystems in use for GRIP XRL

the preamplifier in a 10 Joule double pass single grating compressor. For petawatt operation a single pass compressor after the main amplifier stage is under construction. Fig. 3.2 shows the layout of the ground floor from the PHELIX building, where the optical subsystems are located. A more detailed description of the subsystems is provided in the following subsections.

3.1.1 The front-ends

The oscillator for the short-pulse front-end (fs-front-end) is a commercial Kerr-lens mode locked 150 fs Ti:sapphire oscillator (corresponding to 11 nm bandwidth)(Coherent Mira), running at 1053.7 nm wavelength pumped with a Nd:YVO₄ laser (Coherent Verdi). The repetition rate of the oscillator is determined by the length of it's tunable cavity to about 76 MHz. The cavity length is stabilized to an external frequency standard. With the average power in the range of 350 mW, the energy of single pulses is in the range of 4.4 nJ.

The pulses are sent to a grating stretcher similar to the one described in [BPY+00]. The holographic gold diffraction grating has 1480 lines/mm, and is used as first and second grating in a standard stretcher design. The advantage of this configuration is that the gratings are automatically aligned parallel. The 1:1 telescope of the stretcher is made in reflection, using a spherical mirror with curvature radius of 387.6 cm and a diameter of 152.4 mm and two mirrors, one in the grating plane (on the same substrate with the two diffraction gratings) and one in the focal plane. The oscillator laser

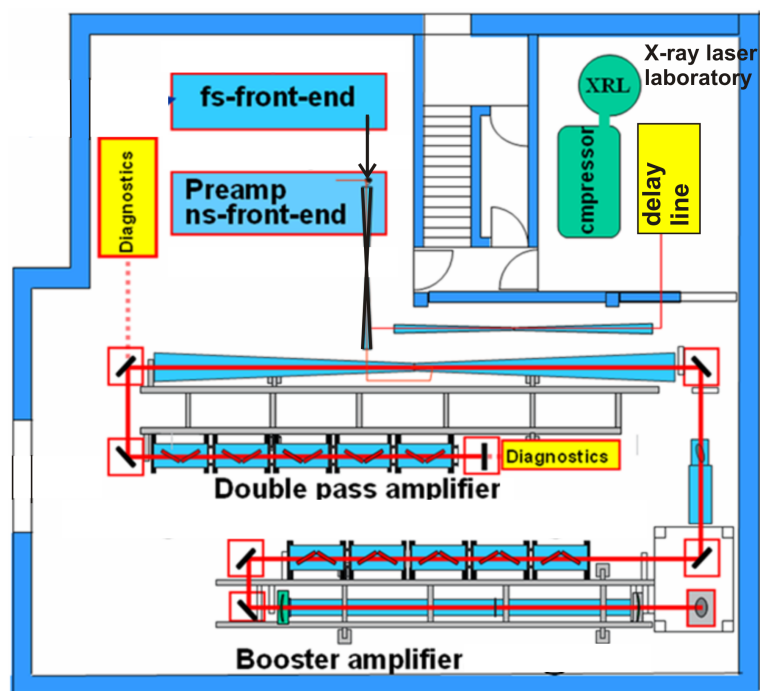


Figure 3.2: PHELIX building ground floor layout with the position of the main subsystems indicated

pulse hits the grating at an angle of 46° and is diffracted toward the spherical mirror placed 97 cm away. The dispersion of the stretcher is determined numerically using ray-tracing. The pulse broadening is evaluated to be 201 ps/nm and the transmitted bandwidth is 16 nm, limited by the dimension of the spherical mirror.

After the stretcher, the repetition rate of the laser is reduced to 10 Hz and the selected pulses are further amplified in two regenerative amplifiers. The first one is based on a Ti:sapphire crystal with 25.4 mm length and 6.4 mm diameter with the end surfaces cut at Brewster angle, and has a linear cavity. The crystal is longitudinally pumped through both sides with 200 mJ laser pulses, second harmonic of a Nd:YAG-laser (Continuum PL8010) producing 3.2 J/cm^2 energy density. The stretched oscillator pulse, at this moment with perpendicular polarisation, enters into the cavity of the linear regenerative amplifier through reflection on the Brewster angle end surface of the crystal. Then a pockels cell rotates the polarization of the pulse in such a way that the pulse is transmitted through the cavity with minimum of reflections. After about 400 ns corresponding to about 40 round trips between the two mirrors of the cavity, a second pockels cell rotates the polarization of the pulse with 90° in total so that the pulse is reflected by a thin film polarizer out of the cavity with an energy of about 5 mJ.

In order to provide a wider beam waist, the second regenerative amplifier uses a ring cavity made of plane mirrors and a single lens with a focal length of 10 m and uses one pockels cell to couple in and out the pulse to be amplified. The Ti:sapphire crystal is pumped from both sides by 250 mJ pulses of second harmonic of a Nd:YAG laser (Continuum PL9010). After about 400 ns corresponding to 30 round trips in the cavity, the pulses reach the 50 mJ level, having standard deviation of the energy in the range of 2%. Due to spectral narrowing and clipping in the stretcher, the output bandwidth of the fs-front-end is only 8 nm. The beam profile is Gaussian, corresponding to TEM_{00} mode of the resonators. A Galilei telescope increases the beam diameter to 9 mm for injection in preamplifier.

The long-pulse front-end (ns-front-end) uses a fiber oscillator and fiber modulators to form arbitrarily shaped pulses of 0.5 ns to 25 ns duration with the same input energy. It follows the design of [BWBP96] and was developed in parallel with the front end oscillator for the National Ignition Facility [PBK⁺95].

The oscillator is a diode pumped Ytterbium doped fiber oscillator delivering 15 mW in continuous wave. Using an acousto-optic modulator, pulses of 100 ns are cut and sent for amplification in a further double pass diode pumped Ytterbium doped fiber stage, then the pulses are amplitude modulated using a free programmable pulse shape generator with 100 ps resolution

time. This allows to form especially shaped pulses for plasma generation and diagnostics. Finally, an 8 m cavity length regenerative ring amplifier with Nd:glass active medium pumped via two flash lamps is increasing the output energy of the ns front-end to 50 mJ. The maximum possible pulse duration of the front-end is limited to 25 ns due to the circumference of the ring cavity.

In the XRL experiments, the fs front-end together with the preamplifier stage is used due to the fact that it allows to obtain 10 TW pulses in the range of half of picosecond, as needed for the TCE XRL scheme.

3.1.2 PHELIX 10 Joule preamplifier

The preamplifier is a single pass Nd:glass system with two flash lamp pumped rods of 19 mm diameter and one of 45 mm diameter. It operates in single shot mode (1 shot in 3 minutes), increasing the energy of the laser pulses from 50 mJ to the 10 J range for a selected front-end pulse.

In the first section of the preamplifier, two pockels cells together with the corresponding Glan polarizers are used to select a given pulse from the front-end and to suppress the prepulses and the ASE pedestal which appear in the pulses due to the limited (100:1) contrast of the thin film polarizers in the regenerative amplifiers.

A serrated apodizer [AK94] in combination with a vacuum Kepler telescope with a pinhole which acts as a low-pass filter shapes the spatial beam profile to a super-gaussian of 6th-8th order, needed for efficient use of the gain media.

The two 19 mm heads, each 240 mm long, and separated by a pockels cell are then amplifying the pulses in the 1 J range. The rods are protected against back reflection from the next amplifier stage using a Faraday isolator. A further vacuum Kepler telescope magnifies the beam diameter for the third amplifier rod. This one has a diameter of 45 mm and also a length of 240 mm, and is passively isolated against back reflection from the main amplification stage using a Faraday isolator. After the preamplifier the bandwidth of the pulses is reduced to 5 nm (FWHM) due to the doped glass properties and gain narrowing. An adaptive mirror is implemented for phase front corrections after a further magnification of the beam diameter. This adaptive mirror is mainly serving as a precorrection for wavefront deformations in the main amplifier. It was not used for pumping the XRL because the beam quality of the preamplifier output was fully sufficient for this purpose.

The vacuum telescopes used in the preamplifier have three main functions: 1) they image the beam in such a way that the propagation of the laser pulse does not affect the beam profile; 2) the beam diameter is magnified to fit the useful aperture of each amplifier head and also to keep the pulse fluence

below the damage threshold of the optics; 3) each telescope with a pinhole in the focal plane can be used as low-pass filter for the spatial beam profile to clean the intensity spikes which might appear.

The repetition rate is limited by the cooling time of the three glass amplifier heads to one shot every 2 minutes. The cooling was independent for the 19 mm heads and for the 45 mm head with commercial water coolers regulated to better than one degree temperature variation. This temperature fluctuation alone, however, generated a thermal lens in the preamplifier, while heating from firing the flash lamps of the heads was removed in a short time. This problem was solved by regulating the head temperature to better than 0,2 degrees.

After the preamplifier, the pulses are transported to the main amplifier or alternatively to the X-ray laser laboratory via vacuum Kepler telescopes.

3.1.3 Main amplifier, petawatt compressor and booster

The main amplifier is of the disk type. The ten Nd:glass laser disks have a clear aperture of 31.5 cm, are 7 cm thick, and are mounted at Brewster angle in 5 amplifier heads. They are used in a double pass configuration. The components were provided by the former Phebus laser (CEA Limeil, France) and Nova laser (Lawrence Livermore National Laboratory, USA). The two-pass amplifier is presently under test and should give first hundreds of Joule shots in spring 2006.

The Petawatt compressor configuration was modelled intensively with different laser simulation programs. It is configured as a single pass compressor with dielectric gratings. The chirped pulses amplified to 500 J can be compressed to approximatively 0.5 ps. This system will become operative in 2006.

The booster is an additional amplifying level, similar to the main amplifier but single pass which will bring the energy of the laser to approximately 4 kJ/pulse.

Further XRL experiments are planned for beginning of 2007 using the main amplifier and the petawatt compressor. They investigate the possibility to scale the XRL wavelength to the water window range (2.2-4.4 nm) using the TCE scheme. Up to now the shortest reported saturated TCE XRL wavelength was 7.3 nm using Ni-like Samarium [KPM⁺01] with 50 J pump energy. For the experiments at PHELIX, 200 J pump energy will be available.

3.1.4 10 Joule Compressor

The 10 Joule compressor used for the present XRL set-up is a double pass single grating configuration. The gold holographic diffraction grating on a 16 inch substrate [SHC92] was manufactured by Lawrence Livermore National Laboratory. The diffraction efficiency is rather homogeneous over the whole surface and has an average measured value of 84 %. The damage threshold during experiments is specified as 200 mJ/cm². The incidence angle on the grating is 46°. The compressor can compress pulses of up to 15 J of energy. The total optical path in the compressor is about 18 m and can be varied using a translation stage for vertical roof mirror. In this way the pulse duration can be varied from a minimum of 350 fs up to 10 ps.

The angles of the two 90° roof mirrors are set using an autocollimator with an accuracy of 20 μ m. This is of great importance for the generation of the traveling wave excitation, as it is explained in subsection 3.2.1.

The whole set-up is placed in a specially designed vibration isolated vacuum tank which can reach 10⁻⁶ mbar pressure range in order to minimize the accumulation of phase nonlinearity in the optical pulse, and to prevent damage by surface contamination.

The duration of the compressed pulses is measured using a second harmonic generation single shot autocorrelator (SSAC) [GSH79, SGRB87] with a LiIO₃ crystal. The tilt of the amplitude front is measured using an inverted field autocorrelator (IFA) [PKW00]. This is a Mach-Zender interferometer in which one of the pulses is spatially inverted. The interference figure consists of fringes with the contrast function depending on the tilt of the pulse front. Using the 350 fs short pulses the tilt of the amplitude front of the pulse can be determined with an accuracy of 1 mrad with this IFA. The measurements are valuable for our GRIP XRL setup as will be discussed in subsection 3.2.1.

3.2 Experimental set-up

The XRL experiments in Ni-like Zr at PHELIX were performed in two campaigns with similar set-ups. The first one was using an incident angle on target of 45° for the main pulse. Results were presented in [Neu03, NSC⁺04, UCK⁺04]. In a second experimental campaign in summer 2005 an incidence angle on target of 72° was used (see fig. 3.3). This thesis concentrates on this second experiment, including from the first experiment only unpublished results which generate new understanding through comparison with those from the new data.

The XRL is pumped with pulses delivered by the PHELIX preamplifier.

The pump beam is split into two parts: 75% of the energy is entering in the compressor which re-compresses the pulse down to 400 fs. The transmission of the device is slightly better than 50%.

The remaining 25% of the energy are directly transported to the target. The duration of this un-compressed pulse is about 0.8 ns. It is passed through an 18 m long optical delay line in order to produce nearly the same optical path length as the travel distance in the compressor.

This nanosecond pulse is focused by a spherical lens with 1 m focal length and a cylindrical lens with 250 mm focal length to a line focus of ($30 \mu\text{m} \times 6 \text{mm}$) onto a Zr metal target. Here it serves to create a plasma column several hundreds of picosecond before the impact of the compressed pulse. Due to the ultra-high intensity of the short ps-pulse this plasma is rapidly heated, which leads to a non-stationary population inversion, with a high transient gain.

A singlegold coated, 6 inch diameter on-axis parabola, tilted at an incidence angle of 9 degrees is used to generate a line focus of $30 \mu\text{m} - 100 \mu\text{m}$ width and over 5 mm length. This geometry intrinsically leads to a tilt of the pulse front generating in this way the “traveling wave excitation” needed for the TCE XRL. The lifetime of the high gain in the transient collisionally pumped (TCE) scheme is typically in the order of a few picoseconds. Therefore the focused pulse front of the short pulse creating the population inversion in the plasma has to run along the plasma column with approximately the speed of light c to maximize the overlap of the x-ray pulse and the gain peak. The discussion of the focusing system is essential for understanding the peculiarities of the GRIP XRL scheme and is presented in next subsection.

Measurement of the line focus for both prepulse and main pulse are performed using a microscope objective attached to a video camera. The spatial line widths of the two pulses are determined in comparison with a calibrated target. The motorized compact device allows to monitor the overlap of the two lines over the whole length of the lines.

3.2.1 Focusing system characterization

There are several different focusing systems implemented for the generation of a line focus with traveling wave (TW) characteristics. Generation of a high quality line focus was extensively investigated in the eighties and nineties. Usually they work in reflection, using a combination of parabolic and spherical mirrors [RH85, HS98]. However, they do not automatically generate a TW excitation and besides, especially since at that time the importance of this feature was not yet recognized. The first TCE XRL was reported in

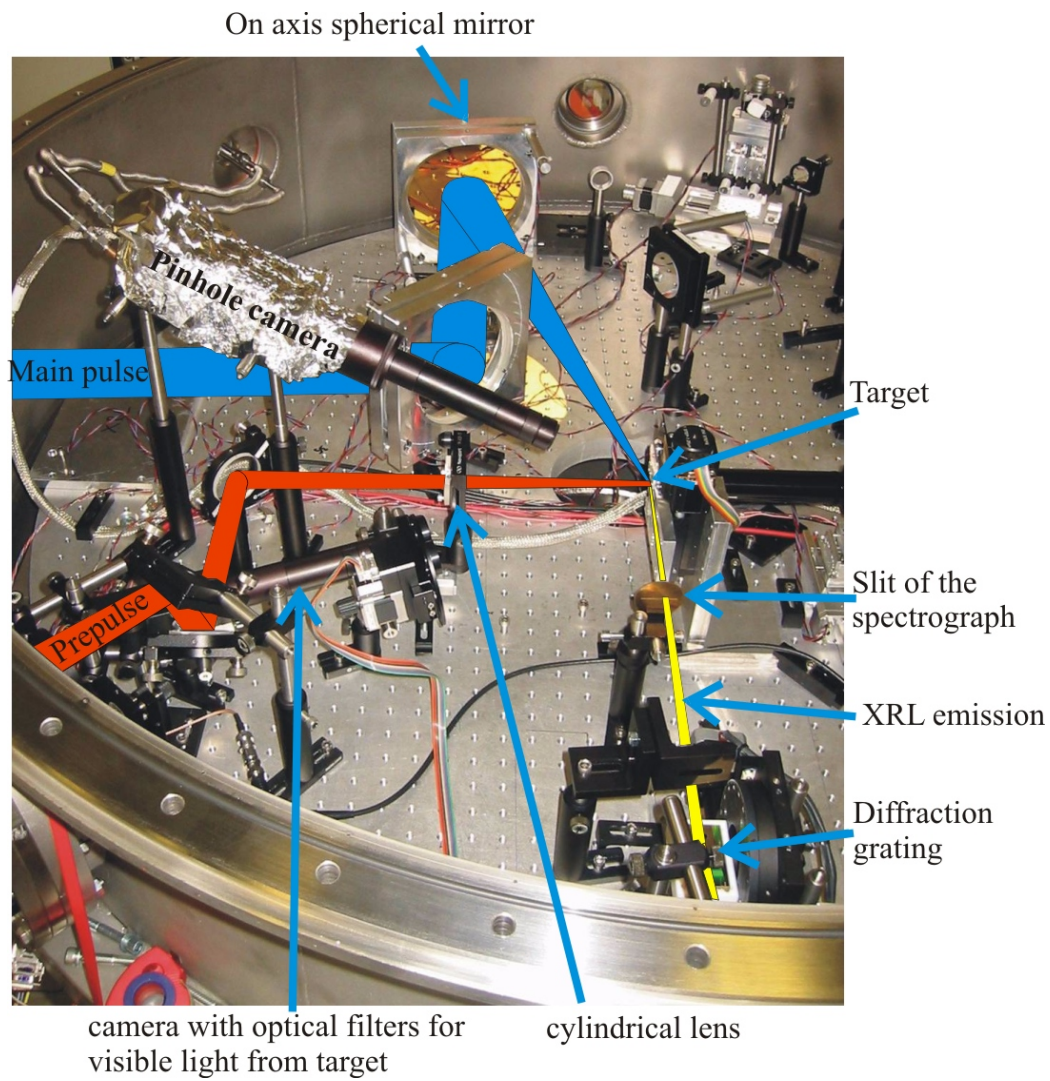


Figure 3.3: Experimental set-up picture with the focusing systems for pre-pulse and main pulse and part of the diagnostics

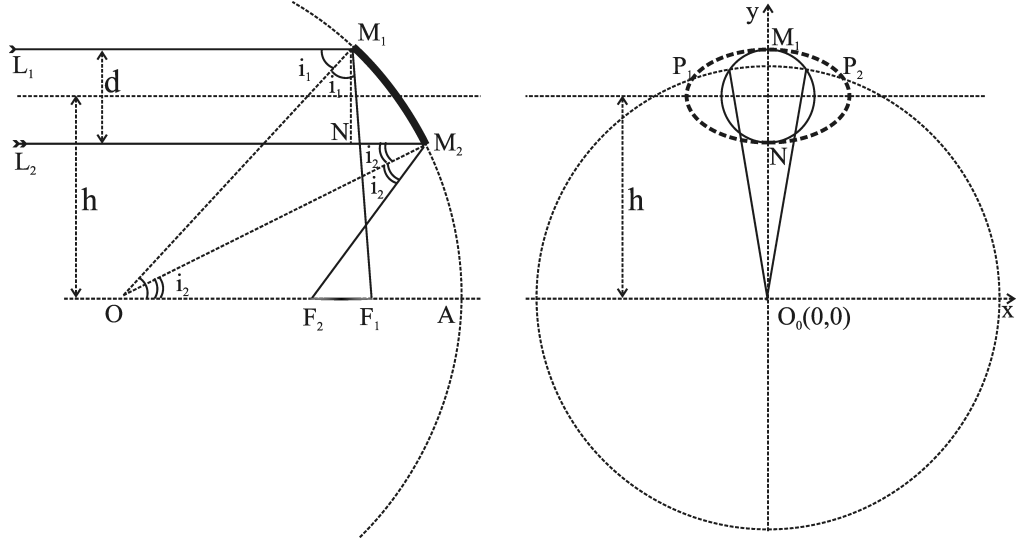


Figure 3.4: Representation of the main pulse focusing system used for deriving the analytical formula of the traveling wave and for the line focus length

1997 and even in that case no TW was used [NSK⁺97]. After that, the efforts to generate an optimal TW (close to the speed of light) went in several directions. Additional amplitude pulse front tilting can be generated in the compressor [CSS⁺00, KZR⁺00], using an additional grating before compressor [MNDS94, AATE⁺03] or using step mirrors (echelons) [JLP⁺03].

A significant step forward was made by a collaboration of GSI in Darmstadt and the Max Born Institute in Berlin which reported the first measurement of TW close to the speed of light produced by a much simpler scheme [NAdM⁺01, Neu03]. Here the optical aberration of only one spherical mirror is used to replace the previous complicated mixture of gratings, off axis parabolic mirror and on axis spherical mirror. (An especially complicated example can be found in [KPM⁺01].) This simple and efficient focusing system opened the way to the grazing incidence pumping scheme (GRIP) [KDS⁺03, KDP⁺05, LWL⁺05, RWL⁺05b, TJPN05].

The methods for generation of a line focus and TW were reviewed in [Neu03]. In addition, the analytical formulas are provided here which are of interest for any GRIP set-up as used also in the experiments reported in this work. The line focus length is computed here and then, for the first time, an analytical formula for the TW behavior under the tilted spherical mirror geometry is given.

The focusing system is represented in the left side of fig. 3.4. A parallel

laser beam is coming along lines $\overline{L_1M_1}$ and $\overline{L_2M_2}$ to the spherical mirror with center in O and radius $\overline{OA} = \overline{OM_1} = \overline{OM_2} = R = 2f$.

From rotational symmetry around the OA axis one can infer that all the rays coming at a given angle MOA relative to \overline{OA} will be reflected through the same focal point F. In this way one generates a line of focal points parallel with the laser beam incident on the spherical mirror.

$$L_1M_1 || L_2M_2 || OA \quad (3.1)$$

An incident laser beam is assumed to have diameter d at the distance h from the symmetry axis \overline{OA} . The line focus length $\overline{F_1F_2}$ is computed first.

The reflection law secures that the angles L_1M_1O and OM_1F_1 are congruent, while the radius $\overline{OM_1}$ is normal to the circle. Using relation 3.1, the triangles ΔOM_1F_1 and ΔOM_2F_2 have each two equal sides:

$$\overline{OF_1} = \overline{F_1M_1} \quad (3.2)$$

$$\overline{OF_2} = \overline{F_2M_2} \quad (3.3)$$

and as a consequence we can determine the \overline{OF} distances as

$$\overline{OF_1} = \frac{R}{2 \cos i_1} = \frac{f}{\cos i_1} \quad (3.4)$$

$$\overline{OF_2} = \frac{R}{2 \cos i_2} = \frac{f}{\cos i_2} \quad (3.5)$$

To determine the i angles one remarks that

$$\sin i_1 = \frac{h_1}{R} = \frac{h + d/2}{2f} = \sin i_0 + \frac{d}{4f} \quad (3.6)$$

$$\sin i_2 = \frac{h_2}{R} = \frac{h - d/2}{2f} = \sin i_0 - \frac{d}{4f} \quad (3.7)$$

where i_0 is the incidence angle on the middle of the mirror.

Using relations 3.4-3.7 one can determine the line focus length as:

$$\overline{F_1F_2} = \overline{OF_1} - \overline{OF_2} = \frac{f}{\sqrt{|1 - (\sin i_0 + \frac{d}{4f})^2|}} - \frac{f}{\sqrt{|1 - (\sin i_0 - \frac{d}{4f})^2|}} \quad (3.8)$$

and if the beam is incident only on one side of the \overline{OA} one can drop the modulus sign under the square root. In fig. 3.5 the line focus length is plotted for a focusing mirror of focal length 600 mm, as it was used in both

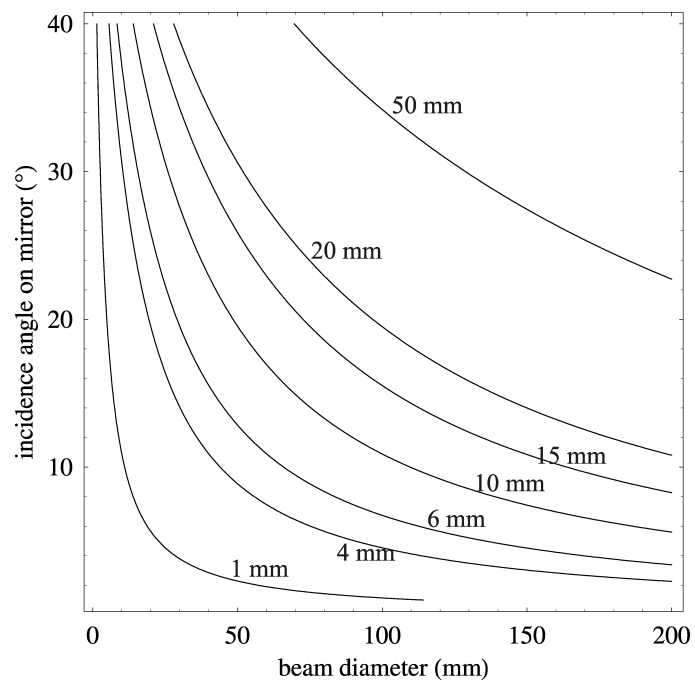


Figure 3.5: Contour plot of the line focus length generated with a 600 mm focus spherical mirror as a function of incident angle and beam diameter; the values on the curves represent the focal line length associated with that curve

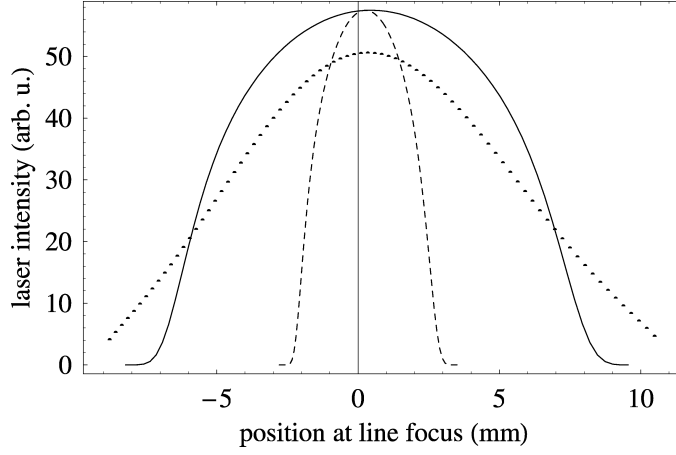


Figure 3.6: Line focus intensity distribution for 22.5° incidence angle using super-gaussian of 6-th order (straight line) and first order (dotted line) and for 9° incidence angle using 6-th order super-gaussian (dashed line)

XRL Zr experiments, for different incidence angles i_0 on the middle of the mirror and for various beam diameters.

Note that the line focus length formula 3.8 gives just a preliminary evaluation of the length of the focal line. One has to insert a realistic beam profile and to integrate along all the beam surface elements which are contributing with energy in a given point on the focal line. On the right side of the fig. 3.4 it is represented the plane perpendicular on OA containing the points M_1 and N . A round beam is marked with solid line while the spherical mirror projection is marked with thick dashed line. The points which are contributing with intensity to a certain point on the focus line are situated on the circle going through P_1 and P_2 , having origin in O_0 , due to rotational symmetry of the system.

The computed intensity distribution of the laser light along the line focus using numerical integration is represented in fig. 3.6.

To compute the average TW speed one has to evaluate the focal line length and divide it by the difference in the optical paths for the rays reaching F_1 and F_2 :

$$TW = \frac{\overline{F_1 F_2}}{\overline{M_1 F_1} - (\overline{N M_2} + \overline{M_2 F_2})} \cdot c = \frac{1}{\frac{\overline{N M_2}}{\overline{F_1 F_2}} - 1} \cdot c \quad (3.9)$$

where the relations 3.2 and 3.3 were used and the speed of light in vacuum is denoted with c . One can approximate the middle of arc $M_1 M_2$ with the middle of segment $\overline{M_1 M_2}$ and using the incidence angle on the middle of the

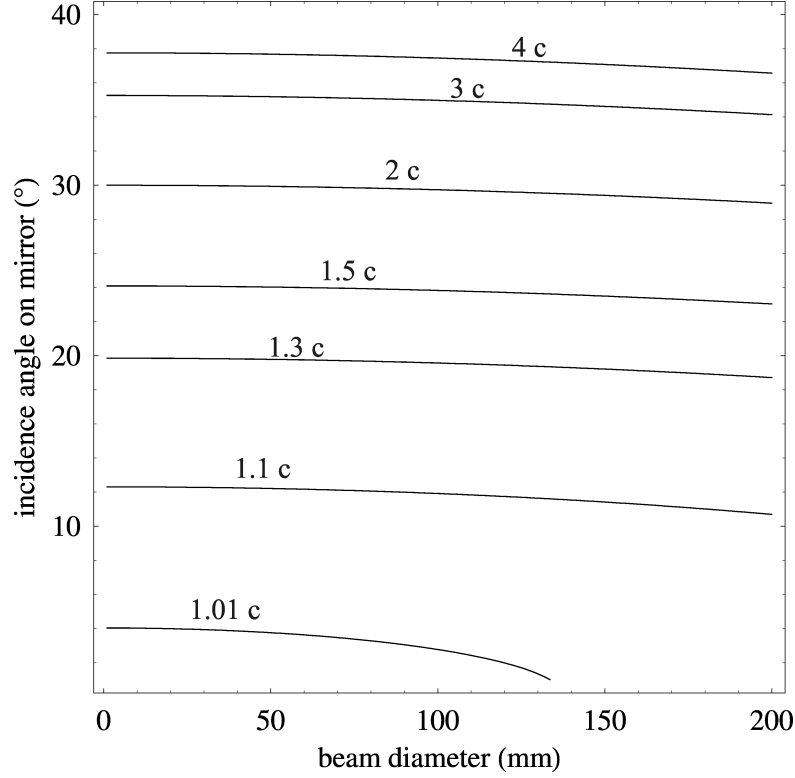


Figure 3.7: Average traveling wave velocity along the line focus represented as iso-contours for various beam diameters and incidence angles

mirror denoted i_0 one can write

$$\overline{NM}_2 = \overline{NM}_1 \tan i_0 = d \tan i_0 \quad (3.10)$$

so the final formula for the average TW speed is obtained using 3.8-3.10 as

$$TW = \frac{1}{\frac{d \tan i_0}{f} \cdot \frac{\sqrt{1 - (\sin i_0 - \frac{d}{4f})^2} \sqrt{1 - (\sin i_0 + \frac{d}{4f})^2}}{\sqrt{1 - (\sin i_0 - \frac{d}{4f})^2} - \sqrt{1 - (\sin i_0 + \frac{d}{4f})^2}} - 1} \cdot c \quad (3.11)$$

The average TW is plotted in 3.7 for a spherical mirror with focal length of 600 mm.

Note that for small (infinitesimal) beam diameters d , the above formula gives the instantaneous (local) TW speed, corresponding to the incidence angle on mirror i_0 :

$$\lim_{d \rightarrow 0} TW = \frac{1}{\cos 2i_0}. \quad (3.12)$$

The focusing mirror for generating the line focus of the main pulse introduces also an amplitude front tilt.

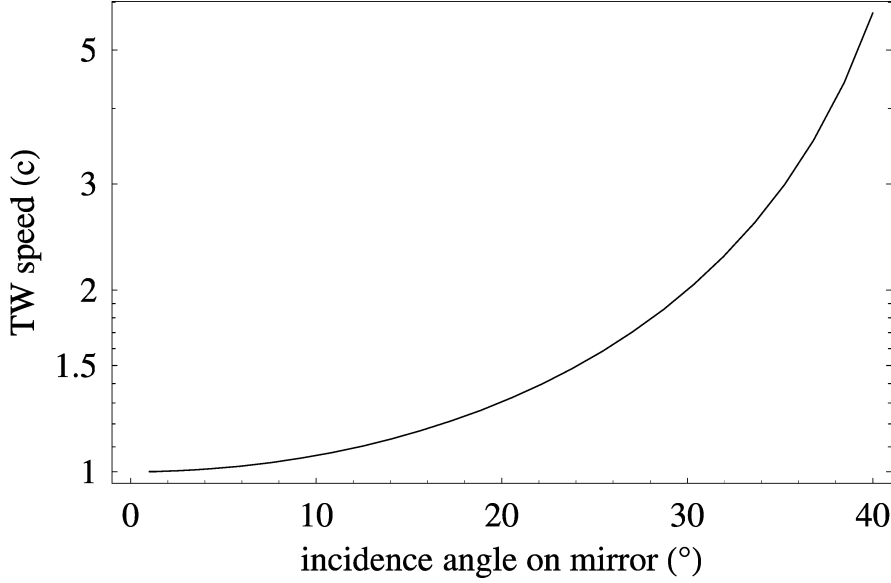


Figure 3.8: Local traveling wave excitation velocity in speed of light units as a function of the local incidence angle on a spherical mirror

The analysis of line focus and TW for XRL experiments has been performed up to now in other works using ray tracing codes. In contrast, the approach presented here is less time consuming, giving directly the analytical relations for line focus lengths and TW generated with a spherical mirror.

The TW effects of compressor and the focusing system can add constructively or destructively. In general it can be shown that the total TW is obtained by the formula:

$$TW_{tot} = \frac{TW_{GRIP}}{1 \pm \frac{D \tan \alpha}{F_1 F_2} \frac{TW_{GRIP}}{c}} \quad (3.13)$$

In the set-up used for the experiments reported here, one can introduce an angular chirp using the 10 J compressor by tilting one of the mirrors of the horizontal roof mirror. In this way one changes with a small angle ϵ_{RM} the 90° angle of the roof mirror and, as consequence, one obtains a tilt in the virtual gratings of the second pass on the compressor equal to $\epsilon_C = 2\epsilon_{RM}$.

The value of the ϵ_{RM} is limited by the width of the grating used. Using ray tracing the maximum angle of the roof mirror tilt was evaluated to 6 mrad. As a consequence, the maximum angular chirp that can be generated is 86 mrad.

The TW of the compressor was measured using an inverted field autocorrelator [PKW00]. In the setup, the delay between the two pulses is precisely

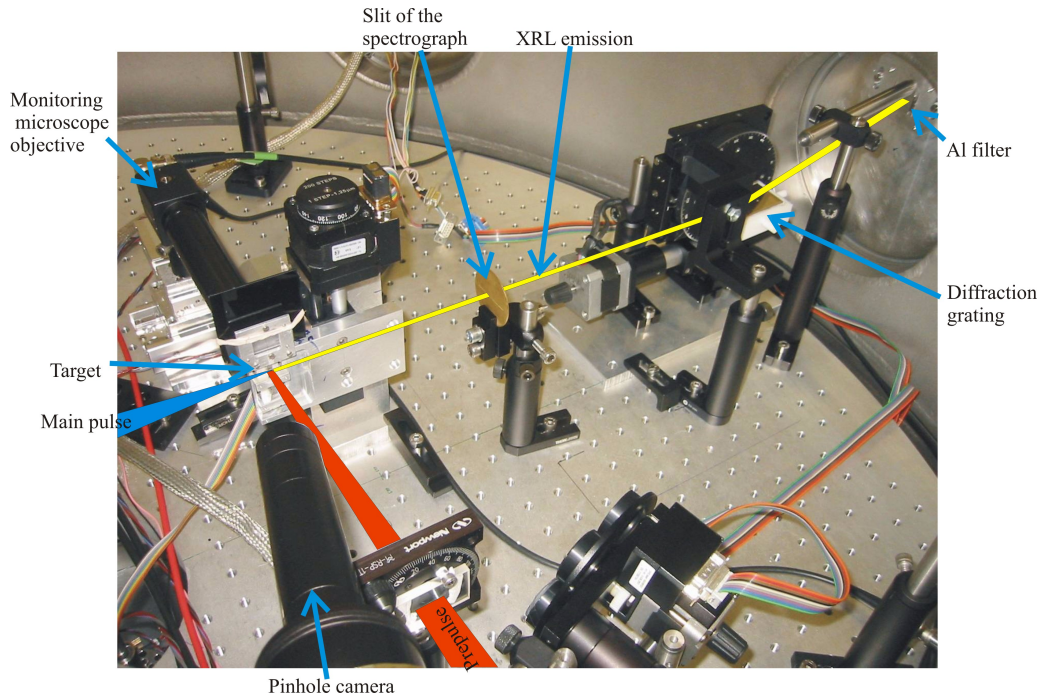


Figure 3.9: Detail photo with the spectrograph

controlled with a micrometer screw. The resolution for the measurement of the angle obtained with 350 fs pulses is about 1 mrad. This value is equivalent with 0.01 c TW. In this way, the compressor angular chirp was set to 0. As a consequence, the total traveling wave is determined only by the focusing mirror.

3.2.2 XRL diagnostics

In order to characterize the performance of the XRL, the spectral distribution of the emission from the plasma has to be measured. A clean signature for lasing is a strong enhancement of the laser line in comparison to the surrounding background features.

The flat field spectrograph implemented in the experimental set-up (see fig. 3.9) is based on a XUV flat-field grating (Hitachi type 001-0437), combined with a XUV CCD camera (Princeton Instruments). The grating substrate dimensions are 30 mm \times 50 mm with a curvature radius of 5649 mm. The average number of lines is 1200 /mm but the number varies along the grating from 1010 /mm to 1450 /mm. This special design [KHNK83] allows to obtain a spectral focusing in a plane perpendicular to the grating in contrast to the standard homogeneous line density gratings where the spectrum

is focused on the Rowland circle.

Due to the special design of the grating, the incidence angle on the grating is fixed to 87° as well as the distance from the entrance slit to the center of the grating and from the center of grating to the focal plane are fixed to 237 mm and 235 mm, respectively. The XRL emission is entering through a rectangular horizontal slit into the spectrograph, which allows to obtain a spatially resolved spectrum. The slit dimensions were $3 \text{ mm} \times 0.1 \text{ mm}$ and $10 \text{ mm} \times 0.15 \text{ mm}$, respectively, in the first (45°) and second experiment (GRIP). Due to the plasma gradients, the XRL beam is refracted several mrad from the plasma axis. The slit, the grating and the camera are placed along the propagation of the XRL pulse, to compensate this effect.

The CCD camera used as detector has a back illuminated detection chip exhibiting a high quantum detection efficiency in the XUV wavelength range. The visible light on the chip was suppressed by an aluminium filter with a thickness of 1.1 micron. The transmission curve of this filter is presented in fig. 3.10. For the lasing line of Zr at 22.02 nm the transmission is 18% and at 26.4 nm (the second lasing line) this is 9.5%.

The quadratic CCD chip has a width of 12 mm and 1024 pixels. As a consequence, the angular acceptance of the spectrograph is 20 mrad. The average spectral range which can be registered at one camera position is 6.5 nm, so using a specially designed adapter flange the 6.5 nm to 26.8 nm wavelength region could be covered. In the region where the two lasing lines are present (22-27 nm), the first order diffraction efficiency is approximately constant (9%-12% according to [EHM+84]).

The resolution of the spectrograph equals the number of illuminated lines multiplied with the diffraction order. For the given set-up this is in the range of 10^{-4} . However, due to the dimension of the pixel on the CCD the real resolution obtained is in the range of $2 \cdot 10^{-3}$ corresponding to less than 0.01 nm/pixel.

The properties of the plasma column were further analyzed using an x-ray pinhole camera. This is producing an image of the plasma through a hole of 30 micron diameter. A specially designed filter against infrared and visible light (1 micron polypropylene and 200 nm Al see fig. 3.10) defines the sensitivity range. The magnification of the system is 3.2. The 16 bit camera (Princeton Instruments) used for this purposes, similar to the one for the spectrometer, has a back illuminated cooled square chip of length 26 mm with 1024 pixels. This allowed to obtain the spatially resolved keV emission image of the whole 4 mm long plasma.

Alternatively in the 2003 experiments (45° incidence angle on target) a cross-slit camera was used. Here the pinhole is replaced with a set of slits at different positions relative to the CCD such that the magnification of

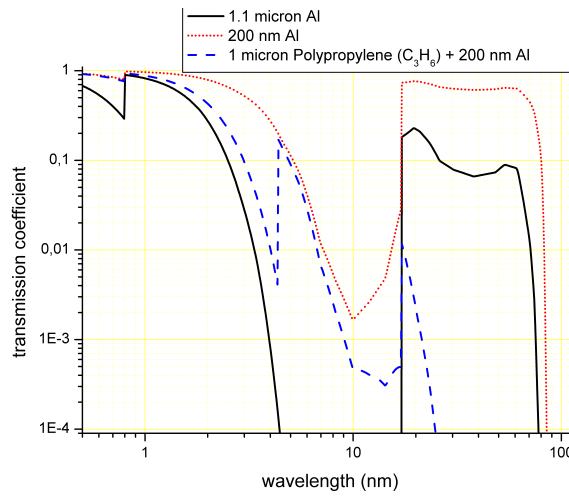


Figure 3.10: Transmission curves for the various filters used during experiments

the image in the two directions on the chip is different. Shots where the prepulse and the main pulse did not overlap were easily detected by the pinhole camera. It provided a full length side view of the plasma with a transverse resolution of the images of $10 \mu m$. In this case an 8 bit camera (PULNIX, model TM-745) with a 200 nm thick aluminium filter (see fig. 3.10) was used. The glass protection window of the camera chip was removed, in order to make it sensitive to keV radiation. However, dynamic range and quantum efficiency were significantly lower than with the back-illuminated detector.

In the GRIP experiments a third camera was installed, monitoring the target in the infrared and visible range. Using adequate motorized filters on a wheel the visible plasma emission during the shots was monitored. In this way the overlap of the two infrared pulses along the whole length of the plasma is controlled on-line.

Chapter 4

Experiments results

In the first round of experiments at GSI in 2003 employing 45° incidence angle the total energy from preamplifier was 5 J. 67% of the energy was delivered to the 10 J compressor, 33% was split off for the 0.8 ns prepulses. After compression the main pulse had approximately 2.4 J. The length of the line focus was 12 mm for both pulses. The peak-to-peak delay between the pulses was fixed to 0.7 ns. The incidence angle of the main pulse of 45° on target corresponds to a main pulse laser turning point density of $5.5 \cdot 10^{20} / \text{cm}^3$.

The CCD image from the spectrograph for one selected lasing shot is represented in three dimensions in fig. 4.1 for a 3.6 mm target length. The spectrum was limited on the left side by the length of the slit of the spectrograph as it is visible in the figure. The lasing line is 50 times stronger than the plasma emission background. The dip in the spectral line is due to a fiducial wire used to calibrate the deflection angle of the XRL beam.

The cross slit camera registered the keV plasma emission; a typical image after brightness and contrast enhancement is presented in 4.2.

The spectrum of the plasma in the absence of lasing presents no line at 22.02 nm and at 26.46 nm while at optimum parameters a highly reproducible spectrum is obtained as depicted in fig. 4.3.

The main pulse duration was varied from 0.5 ps to 6.4 ps. With a height of the focus line of $90 \mu\text{m}$ for the prepulse and $50 \mu\text{m}$ for the main pulse, the focused intensity was $1.2 \cdot 10^{11} \text{ W/cm}^2$ and $0.625\text{-}7.75 \cdot 10^{14} \text{ W/cm}^2$ respectively. The optimum main pulse duration was identified to be around 3 ps using a 5.75 mm target. For this duration the output of the XRL was three times higher than for a 0.5 ps pulse. Using the same parameters the gain curve was measured at a main pulse intensity of $1.66 \cdot 10^{14} \text{ W/cm}^2$.

A similar optimization strategy was applied during the experiments in June 2005 where for the first time a GRIP Ni-like Zr XRL was demonstrated.

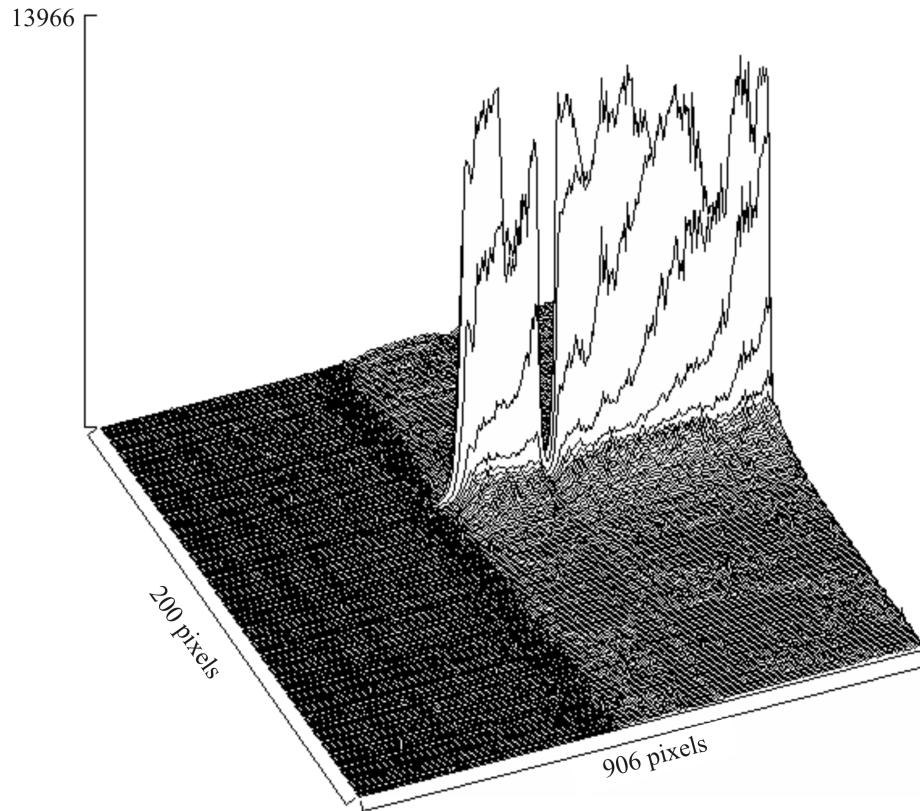


Figure 4.1: Spectrum of shot 47 (45°) for 3.6 mm target length, represented in 3D

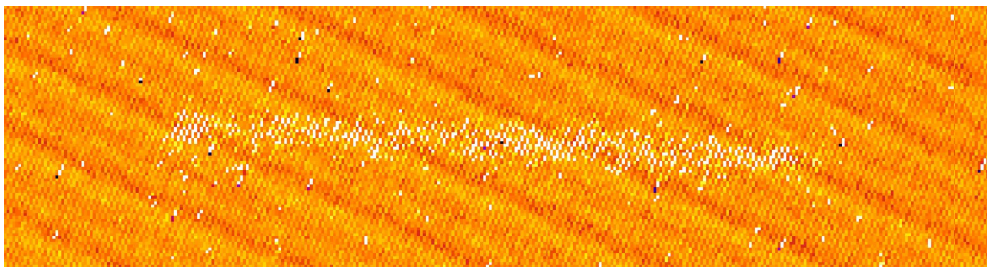


Figure 4.2: Measurement of the spatial resolved keV emission of the plasma for typical shot (45°)

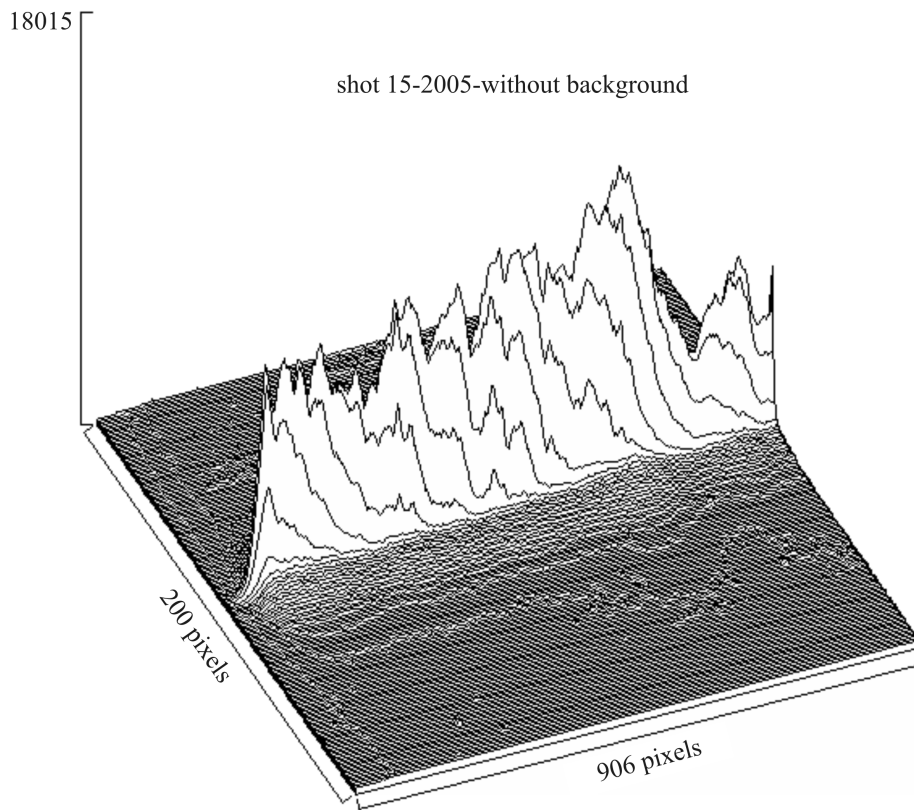


Figure 4.3: Spectrum of shot 15 (72°) represented in 3D

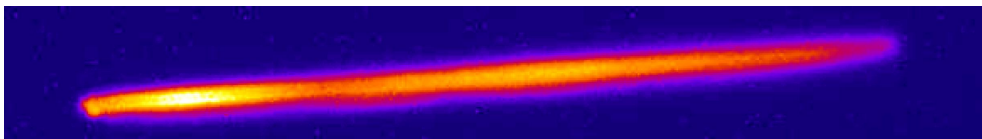


Figure 4.4: Measurement of the keV emission of the plasma for the GRIP set-up

The incidence angle on the target was 72° corresponding to a main pulse laser turning point electron density of $10^{20} /\text{cm}^3$. During this experiment the output energy of the preamplifier was limited to a maximum of 3.7 J. The line focus generated for the prepulse had 6 mm length and $80 \mu\text{m}$ width and the pulse duration was 800 ps corresponding to an intensity of $2.35 \cdot 10^{11} \text{ W/cm}^2$ for the 0.9 J pulses. The line focus for the main pulse was 5 mm long and $35 \mu\text{m}$ width with a total energy of 1.4 J on target corresponding to $1.6 \cdot 10^{15} \text{ W/cm}^2$ at 0.5 ps pulse duration. Optimization of the peak-to-peak delay gave a value of 200 ps. The main pulse duration was varied from 0.5 ps up to 5.5 ps, and the optimum pulse duration was identified to be the shortest one. A gain curve measurement was made using triangular targets generating plasma with length between 0.6 mm and 3.8 mm. An extended discussion of the results follows in the subsections.

Typical spectrum and X-ray plasma emission pictures are presented in figures 4.3 and 4.4 for comparison with fig. 4.1 and 4.2.

4.1 Lasing lines

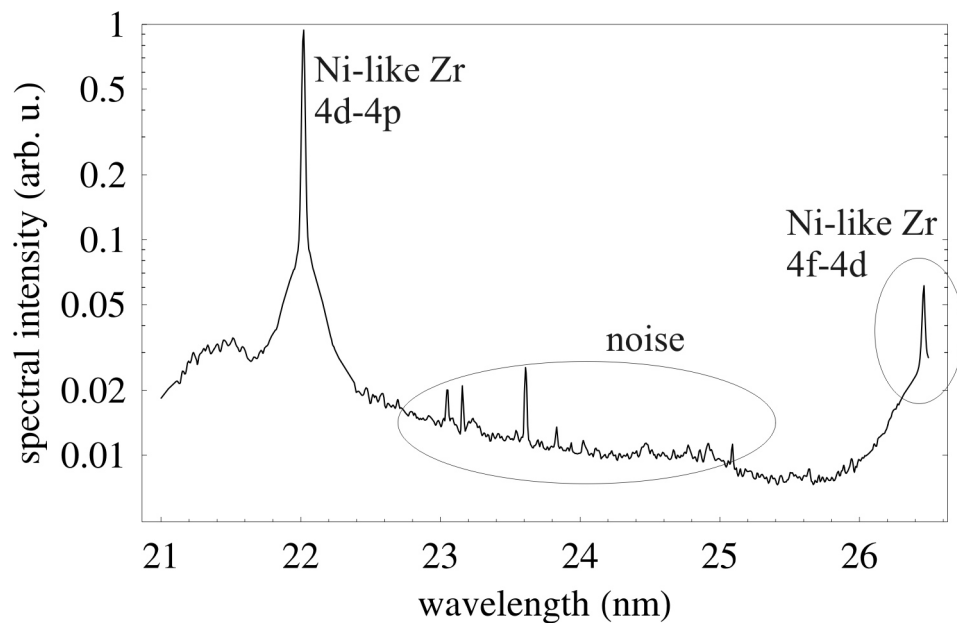


Figure 4.5: Logarithmic representation of measured lasing lines corrected for transmission filter of the spectrograph.

The two lasing lines of Ni-like Zr were observed. A typical spectrum is represented in logarithmic scale in fig. 4.5. For this plot the background of

the cooled CCD camera is first subtracted and in a second step is corrected for the transmission of the $1\ \mu\text{m}$ Al filter (see fig. 3.10). The strongest laser transition is the 4d-4p transition at 22.02 nm, the second a 4f-4d transition, both in Ni-like Zr. The second lasing line is attributed to collisional excitation combined with self-photopumping [Nil97, DNO⁺99]. The noise in the graph is coming from some bright dots registered by the camera, which can be associated with keV radiation hitting the CCD chip.

4.2 Delay between the pumping pulses

The output of the XRL as a function of the delay between the pulses is represented in fig. 4.6. The presence of the lasing line for large delay changes is a sign that the GRIP XRL is driven with enough prepulse intensity to make it insensitive to energy fluctuations of the prepulse.

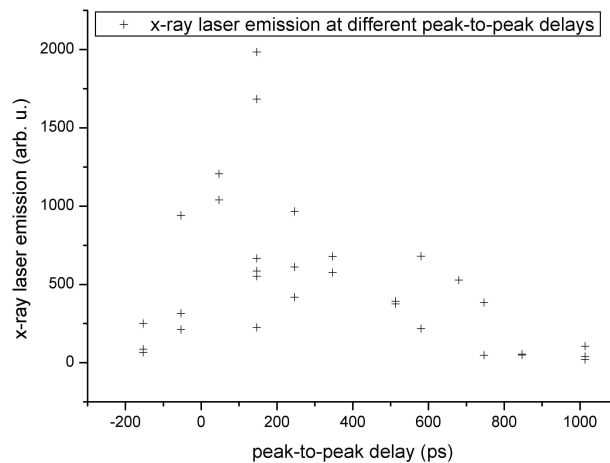


Figure 4.6: Output of the GRIP Zr XRL as a function of the peak-to-peak delay of the prepulse and main pulse

The scattering of the GRIP XRL intensity values can be attributed to a simple incident which shows the importance of carefully driving the laser pulses. In the experiments, the overlap of the two focus lines of the XRL was fluctuating between the measurements due to thermal lensing induced by the water cooling systems of the three glass amplifier heads. These oscillations are represented in fig. 4.6. The temperatures of the amplifier heads were oscillating with periods close to 3 minutes, independently for the two 19 mm

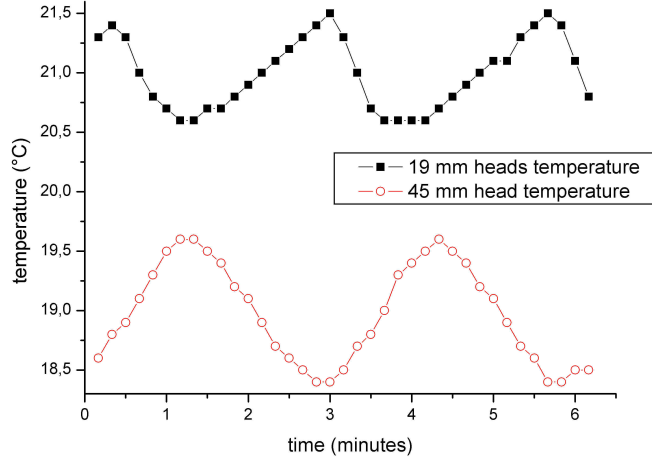


Figure 4.7: Measured thermal oscillations of the preamplifier laser heads as a function of time, due to the cooling system feedback loop

heads and for the 45 mm head. The amplitude of the oscillations was about 1 K. During the cooling phase a thermal lens builds up via a competition of glass expansion of the rods and change of the refraction index induced by temperature. This dynamic thermal lensing effect translated into a variation of the focal length and into a small displacement of the two focusing lines on target of the order of 15 micron, due to the long propagation in compressor and in optical delay line. After identifying the problem the temperature of the cooling water was changed at the infrastructure level and also the feedback loop of the water cooling device was set very carefully to get rid of these fluctuations.

The total peak-to-peak delay which can be inserted in the system ranges from -150 ps to 1000 ps showing that even with a prepulse fraction as low as 250 ps (out of the total 800 ps duration) conditions are created to generate lasing via main pulse. This information has to be related to the ionization dynamics of target.

In fig. 4.8 the ionization potentials for Zr are depicted. To obtain Ni-like Zr from previous ionization charge state one needs about 248 eV and to further ionize it more than 402 eV. This significant energy difference is one of the key factors in the Ni-like XRL schemes allowing to obtain large percentage of plasma ions in the Ni-like state. On the other side, one can use plasma physics scaling laws to predict the average charge state at a given plasma temperature. The rule of thumb says that a third of the plasma temperature

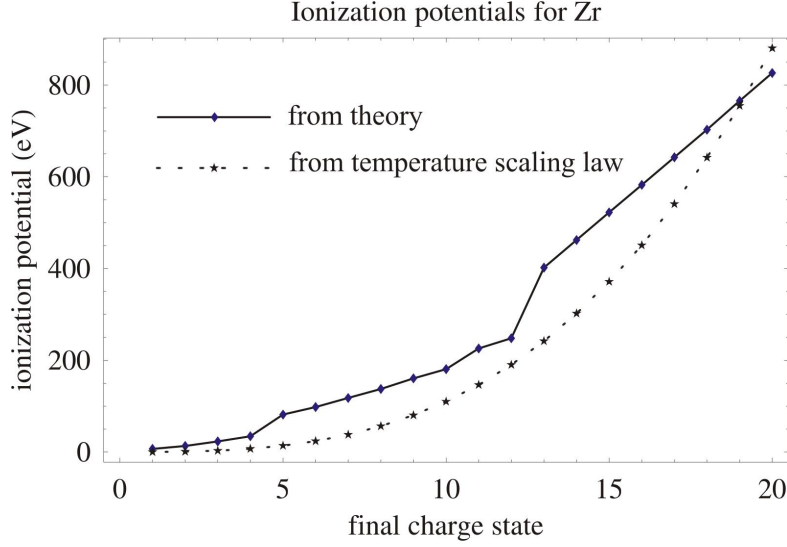


Figure 4.8: Ionization potentials for Zr obtained from atomic physics theory compared to ionization potentials for Zr obtained from plasma temperature scaling laws

in eV represents the value of ionization potential for the average charge state. Inverting the formula for the average charge state (see eq. 2.6) one obtains:

$$U_{pot} = 3 \cdot T = 3 \cdot \frac{1}{A} \cdot \left(\frac{3}{2}Z\right)^3 \quad (4.1)$$

This function is represented in fig. 4.8 to elucidate the value of approximation used in the preplasma description. In other words, one can formally associate an ionization potential of one ion species with a given plasma electron temperature. Comparison of the calculated ionization charge state to the real one is presented in fig. 4.8. It indicates that the eq. 2.6 might overestimate the value of the average charge state by two or three charge states.

As experimental results show through the presence of the lasing line, a Ni-like Zr plasma is reached for a wide range of prepulse and main pulse intensities and delays. Due to the focal line width variation generated by the thermal lens problem one has to assume 50% intensity variation of the prepulse which translates in only 27% temperature fluctuation according to the formula 2.25. Change of the temperature of the preplasma at the arrival of the main pulse at different delays in these experiments is estimated according to the same formula to be 36%. Changes in the intensity of the main pulse are more drastic, a factor of three between minimum and maximum intensity,

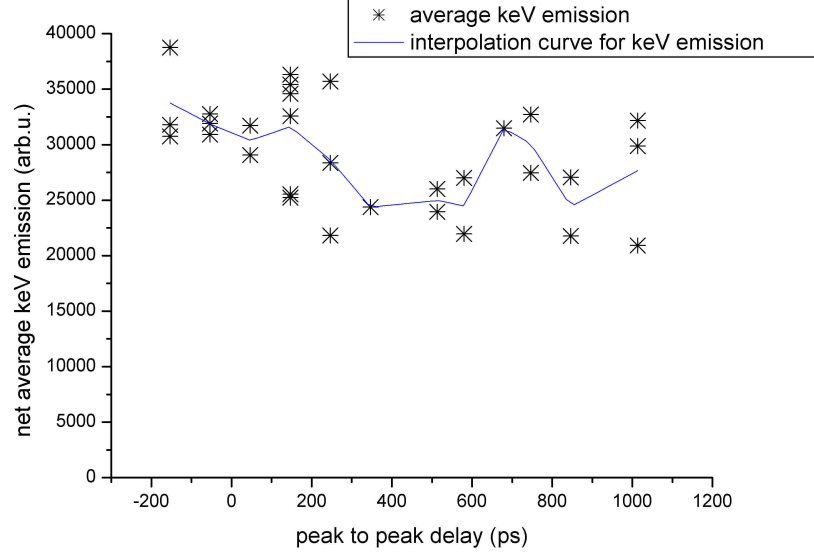


Figure 4.9: The keV emission of the plasma measured with the pinhole camera for various peak-to-peak delays, at 72° angle (GRIP)

estimated from line focus measurements in the presence of the thermal lens. According to the model in [LZ01, LLZ02], the temperature of the plasma grows approximately linear with the energy of the main pulse and does not depend on the intensity. If one includes the IB correction factor and the plasma opacity, the model can be significantly improved as presented in the following subsection.

Analysis of the keV emission shows a scattering of the plasma temperature of a factor of 2. This is shown in fig. 4.9 where the background corrected keV emission of the plasma was registered with the pinhole camera through an Al-polypropylene filter with low energy photons cut off at 500 eV (see fig. 3.10). These fluctuations are mainly due to the dynamic thermal lens problem.

An important quality of the XRL output is the divergence of the emission. The divergence of the shots with -150 ps and 1000 ps delay in the plane perpendicular to the target is measured from the spectrograph image. While the angular acceptance of the spectrograph is about 15 mrad, the line focus is having almost constant intensity over the whole line. This suggests a beam divergence in the plane perpendicular to the target in excess of 15 mrad. Taking in account a 3 mm long active medium this corresponds to more than 50 μm gain region in the plasma. Using the simplified analytical formulas

presented in the plasma modeling chapter (eq. 2.25) this corresponds to two scale lengths of the preplasma. Translated in electron densities this is equivalent with a factor of 4 from one side to the other of the gain region, measured in the plane perpendicular on the target.

4.3 Optimal duration of the main pump pulse

In a second optimization step, the duration of the main pulse was tuned from 0.5 ps to about 6 ps. The puzzling result from the experiment using 45° incidence angle was that the temperature of the plasma is smaller when short pulse durations were used, in spite of the fact that the total pulse energy was constant, and at first sight one would expect constant time-integrated plasma temperature. A qualitative explanation was proposed in [NSC⁺04] considering the effect of the IB correction factor at high laser main pulse intensities, corresponding to short pulse durations. The influence of this factor on the absorption at different intensities is described in section 2.2 of this thesis.

The results from the experiments using 72° main pulse incidence on preplasma show much less influence of the main pulse duration on the keV plasma emission. The temperature of the plasma is slowly increasing when the main pulse duration increases as indicated in the measurements performed with the pinhole camera. For comparison, the results of the two experiments are presented in fig. 4.10.

As the calculations developed in this thesis show, the IB correction factor is only half of the truth. The absorption of the main pulse in plasma is given by the opacity of the plasma created by the main pulse. This is dependent not only on the IB correction factor but also on the optical path of the main pulse within the plasma. As it appears from the analysis developed in section 2.3, this path is controlled via the incidence angle of the main pulse on the preplasma, being an intrinsic feature of the GRIP scheme. However, it should be noted that the optical path is also depending on the plasma scale length, making necessary the use of MHD analysis coupled with the ray tracing code and the absorption in plasma analysis using the IB correction factor as it will be shown in next subsection.

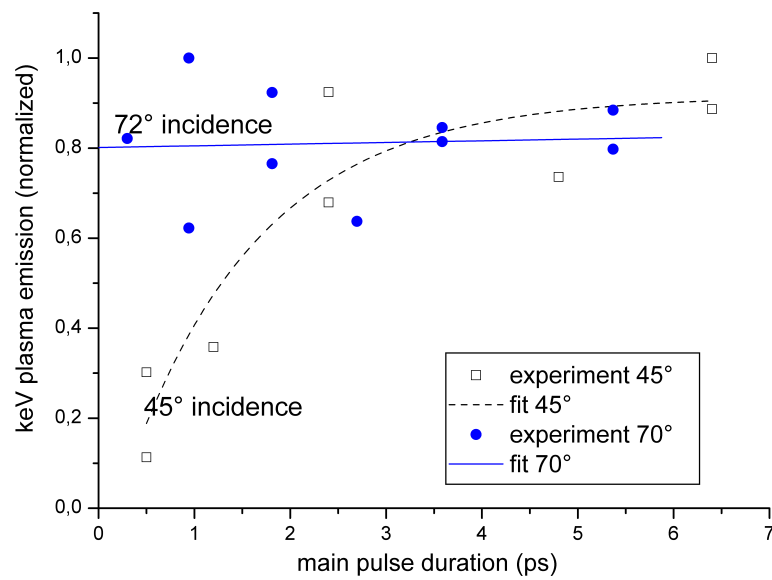


Figure 4.10: Comparison of the plasma x-ray emission intensity as function of main pulse duration for 45° and 72° incidence angles on target

4.4 Main pulse absorption: theory vs. experiment

In this section numerical results of the absorption are presented in order to evaluate the absorption of the main pulse in the plasma. The previous analytical calculations for the main pulse final temperature [LZ01, LLZ02] have the drawback that they do not take into account the reduced IB absorption. Neither are they concerned with the opacity of the plasma, assuming that all the main pulse energy is absorbed. Their approximations concerning the plasma opacity are still very useful in the case of normal incidence on target when all the rays reaching critical density regions are absorbed. Their model predicts an almost linear increase of the temperature with the main pulse energy and an increase of the scale length of the plasma which scales roughly as square root of the deposited energy. This is a consequence of the implicit assumption that all the pulse energy is converted into thermal energy of the electrons. No dependence of the absorption with the main pulse duration can be predicted in the frame of this model approximation.

In this work these scaling laws are significantly improved. The correction to the model is introduced through the IB correction factor and through the opacity calculation using the complex refraction index as described in section 2.3.

To perform calculations, in the first step the dependence of the transmission of the main pulse through the plasma on temperature is derived directly using the scaling laws of the main pulse temperature and of the plasma scale length mentioned in the above paragraph. The result is plotted in fig. 4.11 for the case of both experiments at 45° and 72° incidence angle.

The inverse Bremsstrahlung (IB) absorption correction factor is determined as described in section 2.2. As mentioned there, this correction factor can be influenced by the non-maxwellian electron velocity distribution [Lan80], which is included in the calculation of the above plots. The electron-electron collision rate is in the order of 10 ps, that means longer than the main pulse. As a consequence it can be considered in the first order approximation for the IB correction factor calculation that the temperature associated with the electron distribution function is unchanged during the main pulse interaction with plasma.

In a second step, the following equation is solved:

$$\frac{\partial T(t)}{\partial t} = \gamma(1 - \Xi(T(t))) \quad (4.2)$$

where the $T(t)$ is the temperature of the plasma at the moment of time t which takes values between 0 and the duration of the main pulse; Ξ denotes

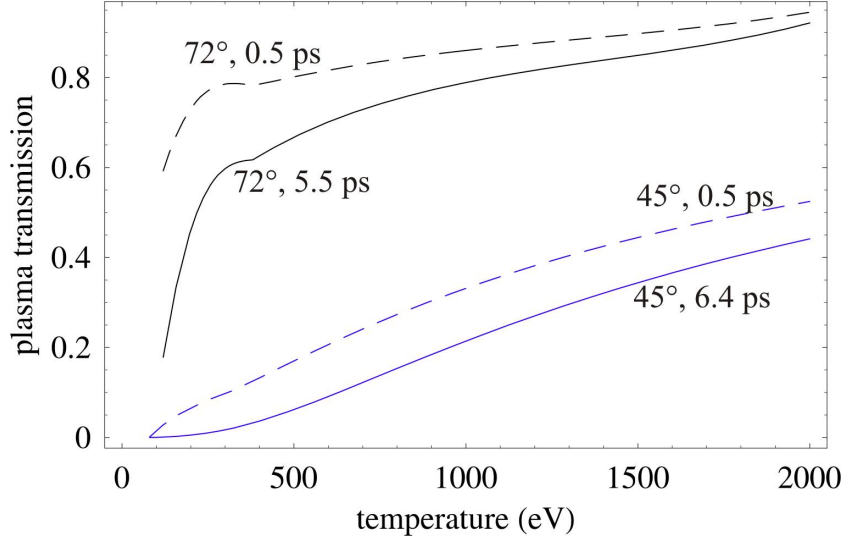


Figure 4.11: Calculated transmission of a 0.5 ps and a 6.5 ps main pulse through plasma in the experimental conditions from 2003 in blue (45°) together with a 0.5 ps and a 5.5 ps main pulse in the experimental conditions from 2005 in black (72°).

the transmission of the plasma as a function of temperature as shown in fig. 4.11. The coefficient γ is obtained from the analytical formula of the model in [LZ01, LLZ02] assuming full absorption of the pulse as follows:

$$\gamma = \frac{T_{Main} - T_{Free}}{t_{Main}} \quad (4.3)$$

where T_{Free} and T_{Main} stand for plasma temperature after free expansion period and after main pulse while the t_{Main} parameter represents the duration of the main pulse.

The above differential equation implies that the increase in the temperature is proportional to the absorbed energy $1 - \Xi$. In the case of opacity equal to unity, the linear dependence of [LZ01, LLZ02] is recovered due to our choice of the γ coefficient.

Interpolation of the points in fig. 4.11 was used for the calculations, allowing to obtain the solution of the above differential equation for the $T(t)$ as a numerical function. The results for a 5.5 ps main pulse in 72° configuration are presented in figure 4.12, in comparison with the result from the analytical model from [LZ01, LLZ02]. The plasma temperature during the main pulse reaches 1750 eV temperature at the end of the main pulse, in contrast to the 3000 eV predicted by the linear model with plasma opacity equal to unity.

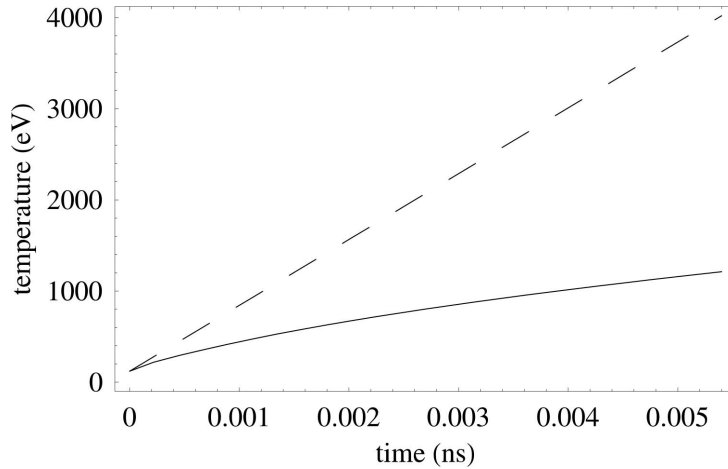


Figure 4.12: Temperature evolution of the plasma in time according to [LZ01] model (dotted line) and according to the model presented in this work which includes the IB correction factor and opacity of the plasma for the 5.5 ps pulse in 72° configuration.

Further, computation of the temperature at various main pulse durations was performed in order to compare it with the signal of the cross slit camera. The longer the pulse, the higher the temperature, so that for the longest pulse of 6.4 ps the temperature reached is 2250 eV, while according to the linear model the pulse duration has almost no influence on the predicted temperature which equals 3000 eV.

For the experiments using 45° incidence angle, the theoretical signal obtained on a camera with constant quantum efficiency through an Al filter (low frequency cut off 850 eV) is represented together with the experimental results. The correction factor is computed taking into account constant preplasma temperature (85 eV). It seems that the computed curve is not decreasing so drastically at short main pulse duration as the experiment. This discrepancy has to be understood as reduction of the quantum efficiency of the CCD which registered the plasma keV emission corresponding to lower energy photons. Taking this into account, the agreement of the computations with the experiment is recovered.

The XRL emission for 45° and 72° incidence angle on target for various main pulse durations is presented in fig. 4.14. For the 45° incidence angle a maximum emission intensity is identified at about 3 ps main pulse duration. The result is compatible with previous observations for Pd for example see ref. [DON⁺00] where an optimal pulse duration of 6 ps was measured with the main pulse having normal incidence on target.

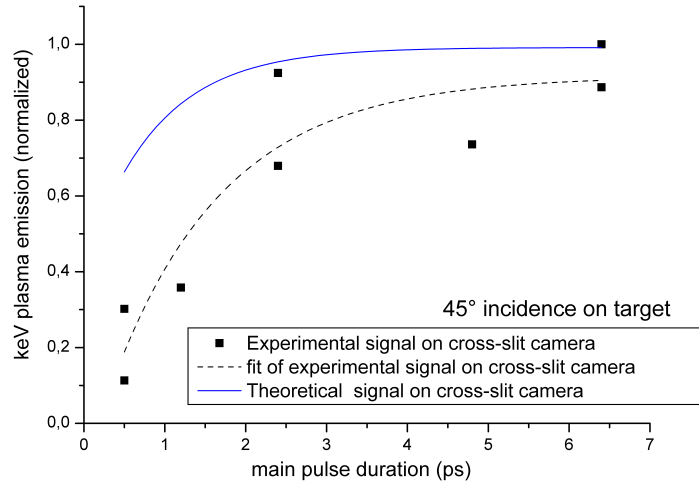


Figure 4.13: Comparison of the cross-slit camera measurement with theory for the 45° incidence angle

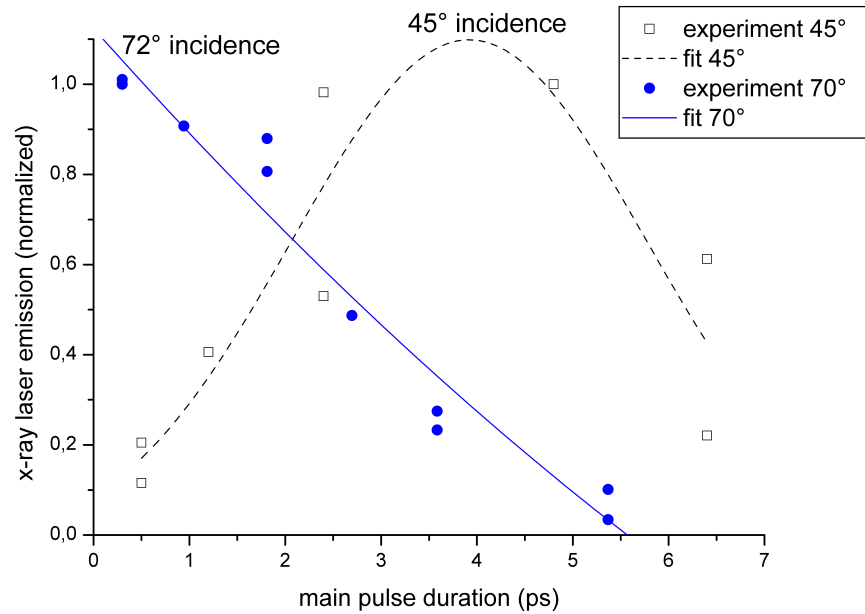


Figure 4.14: Comparison of the x-ray laser emission as a function of main pulse duration for 45° and 72° incidence angles on target

For the GRIP set-up at GSI the highest XRL output is obtained at the best optical compression of the main pulse, corresponding to 0.5 ps. This behavior is unexpected, because it cannot be extrapolated from previous TCE experiments with normal incidence on target of the main pulse. The experiments for individual geometries were performed at the same pump energy and it has been seen from the integrated keV emission that at such short pulses the main pulse energy absorption in plasma tends to be reduced due to IB correction factor.

It can be concluded from here that large reduction can be clearly observed for short pulses, if the energy deposition is mainly in the high density regime of the plasma. In contrast to that in the GRIP schemes, where the main pulse energy deposition happens at lower densities, the absorption reduction is no more so strong, and the intensity increase of the main pulse has a beneficial effect. However, a direct comparison of the effect of different incidence angles on target with the available data is not completely clear, because the initial average charge state of the plasma is not the same

4.5 Small gain coefficient of the XRL

In both geometries, two lasing lines were identified from the emission spectrum of the Ni-like Zr XRL. The stronger one at a wavelength of 22.02 nm is identified as the 4d-4p transition and the second one at 26.46 nm as the 4f-4d transition. In both cases, the ratio between the two intensities is about 10. For spectroscopy experiments on Li-like ions certainly the 22.02 nm lasing line is the better choice. However, the second line might also be important in various situations. For example, if the intensities of the two lasing lines would be equal, due to the beat of the two frequencies a picosecond long electromagnetic pulse train made of 440 atto-second pulses would be generated. This could be achieved using HHG at 26.4 nm wavelength and injection in Ni-like Zr XRL.

The gain for the GRIP Zr XRL at 22.02 nm was measured at the main pulse duration and peak-to-peak delay where the maximum output was reached. Triangular targets allowed to use plasma lengths from 0.6 mm to 3.8 mm. The results are presented in fig. 4.15. There were two shots at each position on the target. Interesting clue is provided by the fact that the XRL output intensity from the second shot in one place is systematically higher than the output of first shot in the same place. Fitting individually the first shot series and the second shot series for plasma lengths up to 2.7 mm using the Linford formula [LPSS74], one obtains a small gain coefficient of 11 /cm and 22 /cm respectively.

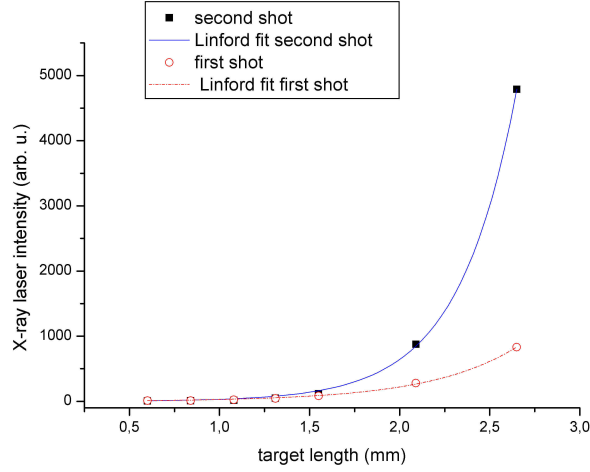


Figure 4.15: Zr XRL gain measurement depending on the target length using linear scale; the curves are corresponding to the first shot and to second shot in the same groove, respectively

The explanation for the different gain might come from the fact that the groove made by a first shot acts as a focusing mirror for the second shot. For a $3 \mu\text{m}$ deep groove made by a $80 \mu\text{m}$ pump pulse width one obtains a cylindrical lens with $400 \mu\text{m}$ focal length which means an accordingly higher energy density in the plasma for the second shot.

Another important parameter can be obtained from fig. 4.16 where all measurements of the GRIP XRL output as a function of target length are represented in a logarithmic scale. The signature of the saturation for the XRL is given by the roll off of the curve which appears for target lengths about 3 mm long.

This roll off might be produced by the XRL propagation in plasma, too. In this case the XRL will be refracted out from the gain region due to the plasma gradients after a distance shorter than the plasma length. This possibility has to be excluded due to the fact that our preplasma is produced with a relatively long prepulse (800 ps) generating soft plasma gradients and due to the fact that the density at the gain region is $10^{20} / \text{cm}^3$ where the refraction index varies slowly. Besides of that, the length of our plasma medium is below 4 mm. Another argument favoring the interpretation of the saturation roll off is the gain length product of the order 10 which is also considered to be a sign for saturation (see [Elt90]).

A third argument supporting the presence of saturation in the GRIP case is the comparison with the experiments performed using 45° main pulse in-

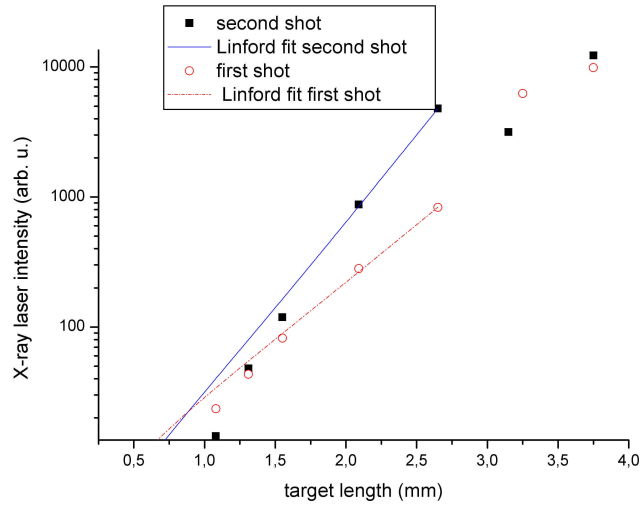


Figure 4.16: Zr XRL gain measurement depending on the target length using logarithmic scale; the curves are corresponding to the first shot and to second shot in the same groove, respectively

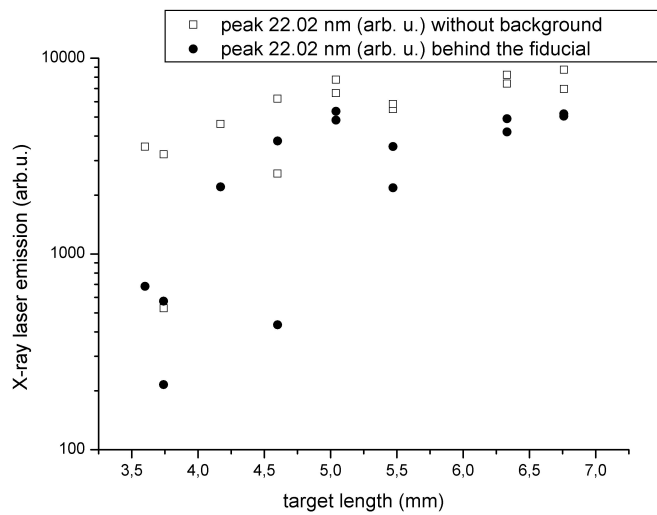


Figure 4.17: Gain curves for the experiment with 45° measured using averaged values of the spectral line and measurements of the line emission behind the fiducial wire

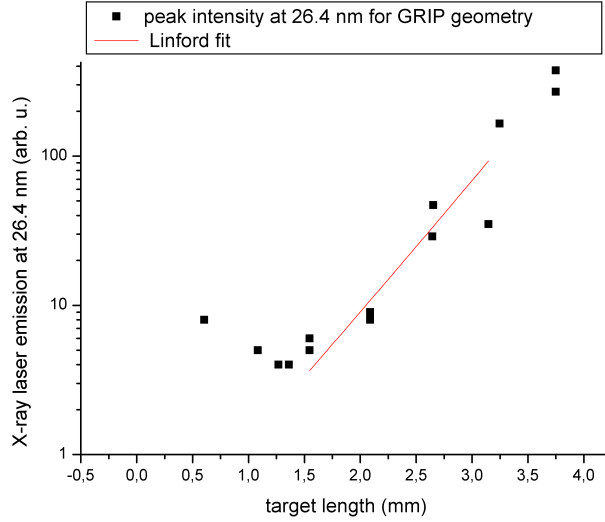


Figure 4.18: Gain measurements for the second lasing line and a Linford fit (72°)

idence on target. The 45° XRL output is represented on a logarithmic scale as a function of target length in fig. 4.17. In this case the CCD of the spectrograph was showing saturation of the pixels. Re-evaluation of the data has been performed in two ways: measuring the XRL line intensity behind the fiducial wire used as a spatial reference in the experiment and measuring a certain region from the spectrograph lasing line and then subtracting the background. These two measurements together with the initial data evaluation give essentially the same result: the roll off of the gain curve appears for target lengths about 5 mm long. The pumping conditions for the two pumping geometries are quite similar so one can infer that a roll off due to refraction in plasma might appear only after more than 5 mm propagation in both cases.

We analyze further the second lasing line (26.4 nm) attributed to 4f-4d transition in Ni-like Zr XRL. The result from the GRIP experiments in this case are presented in fig. 4.18 on a logarithmic scale together with the Linford fit. The measured gain is again 22 /cm for targets up to 3.7 mm length. The major difference is the lack of roll off, in comparison with the lasing line at 22.02 nm. This shows potential for an intensity increase of the 4f-4d line relative to the 4d-4f line for longer target lengths.

Turning now to experiments at 45° , the gain for the 26.4 nm lasing line is presented in fig. 4.19. In this case the evaluation of the intensity of the spectral line was again performed using the two methods described for

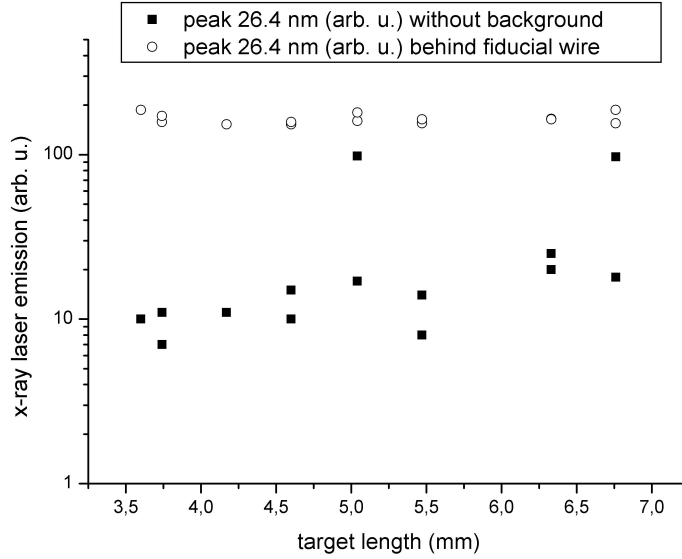


Figure 4.19: Gain measurements for the lasing line at 26.4 nm (45°) using two methods

the analysis of the 4d-4p lasing line at 45° . In this case the background subtraction technique shows a slow increase of the lasing line for all target lengths. The gain is evaluated to 4 /cm which is comparable with the one obtained at saturation for the other lasing line. As a consequence no increase in the second lasing line relative to the first line is expected for larger targets.

Another important difference between GRIP and 45° geometry is identified in this way. The significantly larger gain and the lack of roll off in the GRIP case for the second line shows potential for enhancement of this lasing line when needed.

4.6 Prepulse influence and gain region

The picture of the Ni-like Zr XRL is completed in this section by pointing out several features observed during experiments related to the gain region.

One basic test during the experiment at 45° main pulse incidence angle was to look for the lasing line employing only the prepulse or only the main pulse. In both cases no spectral line corresponding to the laser transition could be identified with the spectrograph. In the case of the main pulse shot only this shows that the pulse contrast of our pump laser is high enough to prevent the formation of a preplasma due to some energy pedestal. If,

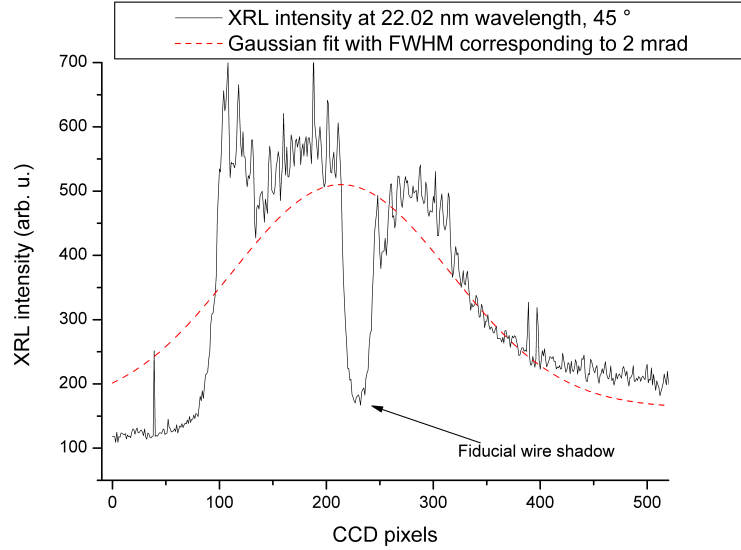


Figure 4.20: Spatial profile along the 22.02 nm lasing line registered by the spectrograph at 45° pumping geometry

however, the prepulse was maintained, although strongly reduced by a factor of 40 to about 25 mJ, at a main pulse energy was 1 J on target lasing was still observed. In this way an interesting result is obtained similar with those reported in [JLP⁺03] and analyzed theoretically in [JNKP04, JTPN05]. In these papers lasing is achieved in TCE Ni-like Ag XRL at 13.9 nm using only one pumping pulse with a long low-energy pedestal coming ahead the main pulse. Our low energy prepulse simulates the conditions from the above mentioned papers.

An important result concerning the XRL divergence was obtained for this situation, as presented in fig. 4.20. The low divergence of the laser pulse, of the order of 2 mrad for a 5.8 mm target shows a very narrow gain region in plasma. This has to be expected according to formula 2.27 which predicts a power law dependence for the plasma scale length as function of the temperature of the prepulse. Taking into account the scaling law of the temperature with the prepulse intensity (2.25), one obtains a factor of 10 reduction in temperature and only a factor of 2 reduction in the plasma scale length and in the average charge state for the preplasma.

4.7 Target behavior

All shots performed with 45° incidence angle geometry were using a several seconds train of prepulses in advance at a repetition rate of 10 Hz with an average energy of 10 mJ per pulse. They were cleaning and heating the target.

After up to twelve XRL shots using the same place of the target a groove in the target appears. Using Zr allowed to obtain lasing with every shot without observing significant reduction in the XRL output, contrary to the cases reported in the literature for silver. This is explained by the high melting temperature of the Zr (2128 K) which is almost double in comparison with Ag (1235 K). A picture of the damage on the target and measurement of the groove depth are presented in fig. 4.21. The upper picture shows the microscope image of the groove and the liquid Zr droplets spread on both sides of the groove; the lower picture shows the measured groove profile after 11 shots. The depth of the groove is about 60 microns, corresponding to an average 5 microns ablation substance per shot. Part of the material is melted and spread on the target making it improper to be used for other XRL shots in a region of about 150 microns on both sides of the target.

Using GRIP geometry the lasing efficiency of the Zr XRL was tested with and without prepulses. No difference has been observed in the output of the XRL.

A typical image of the target structure after two shots with parameters used for measuring the gain curve is presented in fig. 4.22. One can see the solidified Zr droplets spread at the sides of the groove. The edge of the target is much stronger affected by the shot while the incidence angle on the lateral side of the target is complementary to the GRIP angle so the main pulse pump absorption takes place closer to the target in a denser region and, as a consequence, is enhanced significantly. So the plasma temperature increases and the most ablated mass is produced after the main pulse arrival. However this does not influence the XRL output because lasing takes place almost at the same time or several picoseconds later, while the plasma density profile is defined by the prepulse.

4.8 X-ray emission dip

From the analysis of the pinhole camera pictures one can extract information about the energy deposition along plasma line in the GRIP geometry. This is relatively homogeneous along the plasma line.

When analyzing the x-ray emission transversal to the plasma line, a single

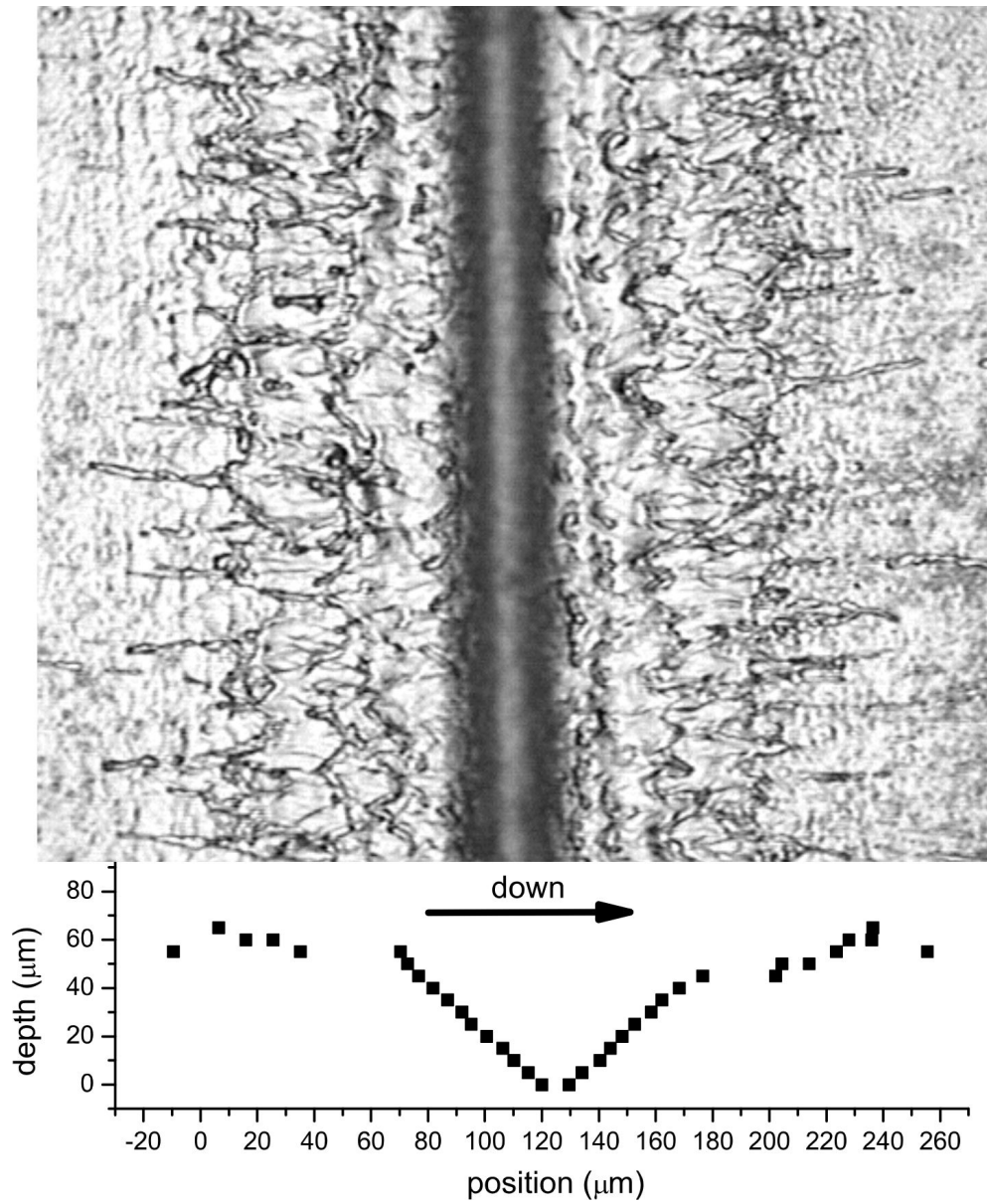


Figure 4.21: Groove in the target after several shots. Upper picture shows the microscope image of the groove and the Zr droplets spread on both sides of the target; lower picture shows the measured groove profile after 11 shots.

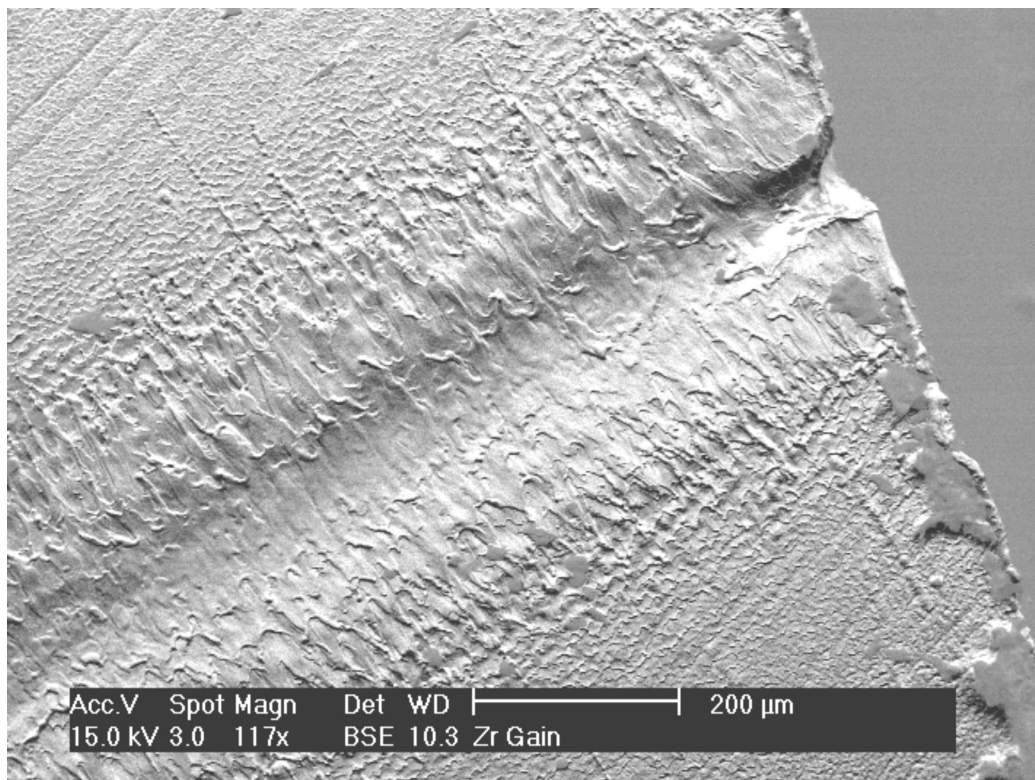


Figure 4.22: Scanning electron microscope image of the Zr target after two shots in GRIP configuration with 0.5 ps main pulse duration

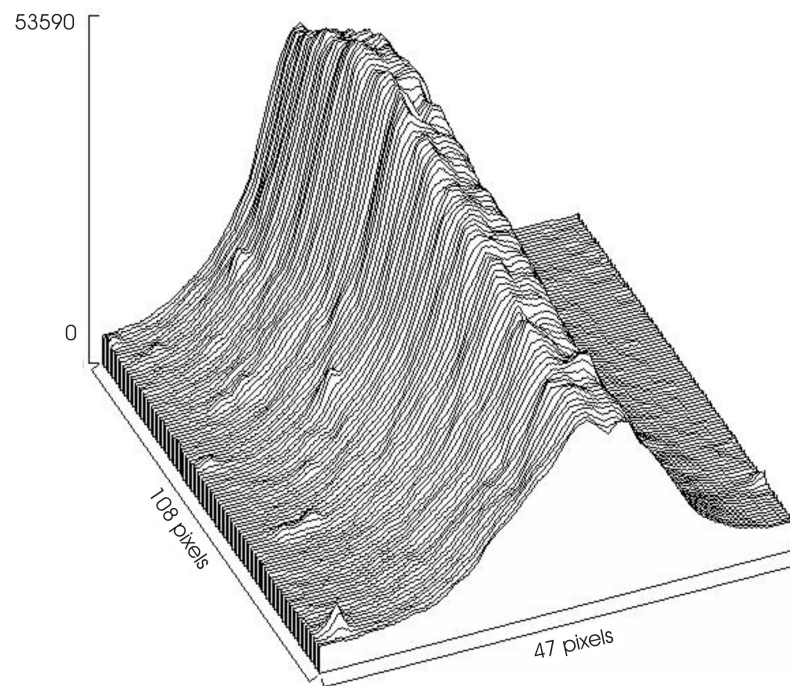


Figure 4.23: 3D representation of the spatially resolved keV plasma emission with the dip feature

peaked shape is expected if one would add up the contributions of the two pump pulses. However, the resolution of the pinhole camera (30 microns pinhole) allowed to distinguish a double peaked structure in the x-ray emission, as presented in fig. 4.23 for several shots. This is for the first time when such an observation is reported in the TCE XRL literature. The two peaks are separated by a distance of 4 pixel corresponding to 32 microns. The valley in the middle is relatively small, of the order of 10%. This excludes the possibility to be created independently by the prepulse and by the main pulse since the FWHM of the main pulse is 70 microns. As a consequence a few microns shift would be clearly peaked on the side of the main pulse.

The plasma produced by the prepulse alone has significantly lower temperature, evaluated from the analytical model to 120 eV in the GRIP typical conditions, while after the main pulse the plasma reaches temperatures of the order of 1 keV.

There are three processes which might account for the observed valley. In the first place one should trace this phenomena back to the prepulse. In [FRJ⁺03] the apparition of an inverted density profile with a density minimum on axis and distinct plasma side lobes was reported. They monitored the plasma generated by a laser pulse in an intensity range similar to our prepulse using soft-x-ray laser interferograms. Their model simulations show that this strong two-dimensional hydrodynamic behavior is essentially a universal phenomena that is the result of plasma radiation induced mass ablation and cooling in the areas surrounding the focal spot. The two density lobes could be then stronger heated by our main pulse generating in this way two regions with stronger keV emission. However, the experiments made use of 13 ns laser pulses and the models presented in the cited paper do not show enough spatial and temporal resolution to allow the evaluation of this effect for the parameters used in GRIP XRL experiments.

A second process is related to absorption mechanism. IB reduction at the center of the main pulse focal line is stronger than at the sides of the pulse. So one might expect a reduction of the absorption in the center of the focus line compared with the one without IB correction factor. This process alone cannot invert the energy deposition within the plasma profile but in the presence of the previous mentioned process this can enhance the temperature in the density side lobes.

A third possibility is generated by laser pulse light pressure coupled with the laser propagation at GRIP geometry. The density side lobes could be generated by the light pressure applied stronger to the center of the pre-plasma and less to the sides. Such effects at the level of 10^{14} - 10^{15} W/cm² were observed for example in [ASAL78]. In such early interferometry experiments of laser created plasmas at irradiation intensities of $3 \cdot 10^{14}$ W/cm² a

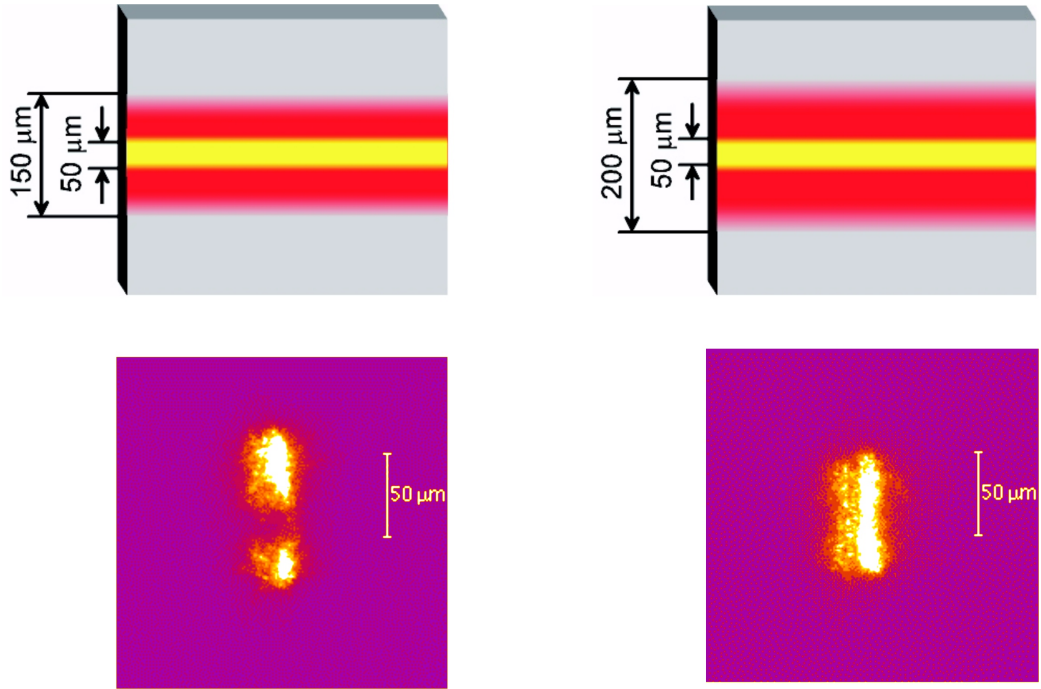


Figure 4.24: Near field images obtained with TCE Ag Ni-like XRL with different prepulse widths: in the left side the schematic up and the near field image down for 150 micron prepulse while on the right side the schematic and the near field for 200 micron prepulse are presented

flattening of the interfering fringes in the subcritical region was shown. For an axis-symmetric plasma, this is indicative of a density depression.

Density depressions induced by the ponderomotive force have also been observed in numerous other high-intensity laser experiments, in agreement with simulations. Some of the most recent studies include the formation of plasma channels and laser-hole boring in underdense and overdense plasmas motivated by the fast ignitor concept in inertial confinement fusion [WYH⁺94, TKT⁺00]. These experiments involved laser intensities of $1.7 \cdot 10^{15}$ and $2 \cdot 10^{17}$ W/cm², respectively. In addition, for several cases involving short laser pulses the saturation of the heat flux, refraction, or channeling of the laser radiation due to relativistic self-focusing at ultrahigh fluxes are found to be responsible for density suppression [MMM80, SBN⁺99]. However plasma temperature side lobes are observed here for the first time. This can be correlated with the above mentioned processes. Most likely our observations are a result of the interplay of several such effects.

The observed sidelobes might be the reason for an unwanted feature in the

XRL emission profile [KJR⁺02, GEK⁺03]. In these experiments ¹ performed in Paris at LULI 100 TW facility, the beam profile of the TCE Ag XRL was registered, as presented in fig. 4.24. The TCE XRL beam profile at the exit of the plasma for several conditions shows two regions with increased lasing. The presence of this behavior is influenced by the prepulse intensity and plasma gradients. It was observed that the emission lobes are stronger when the prepulse has larger fluence and at the same time it generates stronger density gradients. The presence of the two density lobes was proposed as the explanation of the two gain regions observed in the Ag experiments.

The keV emission dip observed in the GRIP Zr XRL at GSI is a complementary observation to those experiments at LULI where the two gain regions were imaged and with the plasma interferometry experiments where the density profiles were monitored [ASAL78, FRJ⁺03]. It is becoming clear that the analytical models are not covering such processes and full 2D-3D modeling has to be applied in order to keep track of them.

¹The geometry (close to normal incidence on target) and partial results of the experiments are extensively presented in [Neu03] where collimation of an XRL over large distances was demonstrated. The results are important for the Li-like ions fluorescence spectroscopy experiments which will take place at GSI, as described in section 1.2.

Chapter 5

Conclusions

Two factors are decisive for the large scale implementation of the transient collisionally pumped X-ray lasers in today's science: beam quality and repetition rate. A better beam quality of the XRL should allow to focus the laser to spots in the sub μm range with intensities exceeding 10^{14} W/cm². Higher repetition rates are substantial for high resolution spectroscopy experiments in the XUV regime [BBdMK⁺00], and also for studies of fundamental nonlinear processes like cluster explosion [WBdC⁺02] or two photons double electron ejection at shorter wavelengths. A significant step forward in this direction was achieved by the newly demonstrated GRIP scheme [KDS⁺03, KDP⁺05, NSC⁺04, LWL⁺05, RWL⁺05a, RWL⁺05b, TJPN05].

Work presented in this thesis contributes to the research in the field of the GRIP scheme in both analytical-numerical modeling of the processes involved and through experimental results analysis.

Starting with a recent analytical model for TCE XRL [LZ01, LLZ02] it's validity range and possible extension to the GRIP scheme was analyzed. Following clues from the experiments performed at GSI with a Zr XRL it was found that some significant corrections had to be applied to the formulas for the main pulse temperature and scale length in the GRIP scheme. This is due to the fact that the IB (inverse bremsstrahlung) absorption of the main pulse in plasma, the main absorption mechanism, is strongly affected by the incidence angle on target via the plasma density and the IB correction factor. Numerical corrections for the analytical formulas in the case of our Zr XRL experimental parameters were computed, demonstrating qualitative agreement with the experimental results.

A significant contribution to this analysis from the experimental part was the adoption of an x-ray pinhole camera with a special filter as diagnostic of the keV plasma emission. This allowed for spatially resolved, high dynamic range images of the plasma emission above the transmission filter cut-off at

500 eV.

In chapter 4, GRIP XRL using Zr as active medium is reported for the first time. An extensive optimization of the laser output was performed. In the strong pumping regime used in the experiments, the peak to peak delay was found to have only little influence on the XRL output over large variations of the order of few hundred of picosecond. This is in contrast to the results of [KDP⁺05] where 50 ps delay was critical for obtaining lasing in the weak pumping regime.

Extended analysis of these results in comparison with earlier experiments under 45° incidence on target and similar conditions was performed. In this way the understanding of the influence of the incidence angle was significantly extended. The optimum main pulse duration was found to be 0.5 ps, significantly different from the result with normal incidence TCE XRL where 3 to 6 ps were the optimum main pulse duration. A reduction of the absorption in the plasma was measured for shorter main pulse duration at constant pump energy which agrees qualitatively with the computations performed using the corrections proposed in chapter 2.

Gain curves were obtained for both lasing lines of the Ni-like GRIP Zr XRL. The small gain signal is similar for the two lasing lines. Saturation for the main lasing line (22.02 nm) is inferred while for the second lasing line this is not seen, suggesting the possibility of enhanced lasing output at the second lasing line for a longer active medium.

An important issue of the GRIP scheme is the generation of the traveling wave at grazing incidence angle. In most GRIP experiments a tilted on axis spherical mirror was introduced to form the main pulse focus. Typically the analysis of the intrinsic TW speed of this system is analyzed by ray-tracing. An analytical formula for the TW speed was developed and is presented in chapter 3. This eliminates the need of ray-tracing calculations for the optimization of the set-up, thus simplifying the implementation of this focusing system for other experiments like TCE Ni-like Tungsten XRL (as proposed for the near future at PHELIX).

An interesting result was obtained using the spatially resolved keV emission registered with the pinhole camera. Two side lobes in the emission showing increased temperature along the focal line of the main pulse were observed. The result correlates well with previous interference measurements of plasma density profile and with near field imaging of the TCE Ag XRL experiments at LULI. The plasma density distribution deduced from the experiments might account for the remaining difference between the model and the measurement. Numerical codes should be used to determine this influence.

The results concerning the XRL presented in this work give a clear pic-

ture of the TCE and GRIP XRL. Use of the GRIP scheme will lead to a better performance of the XRL source for spectroscopy of Li-like ions. For this purpose the laser will be transferred to the reinjection channel between ESR and SIS. In this context also the synchronization scheme of PHELIX with the accelerator bunches was settled. An accuracy of 1 ns is expected, mainly limited by long term thermal drift of the high frequency electronics. Development of an x-ray detector for the laser spectroscopy experiment was started. First spectroscopy experiments are expected in early 2007. They will provide a tool for accurate determination of the 2s-2p transition in different Li-like heavy ions. This will provide accurate values for the difference of nuclear charge radii between isotopes and isotones.

Another important perspective of the work presented in this thesis is the ability to predict the pumping efficiency in higher Z Ni-like lasers. Using the capability of the PHELIX laser, experiments at up to 150 J pulse energy are now planned. This should allow to create XRL output at several 100 eV photon energy, possibly reaching the water window. Using the codes presented in this thesis an optimal range for the pre-pulse energy and the focusing geometry for the main-pulse can be given.

Appendix A

Synchronization with SIS

The synchronization is presented in fig. A.1.

A complete list of signals for synchronization is made using the event list of the experimental place, as follows:

0.1) Mira is locked and 76 MHz signal is sent over as external clock for high frequency devices of SIS via optic link.

0.2) 10 Hz signal from the fs-front-end is sent over as refresh phase reference for high frequency devices of SIS via optic link.

1) Pulse request to the operators of SIS via telephone. They block the other concurrent experiments and approve the request. The experimentalist presses the start button in the PHELIX CS (PCS), thus starting the automatic procedure.

2) Beam request unit (AFE) is reading signal a) "virtual accelerator defined" and signal b) "SIS ok".

3) "SIS ok" is sent to the PCS

4) PCS starts to charge capacitors

5) PCS receives capacitor end of charge signal

6.1) PCS → AFE pulse request

6.2) PCS issues a level signal to Central Pulse Manager (Pulszentrale) of SIS (PZ) stating PHELIX is alive and ready for shot.

7) AFE → SIS CS "pulse request" (Signal 2)

8) CS SIS → AFE "super-cycle started"

9) AFE → PCS "super-cycle started"

10) Multi-multi injection(MMI) takes place

11) The event 40 (EVT_MB_TRIGGER) of channel 03 triggers the bunch-analysis computer (BAC) and initiates a measurement of the SIS current, PCS waits max 100 ms for an OK and injects further

12) BAC signalises "current in SIS ok". Alternatively, the signal from PCS expires after 30 s. End of supercycle.

13) BAC triggers on event 45 (EVT_FLATTOP) when the ramping is finished for another ion beam current measurement

14) BAC signalises "current in SIS ok" to SIS CS. Alternatively, the supercycle is restarted.

15) When BAC signalises current in SIS ok to SIS CS, it also triggers the sequence for the main pulse amplification. That means, it triggers the BNC555 with 4 channels to issue a signal at T0 minus n periods-front-end (10Hz) and in addition triggers the gate for the main PHELIX pulse with the appropriate delay.

16) T0 minus n periods-front-end (10 Hz) from BNC555 with 4 channels is sent to SIS CS to start Channel 06. n is determined off-line, typically n=2 or n=3. The first event on Channel 06 is event 105 (Primaerevent EVT_KICK_READY) or event 57 (EVT_EXTR_BUMP)

17) The event 105 or event 57 are decoded by the HF manager as a signal that in n 10 Hz periods PHELIX will fire. This gives enough lead time to generate the trigger for the timing generator, which kicks out the bunch from SIS.

18) Before event 56 (EVT_SYNCH) the newly defined event (see point B) is issued (about 100 microseconds in advance)

19) event 81 (EVT_HF_BM_START) is broadcast, implying that the amplitude of the HF starts to increase; event 149 (EVT_BUNCH_ROTATE) signalises that the rotation in the phase space started and there is a fixed time of the order of 500 microsecond to the best bunch longitudinal compression corresponding to 90° rotation in the phase space. At the end of the 90° rotation should take place the event 49 (EVT_KICK_START_1). This signalises to the timing generator that it is allowed to kick out the bunch from SIS. In our case, the kick start should come shortly before the kick out from SIS. Moreover, the kick out from SIS should be triggered by a signal directly from HF (P. Moritz) in order to make it fully deterministic. The 90° rotation (the synchrotron motion) takes about 1 ms.

20) the BNC555 with 4 channels opens the gate for the main PHELIX pulse with the appropriate delay (synchronous with the trigger from point 19 to the timing generator and with the bunch phase in SIS which is determined by the 76 MHz signal (point 0.1), by the 10 Hz signal (point 0.2) and by the point 17).

21) SIS ends supercycle; PHELIX stops.

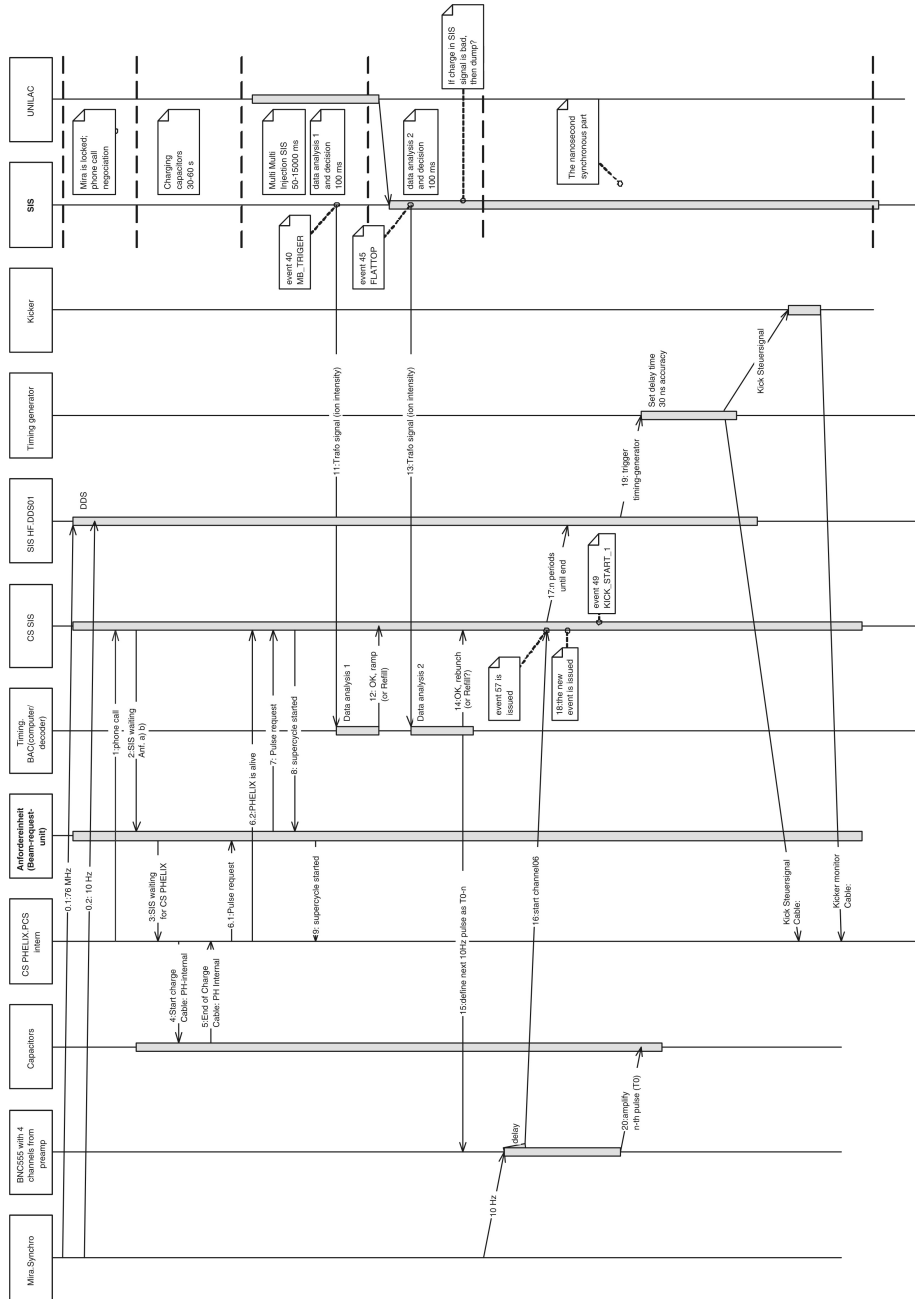


Figure A.1: Communication flow in the PHELIX-SIS synchronization scheme using SysML language

Bibliography

- [AATE⁺03] Y. Abou-Ali, G. J. Tallents, M. Edwards, R. E. King, G. J. Pert, S. J. Pestehe, F. Strati, R. Keenan, C. L. S. Lewis, and S. Topping. Measurement of the duration of x-ray lasing pumped by an optical laser pulse of picosecond duration. *Optics Communications*, 215(4-6):397–406, January 2003. [3.2.1](#)
- [ABB⁺02] V. Ayvazyan, N. Baboi, I. Bohnet, R. Brinkmann, M. Castellano, P. Castro, L. Catani, S. Choroba, A. Cianchi, M. Dohlus, H.T. Edwards, B. Faatz, A.A. Fateev, J. Feldhaus, K. Flttmann, A. Gamp, T. Garvey, H. Genz, Ch. Gerth, V. Gretchko, B. Grigoryan, U. Hahn, C. Hessler, K. Honkavaara, M. Hning, R. Ischebeck, M. Jablonka, T. Kamps, M. Krfer, M. Krassilnikov, J. Krzywinski, M. Liepe, A. Liero, T. Limberg, H. Loos, M. Lung, C. Magne, J. Menzel, P. Michelato, M. Minty, U.-C. Mller, D. Nlle, A. Novokhatski, C. Pagani, F. Peters, J. Pflger, P. Piot, L. Plucinski, K. Rehlich, I. Reyzl, A. Richter, J. Rossbach, E.L. Saldin, W. Sandner, H. Schlarb, G. Schmidt, P. Schmser, J.R. Schneider, E.A. Schneidmiller, H.-J. Schreiber, S. Schreiber, D. Sertore, S. Setzer, S. Simrock, R. Sobierajski, B. Sonntag, B. Steeg, F. Stephan, K.P. Sytchev, K. Tiedtke, M. Tonutti, R. Treusch, D. Trines, D. Trke, V. Verzilov, R. Wanzenberg, T. Weiland, H. Weise, M. Wendt, T. Wilhein, I. Will, K. Wittenburg, S. Wolff, M.V. Yurkov, and K. Zapfe. A new powerful source for coherent vuv radiation: Demonstration of exponential growth and saturation at the ttf free-electron laser. *The European Physical Journal D - Atomic, Molecular and Optical Physics*, 20(1):149–156, July 2002. [1.3](#)
- [AK94] Jerome M. Auerbach and Victor P. Karpenko. Serrated-aperture apodizers for high-energy laser systems. *Applied Optics*, 33:3179–3183, 1994. [3.1.2](#)
- [AS89] Yu V. Afanasev and V. N. Shlyapsev. *Sov. J. Quantum Electron.*, 19:1606, 1989. [1.3.1](#)
- [AS90] Yu V. Afanasev and V. N. Shlyapsev. *Proc. Int. Symposium on Short Wavelength Lasers and Their Applications (Samarkand USSR, May 1418, 1990) ed V V Korovkin and M Romanovsky (New York: Yu Nova Science Pub.)*, page 177, 1990. [1.3.1](#)
- [ASAL78] D. T. Attwood, D. W. Sweeney, J. M. Auerbach, and P. H. Y. Lee. Interferometric confirmation of radiation-pressure effects in laser-plasma interactions. *Physical Review Letters*, 40(3):184–187, 1978. [4.8](#), [4.8](#)

- [BBdMK⁺00] S. Borneis, B. Becker de Moos, H. J. Kluge, T. Kuehl, D. Marx, P.V. Nickles, P. Neumayer, W. Sandner, and W. Seelig. X ray laser spectroscopy at the esr: a proposed novel tool for the investigation of exotic isotopes. *Hyperfine Interactions*, 127(1 - 4):537–542, 2000. [1.2](#), [5](#)
- [BBS⁺05] Keith Boyer, Alex B Borisov, Xiangyang Song, Ping Zhang, John C McCorkindale, Shahab F Khan, Yang Dai, Paul C Kepple, Jack Davis, and Charles K Rhodes. Explosive supersaturated amplification on $3d \rightarrow 2p$ $\text{xe}(1)$ hollow atom transitions at $\lambda \sim 2.7\text{--}2.9 \text{ \AA}$. *Journal of Physics B: Atomic, Molecular and Optical Physics*, 38(16):3055–3069, 2005. [1.3](#)
- [BCTT05] P. Beiersdorfer, H. Chen, D. B. Thorn, and E. Trabert. Measurement of the two-loop lamb shift in lithiumlike $\text{u}[\text{sup } 89+]$. *Physical Review Letters*, 95(23):233003, 2005. [1.2](#)
- [BDS⁺03] Alex B Borisov, Jack Davis, Xiangyang Song, Yevgeniya Koshman, Yang Dai, Keith Boyer, and Charles K Rhodes. Saturated multikilovolt x-ray amplification with xe clusters: single-pulse observation of $\text{xe}(1)$ spectral hole burning. *Journal of Physics B: Atomic, Molecular and Optical Physics*, 36(17):L285–L294, 2003. [1.3](#)
- [BJM97] Laurence Bonnet, Sylvie Jacquemot, and Jean-Luc Miquel. Optimum laser driver for improvements of collisional recombination schemes at short wavelengths. *Soft X-Ray Lasers and Applications II*, 3156(1):98–108, 1997. [1.3](#)
- [BKM⁺03] C. Brandau, C. Kozhuharov, A. Muller, W. Shi, S. Schippers, T. Bartsch, S. Bohm, C. Bohme, A. Hoffknecht, H. Knopp, N. Grun, W. Scheid, T. Steih, F. Bosch, B. Franzke, P. H. Mokler, F. Nolden, M. Steck, T. Stohlker, and Z. Stachura. Precise determination of the $2s_{1/2} - 2p_{1/2}$ splitting in very heavy lithiumlike ions utilizing dielectronic recombination. *Physical Review Letters*, 91(7):073202, 2003. [1.2](#)
- [BPY⁺00] P. S. Banks, M. D. Perry, V. Yanovsky, S. N. Fochs, B. C. Stuart, , and J. Zweiback IEEE J. of Quant. Electron. Novel all-reflective stretcher for chirped-pulse-amplification of ultrashort pulses. *IEEE Journal of Quantum Electronics*, 36:268–274, 2000. [3.1.1](#)
- [BSZ⁺05] Alex B Borisov, Xiangyang Song, Ping Zhang, Arati Dasgupta, Jack Davis, Paul C Kepple, Yang Dai, Keith Boyer, and Charles K Rhodes. Amplification at $\lambda \sim 2.8 \text{ \AA}$ on $\text{xe}(1) (2\bar{s}2\bar{p})$ double-vacancy states produced by 248 nm excitation of xe clusters in plasma channels. *Journal of Physics B: Atomic, Molecular and Optical Physics*, 38(22):3935–3944, 2005. [1.3](#)
- [BW99] Max Born and Emil Wolf. *Principles of Optics*, chapter Foundations of geometrical optics, pages 116–141. Cambridge University Press, 1999. [2.3.1](#)
- [BWBP96] S C Burkhart, R B Wilcox, D Browning, and F A Penko. Amplitude and phase modulation with waveguide optics. Technical report, Lawrence Livermore National Laboratory, 1996. [3.1.1](#)
- [CMPN⁺05] E. Caurier, G. Martinez-Pinedo, F. Nowacki, A. Poves, and A. P. Zuker. The shell model as a unified view of nuclear structure. *Reviews of Modern Physics*, 77(2):427, 2005. [1.1](#)

- [CSS⁺00] Jean-Christophe Chanteloup, Estelle Salmon, Christian Sauteretand, Arnold Migus, Philippe Zeitoun, Annie Klisnick, Antoine Carillon, Stephane Hubert, David Ros, Peter Nickles, and Mikhail Kalachnikov. Pulse-front control of 15-tw pulses with a tilted compressor, and application to the subpicosecond traveling-wave pumping of a soft-x-ray laser. *Journal of the Optical Society of America B*, 17:151–157, 2000. [3.2.1](#)
- [CT73] D. Colombant and G. F. Tonon. X-ray emission in laser-produced plasmas. *Journal of Applied Physics*, 44(8):3524–3537, 1973. [2.1](#), [2.4.1](#), [2.4.1](#)
- [Dai02] Hiroyuki Daido. Review of soft x-ray laser researches and developments. *Reports on Progress in Physics*, 65(10):1513–1576, 2002. [1.3](#), [1.3](#)
- [DJPR76] R. J. Dewhurst, D. Jacoby, G. J. Pert, and S. A. Ramsden. Observation of a population inversion in a possible extreme ultraviolet lasing system. *Physical Review Letters*, 37(19):1265–1268, 1976. [1.3.1](#)
- [DLO⁺00] J. Dunn, Y. Li, A. L. Osterheld, J. Nilsen, J. R. Hunter, and V. N. Shlyaptsev. Gain saturation regime for laser-driven tabletop, transient ni-like ion x-ray lasers. *Physical Review Letters*, 84(21):4834–4837, 2000. [1.3.1](#)
- [DNI⁺97] H. Daido, S. Ninomiya, T. Imani, Y. Okaichi, M. Takagi, R. Kodama, H. Takabe, Y. Kato, F. Koike, J. Nilsen, and K. Murai. Atomic number scaling of the nickel-like soft x-ray lasers. *International Journal of Modern Physics B [Condensed Matter Physics; Statistical Physics; Applied Physics]*, 11:945–990, 1997. [2.4.2](#), [2.4.2](#)
- [DNO⁺99] James Dunn, Joseph Nilsen, Albert L. Osterheld, Yuelin Li, and Vyacheslav N. Shlyaptsev. Demonstration of transient gain x-ray lasers near 20 nm for nickellike yttrium,zirconium, niobium, and molybdenum. *Optics Letters*, 24:101–103, 1999. [4.1](#)
- [DOF⁺02] J. Dunn, A. L. Osterheld, A. Y. Faenov, T. A. Pikuz, and V. N. Shlyaptsev. Injector-amplifier design for tabletop Ne-like x-ray lasers. In *AIP Conf. Proc. 641: X-ray Lasers 2002*, pages 9–14, November 2002. [2.5](#)
- [DON⁺00] J. Dunn, A.L. Osterheld, J. Nilsen, J. R. Hunter, Y. Li, A. Ya. Faenov, T. A. Pikuz, and V.N. Shlyaptsev. Saturated output tabletop x-ray lasers. *X-RAY LASERS 2000: 7th International Conference on X-Ray Lasers*, pages 19–26, 2000. [4.4](#)
- [DOS⁺98] J. Dunn, A. L. Osterheld, R. Shepherd, W. E. White, V. N. Shlyaptsev, and R. E. Stewart. Demonstration of x-ray amplification in transient gain nickel-like palladium scheme. *Physical Review Letters*, 80(13):2825–2828, 1998. [1.3.1](#), [2.1](#)
- [DSS⁺03] James Dunn, Raymond F. Smith, Ronnie Shepherd, Rex Booth, Joseph Nilsen, James R. Hunter, and Vyacheslav N. Shlyaptsev. Temporal characterization of a picosecond-laser-pumped x-ray laser for applications. *Soft X-Ray Lasers and Applications V*, 5197(1):51–59, 2003. [2.5](#)
- [EHM⁺84] Jerry Edelstein, Michael C. Hettrick, Stanley Mrowka, Patrick Jelinsky, and Christopher Martin. Extreme uv measurements of a varied line-space hitachi reflection grating: efficiency and scattering. *Applied Optics*, 23(19):3267–3276, 1984. [3.2.2](#)

- [Eli02] Shalom Eliezer. *The interaction of high-power lasers with plasmas*. IOP Publishing Ltd., 2002. 1.3.1, 2.3.1, 2.3.1
- [Elt90] Raymond C. Elton. *X-Ray Lasers*. Academic Press, Inc., 1990. 1.3.1, 4.5
- [FRJ⁺03] J. Filevich, J. J. Rocca, E. Jankowska, E. C. Hammarsten, K. Kanizay, M. C. Marconi, S. J. Moon, and V. N. Shlyaptsev. Two-dimensional effects in laser-created plasmas measured with soft-x-ray laser interferometry. *Physical Review E (Statistical, Nonlinear, and Soft Matter Physics)*, 67(5):056409, 2003. 4.8, 4.8
- [FWS⁺92] D. J. Fields, R. S. Walling, G. M. Shimkaveg, B. J. MacGowan, L. B. Da Silva, J. H. Scofield, A. L. Osterheld, T. W. Phillips, M. D. Rosen, D. L. Matthews, W. H. Goldstein, and R. E. Stewart. Observation of high gain in ne-like ag lasers. *Physical Review A (Atomic, Molecular, and Optical Physics)*, 46(3):1606–1609, 1992. 1.3.1
- [GEK⁺92] J. S. De Groot, K. G. Estabrook, W. L. Kruer, R. P. Drake, K. Mizuno, and S. M. Cameron. Distributed absorption model for moderate to high laser powers. *Physics of Fluids B: Plasma Physics*, 4(3):701–707, 1992. 2.1, 2.1
- [GEK⁺03] Olivier Guilbaud, Matthew Edwards, Annie Klisnick, David Ros, Gerard Jamelot, Denis Joyeux, Daniel Phalippou, Huajing Tang, Paul Neumayer, Daniel Ursescu, Greg J. Tallents, Thomas Kuehl, K. Cassou, Kamal Bouhouch, Masataka Kado, Masaharu Nishikino, Kota Sukegawa, Maki Kishimoto, Masahiko Ishino, Keisuke Nagashima, Hiroyuki Daido, Wolfgang Seelig, Stefan Borneis, Erhard W. Gaul, W. Geithner, C. Hafner, and Piotr P. Wiewior. Near-field imaging of ni-like silver transient collisional x-ray laser. *Soft X-Ray Lasers and Applications V*, 5197(1):17–28, 2003. 4.8
- [GFR⁺02] J. J. Gonzalez, M. Frati, J. J. Rocca, V. N. Shlyaptsev, and A. L. Osterheld. High-power-density capillary discharge plasma columns for shorter wavelength discharge-pumped soft-x-ray lasers. *Physical Review E (Statistical, Nonlinear, and Soft Matter Physics)*, 65(2):026404, 2002. 1.3
- [GPW⁺04] Emily A. Gibson, Ariel Paul, Nick Wagner, Ra'anan Tobey, Sterling Backus, Ivan P. Christov, Margaret M. Murnane, and Henry C. Kapteyn. High-order harmonic generation up to 250 eV from highly ionized argon. *Physical Review Letters*, 92(3):033001, 2004. 1.3
- [GSF05] G. Gaigalas, O. Scharf, and S. Fritzsche. Maple procedures for the coupling of angular momenta. viii. spin-angular coefficients for single-shell configurations. *Computer Physics Communications*, 166(2):141–169, March 2005. 1.1
- [GSH79] R. N. Gyuzalian, S. B. Sogomonian, and Z. Gy. Horvath. Background-free measurement of time behaviour of an individual picosecond laser pulse. *Optics Communications*, 29(2):239–242, 1979. 3.1.4
- [HKM⁺02] J.-F. Hergott, M. Kovacev, H. Merdji, C. Hubert, Y. Mairesse, E. Jean, P. Breger, P. Agostini, B. Carre, and P. Salieres. Extreme-ultraviolet high-order harmonic pulses in the microjoule range. *Physical Review A (Atomic, Molecular, and Optical Physics)*, 66(2):021801, 2002. 1.3

- [HS98] J. M. Howard and B. D. Stone. Imaging a Point to a Line with a Single Spherical Mirror. *Applied Optics*, 37:1826–1834, April 1998. 3.2.1
- [IP74] F E Irons and N J Peacock. Experimental evidence for population inversion in c^{5+} in an expanding laser-produced plasma. *Journal of Physics B: Atomic and Molecular Physics*, 7(9):1109–1112, 1974. 1.3.1
- [JJC⁺87] Pierre Jaegle, Gerard Jamelot, Antoine Carillon, Annie Klisnick, Alain Sureau, and Helene Guennou. Soft-x-ray amplification by lithiumlike ions in recombining hot plasmas. *JOSAB*, 4:563–574, 1987. 1.3.1
- [JLP⁺03] K. A. Janulewicz, A. Lucianetti, G. Priebe, W. Sandner, and P. V. Nickles. Saturated ni-like ag x-ray laser at 13.9 nm pumped by a single picosecond laser pulse. *Physical Review A (Atomic, Molecular, and Optical Physics)*, 68(5):051802, 2003. 2.5, 3.2.1, 4.6
- [JNKP04] K. A. Janulewicz, P. V. Nickles, R. E. King, and G. J. Pert. Influence of pump pulse structure on a transient collisionally pumped ni-like ag x-ray laser. *Physical Review A (Atomic, Molecular, and Optical Physics)*, 70(1):013804, 2004. 4.6
- [JTPN05] K. A. Janulewicz, J. Tummler, G. Priebe, and P. V. Nickles. Plasma-kinetics perspective on a collisional ni-like x-ray laser pumped by a single profiled laser pulse. *Physical Review A (Atomic, Molecular, and Optical Physics)*, 72(4):043825, 2005. 4.6
- [KB04] H.-J. Kluge and K. Blaum. Trapping radioactive ions. *Nuclear Physics A*, 746:200–205, 2004. 1.1
- [KBHQ03] H.-J. Kluge, K. Blaum, F. Herfurth, and W. Quint. Atomic and nuclear physics with stored particles in ion traps. *Physica Scripta*, T104(167), 2003. 1.1
- [KBMD02] Jaroslav Kuba, Djamel Benredjem, Clary Moller, and Ladislav Drska. Analytical ray-tracing of a transient x-ray laser: Ni-like ag laser at 13.9 nm. *X-RAY LASERS 2002: 8th International Conference on X-Ray Lasers*, 641:46–51, 2002. 2.3.1
- [KDP⁺05] R. Keenan, J. Dunn, P. K. Patel, D. F. Price, R. F. Smith, and V. N. Shlyaptsev. High-repetition-rate grazing-incidence pumped x-ray laser operating at 18.9 nm. *Physical Review Letters*, 94(10):103901, 2005. 3.2.1, 5
- [KDS⁺03] Roisin Keenan, James Dunn, Vyacheslav N. Shlyaptsev, Raymond F. Smith, Pravesh K. Patel, and Dwight F. Price. Efficient pumping schemes for high average brightness collisional x-ray lasers. *Soft X-Ray Lasers and Applications V*, 5197(1):213–220, 2003. 3.2.1, 5
- [KHNK83] T. Kita, T. Harada, N. Nakano, and H. Kuroda. Mechanically ruled aberration-corrected concave gratings for a flat-field grazing-incidence spectrograph. *Applied Optics*, 22:512–513, 1983. 3.2.2
- [KJR⁺02] Annie Klisnick, Gerard Jamelot, David Ros, Antoine Carillon, Pierre Jaegle, Mustapha Boussoukaya, Olivier Guilbaud, Jaroslav Kuba, Raymond Smith, Jean-Claude Lagron, Laurent Vanbostal, Denis Joyeux, Daniel

- Phalippou, Stephane Sebban, Alain Touati, Marie Anne Herve du Penhoat, F. Ballester, E.-J. Petit, Bedrich Rus, Tomas Mocek, Federico Strati, Matthew Edwards, Gregory J. Tallents, Roisin Keenan, Simon Topping, Ciaran L. S. Lewis, Paul Neumeyer, Daniel Ursescu, Thomas Kuhl, Huajing Tang, and Hiroyuki Daido. Development and applications of x-ray lasers at lsai/lixam. *X-RAY LASERS 2002: 8th International Conference on X-Ray Lasers*, 641(1):166–173, 2002. 1.3, 1.3.1, 2.5, 4.8
- [Klu02] H. Jurgen Kluge. Atomic physics techniques applied to nuclear physics. *Nuclear Physics A*, 701(1-4):495–502, 2002. 1.1
- [KN03] H. Jurgen Kluge and Wilfried Nortershauser. Lasers for nuclear physics. *Spectrochimica Acta Part B: Atomic Spectroscopy*, 58(6):1031–1045, 2003. 1.1
- [KPM⁺01] R. E. King, G. J. Pert, S. P. McCabe, P. A. Simms, A. G. MacPhee, C. L. S. Lewis, R. Keenan, R. M. N. O’Rourke, G. J. Tallents, S. J. Pestehe, F. Strati, D. Neely, and R. Allott. Saturated x-ray lasers at 196 and 73 a pumped by a picosecond traveling-wave excitation. *Physical Review A (Atomic, Molecular, and Optical Physics)*, 64(5):053810, 2001. 1.3.1, 3.1.3, 3.2.1
- [KZR⁺00] A. Klisnick, P. Zeitoun, D. Ros, A. Carillon, P. Fourcade, S. Hubert, G. Jamelot, C. L. S. Lewis, A. G. Mac Phee, R. M. N. Rourke, R. Keenan, P. V. Nickles, K. Janulewicz, M. Kalashnikov, J. Warwick, J.-C. Chanteloup, A. Migus, E. Salmon, C. Sauteret, and J. P. Zou. Transient pumping of a ni-like ag x-ray laser with a subpicosecond pump pulse in a traveling-wave irradiation geometry. *Journal of the Optical Society of America B*, 17:1093–1097, 2000. 3.2.1
- [Lan80] A. Bruce Langdon. Nonlinear inverse bremsstrahlung and heated-electron distributions. *Physical Review Letters*, 44:575579, 1980. 2.2, 4.4
- [LLPF97] Yuelin Li, Peixiang Lu, Georg Pretzler, and Ernst E. Fill. Lasing in neonlike sulphur and silicon. *Optics Communications*, 133(1-6):196–200, January 1997. 1.3.1
- [LLZ02] Y. J. Li, X. Lu, and J. Zhang. Effects of delay time on transient ni-like x-ray lasers. *Physical Review E (Statistical, Nonlinear, and Soft Matter Physics)*, 66(4):046501, 2002. 1.3.1, 4.2, 4.4, 4.4, 4.4, 5
- [LPSS74] G.J. Linford, E.R. Peressini, W.R. Sooy, and M.L. Spaeth. Very long lasers. *Applied Optics*, 13(2):379–390, 1974. 2.5, 4.5
- [LWL⁺05] B. M. Luther, Y. Wang, M. A. Larotonda, D. Aless, M. Berrill, M. C. Marconi, J. J. Rocca, and V. N. Shlyaptsev. Saturated high-repetition-rate 18.9-nm tabletop laser in nickellike molybdenum. *Optics Letters*, 30:165–167, 2005. 3.2.1, 5
- [LZ01] Y. J. Li and J. Zhang. Hydrodynamic characteristics of transient ni-like x-ray lasers. *Physical Review E (Statistical, Nonlinear, and Soft Matter Physics)*, 63:036410, 2001. 1.3.1, 2.1, 2.1, 2.1, 4.2, 4.4, 4.4, 4.4, 4.12, 5

- [MHR⁺85] D. L. Matthews, P. L. Hagelstein, M. D. Rosen, M. J. Eckart, N. M. Ceglio, A. U. Hazi, H. Medeck, B. J. MacGowan, J. E. Trebes, B. L. Whitten, E. M. Campbell, C. W. Hatcher, A. M. Hawryluk, R. L. Kauffman, L. D. Pleasance, G. Rambach, J. H. Scofield, G. Stone, and T. A. Weaver. Demonstration of a soft x-ray amplifier. *Physical Review Letters*, 54(2):110–113, 1985. 1.3.1
- [MHRS85] S. Maxon, P. Hagelstein, K. Reed, and J. Scofield. A gas puff soft x-ray laser target design. *Journal of Applied Physics*, 57(3):971–972, 1985. 1.3.1
- [MMH⁺87] B. J. MacGowan, S. Maxon, P. L. Hagelstein, C. J. Keane, R. A. London, D. L. Matthews, M. D. Rosen, J. H. Scofield, and D. A. Whelan. Demonstration of soft x-ray amplification in nickel-like ions. *Physical Review Letters*, 59(19):2157–2160, 1987. 1.3.1
- [MMM80] Claire Ellen Max, Christopher F. McKee, and W. C. Mead. Scaling of ablative laser-fusion implosions. *Physical Review Letters*, 45(1):28–31, 1980. 4.8
- [MMS⁺90] B. J. MacGowan, S. Maxon, L. B. Da Silva, D. J. Fields, C. J. Keane, D. L. Matthews, A. L. Osterheld, J. H. Scofield, G. Shimkaveg, and G. F. Stone. Demonstration of x-ray amplifiers near the carbon k edge. *Physical Review Letters*, 65(4):420–423, 1990. 1.3.1
- [MNDS94] J. C. Moreno, J. Nilsen, and L. B. Da Silva. Traveling wave excitation and amplification of neon-like germanium 3p-3s transitions. *Optics Communications*, 110(5-6):585–589, September 1994. 3.2.1
- [MSM⁺05] T. Mocek, S. Sebban, G. Maynard, Ph. Zeitoun, G. Faivre, A. Hallou, M. Fajardo, S. Kazamias, B. Cros, D. Aubert, G. de Lacheze-Murel, J. P. Rousseau, and J. Dubau. Absolute time-resolved x-ray laser gain measurement. *Physical Review Letters*, 95(17):173902, 2005. 2.5
- [NAdM⁺01] Paul Neumayer, J. Alvarez, Bruno Becker de Mos, Stefan Borneis, K. Brueck, Erhard W. Gaul, C. Haefner, Karol A. Janulewicz, Thomas Kuehl, Dieter Marx, Irene Reinhard, Marco Tomaselli, Peter V. Nickles, Wolfgang Sandner, Wolfgang Seelig, Paul Neumayer, J. Alvarez, Bruno Becker de Mos, Stefan Borneis, K. Brueck, Erhard W. Gaul, C. Haefner, Karol A. Janulewicz, Thomas Kuehl, Dieter Marx, Irene Reinhard, Marco Tomaselli, Peter V. Nickles, Wolfgang Sandner, and Wolfgang Seelig. X-ray laser spectroscopy on lithium-like ions. *Soft X-Ray Lasers and Applications IV*, 4505:236–242, 2001. 1.2, 3.2.1
- [Neu02] R. Neugart. Lasers in nuclear physics –a review. *The European Physical Journal A - Hadrons and Nuclei*, 15(1 - 2):35–39, 2002. 1.1
- [Neu03] Paul Neumayer. *Ein transienter Röntgenlaser zur Laserspektroskopie an Lithium-ähnlichen Ionen*. PhD thesis, TU Darmstadt, Germany, 2003. 1.4, 3.2, 3.2.1, 1
- [Ney03] Gerda Neyens. Nuclear magnetic and quadrupole moments for nuclear structure research on exotic nuclei. *Reports on Progress in Physics*, 66(4):633–689, 2003. 1.1

- [Nil97] Joseph Nilsen. Design of a picosecond-laser-driven ni-like mo x-ray laser near 20 nm. *Journal of the Optical Society of America B*, 14:1511, 1997. 4.1
- [NSC⁺04] P. Neumayer, W. Seelig, K. Cassou, A. Klisnick, D. Ros, D. Ursescu, T. Kuehl, S. Borneis, E. Gaul, W. Geithner, C. Haefner, and P. Wiewior. Transient collisionally excited x-ray laser in nickel-like zirconium pumped with the phelix laser facility. *Applied Physics B: Lasers and Optics*, 78(7-8):957–959, 2004. 1.2, 3.2, 4.3, 5
- [NSK⁺97] P. V. Nickles, V. N. Shlyaptsev, M. Kalachnikov, M. Schnurer, I. Will, and W. Sandner. Short pulse x-ray laser at 32.6 nm based on transient gain in ne-like titanium. *Physical Review Letters*, 78(14):2748–2751, 1997. 1.3.1, 2.1, 2.2, 3.2.1
- [NTN⁺03] Masaharu Nishikino, Momoko Tanaka, Keisuke Nagashima, Maki Kishimoto, Masataka Kado, Tetsuya Kawachi, Kouta Sukegawa, Yoshihiro Ochi, Noboru Hasegawa, and Yoshiaki Kato. Demonstration of a soft-x-ray laser at 13.9 nm with full spatial coherence. *Physical Review A (Atomic, Molecular, and Optical Physics)*, 68(6):061802, 2003. 1.3.1, 2.5
- [Ott89] E. W. Otten. *Treatise on Heavy-Ion Science*. Plenum Press, New York, 1989. 1.1
- [PBK⁺95] J Paisner, J Boyes, S Kumpan, W H Lowdermilk, and M Sorem. Conceptual design of the national ignition facility. Technical report, Lawrence Livermore National Laboratory, 1995. 3.1.1
- [Pel01] Claudio Pellegrini. Design considerations for a sase x-ray fel. *Nuclear Instruments and Methods in Physics Research Section A: Accelerators, Spectrometers, Detectors and Associated Equipment*, 475(1-3):1–12, December 2001. 1.3
- [PKW00] G. Pretzler, A. Kasper, and K.J. Witte. Angular chirp and tilted light pulses in cpa lasers. *Applied Physics B: Lasers and Optics*, 70(1):1–9, January 2000. 3.1.4, 3.2.1
- [PZR⁺01] Sebastien Le Pape, Philippe Zeitoun, Jorge J. G. Rocca, Antoine Carillon, Pierre Dhez, Marc Francois, S. Hubert, Mourad Idir, and David Ros. Characterization of an x-ray laser beam. *Soft X-Ray Lasers and Applications IV*, 4505(1):23–34, 2001. 1.4
- [RH85] I N Ross and E M Hodgson. Some optical designs for the generation of high quality line foci. *Journal of Physics E: Scientific Instruments*, 18(2):169–173, 1985. 3.2.1
- [RLH88] M. D. Rosen, R. A. London, and P. L. Hagelstein. The scaling of ne-like x-ray laser schemes to short wavelength. *Physics of Fluids*, 31(3):666–670, 1988. 1.3.1
- [RMP⁺02] B. Rus, T. Mocek, A. R. Prag, M. Kozlova, G. Jamelot, A. Carillon, D. Ros, D. Joyeux, and D. Phalippou. Multimillijoule, highly coherent x-ray laser at 21 nm operating in deep saturation through double-pass amplification. *Physical Review A (Atomic, Molecular, and Optical Physics)*, 66(6):063806, 2002. 2.5

- [RST⁺94] J. J. Rocca, V. Shlyaptsev, F. G. Tomasel, O. D. Cortazar, D. Hartshorn, and J. L. A. Chilla. Demonstration of a discharge pumped table-top soft-x-ray laser. *Physical Review Letters*, 73(16):2192–2195, 1994. 1.3.1
- [RWL⁺05a] J. J. Rocca, Y. Wang, M. A. Larotonda, B. M. Luther, D. Alessi, M. Berrill, A. Weith, M. C. Marconi, C. S. Menoni, and V. N. Shlyaptsev. Demonstration of saturated high repetition rate tabletop soft x-ray lasers at wavelengths down to 13.2 nm. *Soft X-Ray Lasers and Applications VI*, 5919(1):591901, 2005. 5
- [RWL⁺05b] J. J. Rocca, Y. Wang, M. A. Larotonda, B. M. Luther, M. Berrill, and D. Alessi. Saturated 13.2 nm high-repetition-rate laser in nickellike cadmium. *Optics Letters*, 30:2581–2583, 2005. 3.2.1, 5
- [SBB⁺91] J. Schweppe, A. Belkacem, L. Blumenfeld, Nelson Claytor, B. Feinberg, Harvey Gould, V. E. Kostroun, L. Levy, S. Misawa, J. R. Mowat, and M. H. Prior. Measurement of the lamb shift in lithiumlike uranium ($u_{\text{sup}} 89 +$). *Physical Review Letters*, 66(11):1434–1437, 1991. 1.2
- [SBN⁺99] G. S. Sarkisov, V. Yu. Bychenkov, V. N. Novikov, V. T. Tikhonchuk, A. Maksimchuk, S.-Y. Chen, R. Wagner, G. Mourou, and D. Umstadter. Self-focusing, channel formation, and high-energy ion generation in interaction of an intense short laser pulse with a he jet. *Physical Review E (Statistical Physics, Plasmas, Fluids, and Related Interdisciplinary Topics)*, 59(6):7042–7054, 1999. 4.8
- [SBS⁺97] Ch. Spielmann, N. H. Burnett, S. Sartania, R. Koppitsch, M. Schnrer, C. Kan, M. Lenzner, P. Wobrauschek, and F. Krausz. Generation of coherent x-rays in the water window using 5-femtosecond laser pulses. *Science*, 278(5338):661–664, October 1997. 1.3
- [SGRB87] F. Salin, P. Georges, G. Roger, and A. Brun. Single-shot measurement of a 52-fs pulse. *Applied Optics*, 26:4528, 1987. 3.1.4
- [SHC92] M. Stern, J. P. Heritage, and E. W. Chase. Grating compensation of third order fiber dispersion. *IEEE Journal of Quantum Electronics*, 28:2742–2748, 1992. 3.1.4
- [SKF05] Andrey Surzhykov, Peter Koval, and Stephan Fritzsche. Algebraic tools for dealing with the atomic shell model. i. wavefunctions and integrals for hydrogen-like ions. *Computer Physics Communications*, 165(2):139–156, January 2005. 1.1
- [SMR⁺02] S. Sebban, T. Mocek, D. Ros, L. Upcraft, Ph. Balcou, R. Haroutunian, G. Grillon, B. Rus, A. Klisnick, A. Carillon, G. Jamelot, C. Valentin, A. Rousse, J. P. Rousseau, L. Notebaert, M. Pittman, and D. Hulin. Demonstration of a ni-like kr optical-field-ionization collisional soft x-ray laser at 32.8 nm. *Physical Review Letters*, 89(25):253901, 2002. 1.3
- [SP05] SysML-Partners. Systems modeling language (sysml) specification v1.0a; <http://www.sysml.org/artifacts.htm>. <http://www.sysml.org/artifacts.htm>, 2005. 1.4
- [SSM⁺85] S. Suckewer, C. H. Skinner, H. Milchberg, C. Keane, and D. Voorhees. Amplification of stimulated soft x-ray emission in a confined plasma column. *Physical Review Letters*, 55:17531756, 1985. 1.3.1

- [STZ⁺99] R. Smith, G. J. Tallents, J. Zhang, G. Eker, S. McCabe, G. J. Pert, and E. Wolfrum. Saturation behavior of two x-ray lasing transitions in ni-like dy. *Physical Review A (Atomic, Molecular, and Optical Physics)*, 59(1):R47–R50, 1999. 1.3.1
- [SW79] L. Schlessinger and J. Wright. Inverse-bremsstrahlung absorption rate in an intense laser field. *Physical Review A*, 20:1934, 1979. 2.2
- [Tal03] G J Tallents. The physics of soft x-ray lasers pumped by electron collisions in laser plasmas. *Journal of Physics D: Applied Physics*, 36(15):R259–R276, 2003. 2.3.3, 2.4.2, 2.4.2
- [TJPN05] J. Tummler, K. A. Janulewicz, G. Priebe, and P. V. Nickles. 10-hz grazing-incidence pumped ni-like mo x-ray laser. *Physical Review E (Statistical, Nonlinear, and Soft Matter Physics)*, 72(3):037401, 2005. 3.2.1, 5
- [TKT⁺00] K. Takahashi, R. Kodama, K. A. Tanaka, H. Hashimoto, Y. Kato, K. Mima, F. A. Weber, Jr. T. W. Barbee, and L. B. Da Silva. Laser-hole boring into overdense plasmas measured with soft x-ray laser probing. *Physical Review Letters*, 84(11):2405–2408, 2000. 4.8
- [TLF⁺04] M. Tomaselli, L.C. Liu, S. Fritzsche, T. Kuhl, and D. Ursescu. Cluster transformation coefficients in many-body nuclear physics. *Nuclear Physics A*, 738:216–220, 2004. 1.1
- [TLFK04] M Tomaselli, L C Liu, S Fritzsche, and T KühL. Dressed bosons theory for nuclear structure. *Journal of Physics G: Nuclear and Particle Physics*, 30(9):999–1020, 2004. 1.1
- [TLK⁺03] M Tomaselli, L C Liu, T KühL, W Nörtershäuser, D Ursescu, and S Fritzsche. Cluster-transformation coefficients for structure and dynamics calculations in n -particle systems: atoms, nuclei and quarks. *Journal of Optics B: Quantum and Semiclassical Optics*, 5(3):S395–S401, 2003. 1.1
- [TNM04] Eiji J. Takahashi, Yasuo Nabekawa, and Katsumi Midorikawa. Low-divergence coherent soft x-ray source at 13 nm by high-order harmonics. *Applied Physics Letters*, 84(1):4–6, 2004. 1.3
- [UCK⁺04] D. Ursescu, K. Cassou, A. Klisnick, T. Kuehl, P. Neumayer, P. Nickles, D. Ros, S. Borneis, E. Gaul, W. Geithner, C. Haefner, and P. Wiewior. Transient collisionally pumped x-ray laser at PHELIX. In D. Batani, C. J. Joachain, and S. Martellucci, editors, *Atoms and plasmas in super intense laser fields*, volume 88. SIF, 2004. 3.2
- [UKT⁺05] D. Ursescu, T. Kuehl, A. Tauschwitz, P. Moritz, M. Sayed, and P. Schuett. Internal and external synchronization at phelix. Technical report, GSI Darmstadt, 2005. 1.4
- [UTKF05] D. Ursescu, M. Tomaselli, T. Kuehl, and S. Fritzsche. Symbolic algorithms for the computation of moshinsky brackets and nuclear matrix elements. *Computer Physics Communications*, 173(3):140–161, December 2005. 1.1
- [VAVE77] Sobelman I Vinogradov A V and Yukov E. *Sovietic Journal of Quantum Electronics*, 7:32, 1977. 1.3.1

- [WBdC⁺02] H. Wabnitz, L. Bittner, A. R. B. de Castro, R. Dohrmann, P. Gurtler, T. Laarmann, W. Laasch, J. Schulz, A. Swiderski, K. von Haefen, T. Moller, B. Faatz, A. Fateev, J. Feldhaus, C. Gerth, U. Hahn, E. Saldin, E. Schneidmiller, K. Sytchev, K. Tiedtke, R. Treusch, and M. Yurkov. Multiple ionization of atom clusters by intense soft x-rays from a free-electron laser. *Nature*, 420(6915):482–485, December 2002. 5
- [WYH⁺94] S. Wilks, P. E. Young, J. Hammer, M. Tabak, and W. L. Kruer. Spreading of intense laser beams due to filamentation. *Physical Review Letters*, 73(22):2994–2997, 1994. 4.8
- [ZFS⁺04] Ph. Zeitoun, G. Faivre, S. Sebban, T. Mocek, A. Hallou, M. Fajardo, D. Aubert, Ph. Balcou, F. Burgy, D. Douillet, S. Kazamias, G. de Lacheze-Murel, T. Lefrou, S. le Pape, P. Mercere, H. Merdji, A. S. Morlens, J. P. Rousseau, and C. Valentin. A high-intensity highly coherent soft x-ray femtosecond laser seeded by a high harmonic beam. *Nature*, 431(7007):426–429, September 2004. 1.3.1, 2.5
- [ZKL76] A. Zherikhin, K. Koshelev, and V. Letokhov. *Sovietic Journal of Quantum Electronics*, 6:82, 1976. 1.3.1
- [ZKN⁺95] J. Zhang, M. H. Key, P. A. Norreys, G. J. Tallents, A. Behjat, C. Danson, A. Demir, L. Dwivedi, M. Holden, P. B. Holden, C. L. S. Lewis, A. G. MacPhee, D. Neely, G. J. Pert, S. A. Ramsden, S. J. Rose, Y. F. Shao, O. Thomas, F. Walsh, and Y. L. You. Demonstration of high gain in a recombination xuv laser at 18.2 nm driven by a 20 j, 2 ps glass laser. *Physical Review Letters*, 74(8):1335–1338, 1995. 1.3.1
- [ZML⁺97] J. Zhang, A. G. MacPhee, J. Lin, E. Wolfrum, R. Smith, C. Danson, M. H. Key, C. L. S. Lewis, D. Neely, J. Nilsen, G. J. Pert, G. J. Tallents, and J. S. Wark. A saturated x-ray laser beam at 7 nanometers. *Science*, 276:1097 – 1100, 1997. 1.3.1
- [ZMN⁺97] J. Zhang, A. G. MacPhee, J. Nilsen, J. Lin, Jr. T. W. Barbee, C. Danson, M. H. Key, C. L. S. Lewis, D. Neely, R. M. N. O’Rourke, G. J. Pert, R. Smith, G. J. Tallents, J. S. Wark, and E. Wolfrum. Demonstration of saturation in a ni-like ag x-ray laser at 14 nm. *Physical Review Letters*, 78(20):3856–3859, 1997. 1.3.1

Lebenslauf

Persönliche Daten

Vorname: Daniel
Name: Ursescu
Geburtsdatum: 21.01.1976
Geburtsort: Piatra Neamț, Rumänien
Familienstand: Verheiratet
Staatsangehörigkeit: rumänisch

Schulbildung

09/1982–07/1990 Grundschule in Piatra Neamț
09/1990–07/1994 Gymnasium “Liceul Petru Rareș”, Piatra Neamț (Leistungskurse Mathematik und Physik)

Studium und Arbeit

09/1994–07/1999 Fachbereich Physik an der Universität Bucharest, Rumänien; Diplomarbeit: “Langmuir Probes Measurement in the Reflex Plasma Reactor”
04/1999–01/2000 Wissenschaftliche Hilfskraft: Low-temperature plasma laboratory; National Institute for Lasers, Radiation and Plasma Physics, Bucharest
09/1999–07/2000 Vertiefte Studien, Fachbereich Physik an der Universität Bucharest; Vertiefte Studien Diplomarbeit: “Metal Matrix Composites Laser Cladding on Aluminium”
02/2000–06/2000 Stipendium bei ENSAIS, Strasbourg, Frankreich; Forschungsthema: “Metal Matrix Composites Materials with Aluminium Cladding” (Wear, 2005, **258**, p. 1745-1754)
11/2000–12/2001 Wissenschaftliche Hilfskraft: Entwicklung von Lasern mit ultrastabiler Frequenz für optische Uhren und Tests der speziellen Relativitätstheorie; Heinrich Heine Universität Düsseldorf
01/2002– Wissenschaftliche Hilfskraft: Röntgenlaser entwicklung für Li-ähnliche Ionen Spectroscopie; Johannes Gutenberg Universität Mainz und GSI-Darmstadt

Sonstiges

- 25-27.03.2002 New X-ray Science; X-ray Investigation of Fast and Ultrafast Processes; am Hamburger Synchrotronstrahlungslabor, DESY, Hamburg
- 5-15.07.2003 International summer school of quantum electronics, 37th course: Atoms and Plasmas in Super-intense Laser Fields, Erice-Sicily, Italien

Sprachen

Englisch flüssig, Deutsch gut, Französisch gut, Rumänisch Muttersprache

Darmstadt, March 9, 2006